

Acoustically focusing and measuring biological cells

A thesis submitted to attain the degree of
DOCTOR OF SCIENCES
(Dr. sc. ETH Zurich)

presented by

Cooper Lars Harshbarger

MSc in Mechanical Engineering, ETH Zurich
born on March 14, 1993
citizen of Switzerland, Sweden and the USA

accepted on the recommendation of

Prof. Dr. Jürg Dual, examiner

Prof. Dr. Jess Snedeker, co-examiner

Prof. Dr. Martin Wiklund, co-examiner

Dr. Unai Silván, co-examiner

*"In the morning when you finally go
And the nurse runs in with her head hung low
And the cardinal hits the window"*
- Sufjan Stevens

Acknowledgments

This work would never have been possible without a great deal of people to whom I wish to express my gratitude to:

- Prof. Jürg Dual for accepting me as a bachelor student to work on acoustofluidics. This was the start to a fantastic journey through this highly interdisciplinary field. And for being a role model, demonstrating what perseverance and patience can achieve.
- Prof. Jess Snedeker not only for being my supervisor, but a mentor who helped answer questions of life, from the very big to the very small. Always with astounding insight about the big picture, no matter how far away from your field of expertise.
- Prof. Martin Wiklund for taking the time to read and evaluate my thesis. Your name has continuously been a part of my journey since I entered the field of acoustofluidics in 2016 and it is an honor to have you on my PhD committee. Tack!
- Dr. Unai Silván for the endless hours of scientific discussions and teaching me all the methods that I needed, and then some. I highly appreciate the dedication you had towards my training and any biological relevance that this thesis has is directly linked to your efforts. Beyond the scientific collaboration, I will cherish the memories outside of the lab and look forward to a Kalimotxo, or two.
- Dr. Alen Pavlic, on the one hand for being a vital contributor to my scientific inquiries and always being there to answer any questions I had concerning acoustofluidics. On the other hand, for being an incredible friend, companion and best office mate I could ever have wished for. I find it hard to imagine having completed this thesis had you not been here.
- Davide Bernardoni, for the help on collecting experimental data. I consider myself fortunate to have received your e-mail by chance and truly appreciate your dedication for the numerous projects that we worked on. Being your supervisor and friend was one of the easiest tasks during my PhD.
- Jan Ghadamian, Jana Petr and Amelie Viol, for their contributions to my scientific inquiries, being fantastic and reliable students who truly helped move the needle and all-around great people to have been a part of my life.

- in no particular order, the remaining 14 students, from whom I learnt much on a scientific, professional and personal level.
- Dr. Alekhya Mazumdar, Alina Dintheer, Dr. Amro Hussien, Dr. Aron Horvát, Barbara Niederöst, Beate Fonfé, Bernhard Zybach, Dr. Christoph Goering, Dhananjay Deshmukh, Elio Gubser, Esteban Ongini, Dr. Fabian Passini, Dr. Frédéric Cornaz, Greta Moschini, Helen Strebel, Dr. Irina Heggli, Jean-Claude Tomasina, Dr. Joaquin Urdinez, Jonas Fankhauser, Dr. Jonas Widmer, Joyce Kimenai, Dr. Knut Husmann, Lieke Mous, Maja Bollhalder, Maja Wolleb, Marie-Rosa Fasser, Dr. Michael Gerlt, Martina Koch-Jetzer, Moritz Jokeit, Nicole Chittim, Dr. Nino Wili, Patrick Jäger, Dr. Peter Reichert, Santiago Ardiles, Dr. Sander Botter, Dr. Sarah Morice, Dr. Sebastiano Caprara, Severin Pang, Dr. Thierry Baasch, Dr. Tino Stauber, Tobias Götschi and Dr. Valentin van Gemmeren. Even if the tasks that awaited me sometimes seemed frustrating and never-ending, I always looked forward to coming into the lab because you were there. Without you, this thesis would not exist. You were my scientific sparing partners, work colleagues, and above everything else my family.
- the PhD students, lab technicians and post docs not explicitly mentioned in both Jürg and Jess's lab for being the backbone on which I could build my research.
- the 40-ish teaching assistants who helped me through all of the courses and in which I could always place my trust.
- my friends and family. These past years have been a growing experience. Not just the PhD, but the combined 9.5 years at ETH have been demanding in every conceivable way. Even if it was not always clear what I was doing I still felt your unconditional support, no matter how long I disappeared. For your constantly open arms, I will forever be grateful <3



Cooper Lars Harshbarger
Zurich, Switzerland
February 2023

Contents

List of figures	VII
List of tables	VIII
Abstract	IX
Zusammenfassung	XI
Nomenclature	XV
1 Introduction	1
1.1 A brief history of cancer	2
1.2 Cancer cells in bodily fluids	4
1.3 Classification of cell isolation methods	6
1.3.1 Label-dependency	7
1.3.2 Passive and active methods	8
1.4 Acoustofluidics	9
1.4.1 BAW devices	10
1.4.2 Applications of BAW acoustofluidics	12
1.5 Isolating cells from fluids using BAW acoustofluidics	12
1.5.1 Stability of an optimal excitation frequency	13
1.6 Measuring cellular properties	15
1.6.1 Material properties of cancer cell	16
1.6.2 Acoustofluidics to measure cellular properties	16
1.7 Thesis outline & research questions	17
2 Theoretical background	19
2.1 Piezoelectric transducers	20
2.2 Piezoelectric equations of state	20
2.3 1D resonance frequency	22

2.4	The Q -factor	23
2.5	Governing equations	24
2.6	Perturbation theory	25
2.7	First-order solutions	26
2.8	Boundary conditions	27
2.9	Acoustic waves in a fluid	29
2.10	The acoustic radiation force	31
2.11	The acoustic contrast factor	32
2.12	Mathematical basis for future applications	35
3	Optical feedback control loop for the precise and robust acoustic focusing of cells, micro- and nanoparticles	37
3.1	Abstract	37
3.2	Introduction	38
3.3	Theoretical background	41
3.3.1	Acoustic radiation force (ARF)	41
3.3.2	Stokes' drag force	42
3.4	Materials & Methods	43
3.4.1	Setup	43
3.4.2	Glass capillary	43
3.4.3	Glass-silicon-glass device	44
3.4.4	Polystyrene particles	44
3.4.5	Feedback control loop (FCL)	44
3.5	Results	48
3.5.1	Improved focusing of 5 micrometer diameter PS particles	50
3.5.2	Higher flow rate for 1 micrometer diameter PS particles	51
3.5.3	600 nanometer diameter PS particle focusing	51
3.5.4	Glass - silicon - glass device and $n = 1, 2$ resonance mode	52
3.6	Conclusions	53
4	Measuring and simulating the biophysical basis of the acoustic contrast factor of biological cells	55
4.1	Abstract	55
4.2	Introduction	56
4.3	Results	58
4.4	Discussion	61
4.5	Methods	64
4.5.1	Theoretical background: Acoustic scattering and streaming	64
4.5.2	Theoretical background: Acoustic contrast factor	66

4.5.3	Setup	68
4.5.4	Glass-silicon-glass device	69
4.5.5	Polystyrene particles	69
4.5.6	Cell culture	69
4.5.7	Trajectory measurement protocol	70
4.5.8	Image analysis	70
4.5.9	Data analysis	71
4.5.10	Numerical model	71
5	Conclusions and Outlook	75
5.1	Focusing objects in fluids	75
5.2	Measuring cellular material properties	77
5.3	Closing remarks	78
A	Appendix to chapter 3	79
A.1	Python code for the feedback control loop	79
A.2	Experimental data	79
A.3	Experimental data readout	80
B	Appendix to chapter 4	81
B.1	Data analysis of the experimental data	81
B.1.1	Data normality	81
B.1.2	Data comparison between observers	82
	Bibliography	85
	Research output	103
	Teaching activities	105
	Curriculum Vitae	107

List of figures

1.1	The metastatic process	5
1.2	BAW acoustofluidic device	11
2.1	PT with polarization density and external electric field	20
2.2	Q-factor	25
2.3	Pressure wave	27
2.4	Visualization of monopole and dipole mode	33
2.5	ARF acting on objects	34
3.1	FCL setup	39
3.2	Linewidth calculation	48
3.3	Focusing results	50
3.4	Focusing of cells in lambda half and lambda modes	52
4.1	Setup and measurement protocol of the ACF of a biological cell	57
4.2	ACF comparison of cell lines and treatments	59
4.3	Numerical model of a biological cell	60
4.4	Results of the numerical model of a biological cell	62
B.1	QQ-plots for SaOs-2, fixed SaOs-2 and LM5	83
B.2	Comparison of ACF between two observers	84

List of tables

2.1	Characteristic acoustic impedance values for common materials used in acoustofluidics	29
2.2	Reflection and transmission coefficients for material pairs	29
3.1	Summary of the state of the art methods	40
3.2	Comparison of focusing	49
4.1	ACF of different materials and treated and untreated cell lines	73
B.1	Shapiro test ACF data	82
B.2	Comparison of ACF between two observers	82

Abstract

In the 1990s, thousand-year-old mummies were exhumed at an excavations site in the southern tip of Peru. The exhumed mummies included the mummified body of a woman in her mid thirties who presented an abnormal growth on the bone of her upper arm. Such bone tumors are classified as an orphan disease due to their low prevalence in the general public, have a peak incidence in children and adolescents, and have a high mortality rate. The high mortality rate stems, to a large degree, from cancer cells disseminating from the primary tumor and forming a secondary lesion in a process known as metastasis. Liquid biopsies, such as blood samples, therefore present a unique opportunity to isolate these disseminated tumor cells in order to gain patient specific diagnostic insight. An ideal method to isolate biological cells from liquid biopsies would not require labelling of the sample and would not diminish the cell viability. Acoustofluidics, a contactless and label-free method known to not decrease cell viability, exploits an acoustic field within a fluid cavity to manipulate objects in a fluid. Many variations of acoustofluidic devices have been developed, which include bulk acoustic wave (BAW) devices, where a standing pressure wave determines the position of objects within the fluid cavity of the BAW device. BAW devices have already been tested for the isolation of cancer cells in research settings. Although these preliminary studies demonstrated that BAW devices can be used to isolate cancer cells, there are limiting factors for BAW devices to be employed outside of research settings. This thesis focuses on how BAW devices can be improved to successfully isolate cancer cells from a liquid biopsy and how to measure the dynamic material properties of biological cells.

An actuating element, usually a piezoelectric transducer manually attached to the BAW device, is excited at a frequency at which a standing pressure wave can be established in the fluid cavity. The continuous focusing and subsequently isolation of cancer cells from fluids therefore prerequisites that the optimal excitation frequency to establish a standing pressure wave can be found and dynamically altered. Many approaches are found in literature how to achieve a stable optimal excitation frequency, such as improving the BAW device design and fabrication. These approaches however only optimize the theoretical focusing efficiency. Another approach is to take the real time video feed of the focusing of the objects in the fluid as the control parameter of a feedback control loop (FCL). This thesis details the implementation of a FCL which can dynamically alter the

Abstract

excitation frequency in order to minimize the object distribution, quantified by the light intensity distribution, within the fluid cavity without increasing the cost or complexity of the system. The suggested FCL is not only straightforward and autonomous, it furthermore outperforms a skilled human operator. The FCL performed tasks otherwise difficult, such as focusing 600 nm diameter polystyrene particles in flow, whereas the optical system was the limiting factor to determine how small the objects could be and still be focused. Future work building upon this FCL could include looking into changing the input variable, e.g. transitioning from a video feed to a light sheet, which could reduce the space requirements and could help to bring BAW devices closer to bedside applications. Furthermore, the FCL could be altered for the use in device multiplexing, cell patterning or organoid formation, depending on the input parameter.

Isolating biological cells is however only a first step. An ever growing research field focuses on measuring the material properties of biological cells. Knowing the material properties can lead to an increased diagnostic insight and is crucial information when designing acoustofluidic systems which rely on the relative compressibility and density differences between the object in the fluid and the fluid, which is characterized by the acoustic contrast factor (ACF). The hypothesis is explored if known static material properties of a bone cancer cell line with low and high metastatic potential can be used as a predictor for the dynamic material properties. The cancer cells were placed in an acoustic field and their movement is compared to reference objects in the fluid in order to calculate the dynamic material properties of the cancer cells. The study did not show a difference in the dynamic material properties between the two metastatic potentials. This is highly relevant as the cancer cells used in this study decrease in size as they become more malignant. The higher metastatic potential cancer cells will therefore be harder to manipulate, due to their smaller size but similar ACF, which is a crucial takeaway. Furthermore, this study includes a more in depth analysis, by altering the stiffness of the parental cell line and implementing a numerical model, which demonstrates the influence of various material properties, such as the stiffness, compressibility and density. The insights gained during this thesis highlight the gap in the understanding of the coupling between static and dynamic material properties, which needs to be addressed.

The woman with the bone tumor would not have been cured by acoustofluidic devices. But the research presented here could have helped in detecting her tumor and led to insights about her disease progression.

Zusammenfassung

In den 1990er Jahren wurden an einer Ausgrabungsstätte an der Südspitze Perus tausend Jahre alte Mumien exhumiert. Unter den exhumierten Mumien befand sich auch der mumifizierte Körper einer Frau Mitte dreissig, die einen anomalen Wuchs am Knochen ihres Oberarms aufwies. Solche Knochentumore werden als Waisenkrankheiten eingestuft, da sie in der Allgemeinbevölkerung kaum vorkommen, am häufigsten bei Kindern und Jugendlichen auftreten und eine hohe Sterblichkeitsrate haben. Die hohe Sterblichkeitsrate ist zu einem grossen Teil darauf zurückzuführen, dass sich Krebszellen vom Primärtumor lösen und in einem als Metastasierung bezeichneten Prozess eine sekundäre Läsion bilden. Flüssigbiopsien, wie z. B. Blutproben, bieten daher eine interessante Möglichkeit Tumorzellen zu isolieren, um patientenspezifische diagnostische Erkenntnisse zu gewinnen. Eine ideale Methode zur Isolierung von Zellen aus Flüssigbiopsien würde keine Markierung der Zellen erfordern und die Lebensfähigkeit der Zellen nicht beeinträchtigen. Die Akustofluidik, eine berührungslose und markierungsfreie Methode, von der bekannt ist, dass sie die Lebensfähigkeit der Zellen nicht beeinträchtigt, nutzt ein akustisches Feld um Objekte in einer Flüssigkeit zu manipulieren. Es wurden bereits zahlreiche Varianten von akustofluidischen Geräten entwickelt, darunter auch Bulk Acoustic Wave (BAW)-Geräte, bei denen eine stehende Druckwelle die Position von Objekten im Flüssigkeitshohlraum des BAW-Geräts bestimmen. BAW-Geräte wurden bereits für die Isolierung von Krebszellen in der Forschung getestet. Obwohl diese vorläufigen Studien gezeigt haben, dass BAW-Geräte zur Isolierung von Krebszellen verwendet werden können, gibt es einschränkende Faktoren für den Einsatz von BAW-Geräten ausserhalb von Forschungseinrichtungen. In dieser Arbeit wird untersucht, wie BAW-Geräte verbessert werden können um Krebszellen aus einer Flüssigbiopsie erfolgreich zu isolieren, und wie die dynamischen Materialeigenschaften von biologischen Zellen gemessen werden können.

Ein Antriebselement, in der Regel ein piezoelektrischer Wandler, der manuell am BAW-Gerät angebracht ist, wird mit einer Frequenz angeregt, bei der sich eine stehende Druckwelle im Flüssigkeitshohlraum aufbauen kann. Die stehende Druckwelle bestimmt die Position des Objekts im Flüssigkeitshohlraum. Die kontinuierliche Fokussierung und anschliessende Isolierung von Krebszellen aus Flüssigkeiten setzt daher voraus, dass die optimale Anregungsfrequenz zur Erzeugung einer stehenden Druckwelle gefunden und dynamisch verändert werden

Zusammenfassung

kann. In der Literatur finden sich viele Ansätze, wie eine stabile optimale Anregungsfrequenz erreicht werden kann, z. B. durch Verbesserung des Designs und der Herstellung von BAW-Geräten. Diese Ansätze optimieren jedoch nur die theoretische Fokussierungseffizienz. Ein anderer Ansatz besteht darin, Echtzeit-Videobilder der Fokussierung der Objekte in der Flüssigkeit als Steuerparameter für einen Rückkopplungsregelkreis (feedback control loop - FCL) zu verwenden. In dieser Arbeit wird die Implementierung eines FCLs beschrieben, der die Anregungsfrequenz dynamisch ändern kann, um die Objektverteilung, quantifiziert durch die Lichtintensitätsverteilung, innerhalb des Fluidhohlraums zu minimieren, ohne die Kosten oder die Komplexität des Systems zu erhöhen. Der vorgeschlagene FCL ist nicht nur einfach und autonom, sondern übertrifft auch die Leistung eines erfahrenen menschlichen Bedieners. Der FCL erfüllte Aufgaben die sonst schwierig sind, wie z. B. die Fokussierung von 600 nm Durchmesser Polystyrolpartikeln in der Strömung, wobei das optische System der begrenzende Faktor war, um zu bestimmen, wie klein die Objekte sein können und dennoch fokussiert werden können. Zukünftige Arbeiten, die auf diesem FCL aufbauen, könnten eine Änderung der Eingangsvariablen beinhalten, z. B. den Übergang von einem Videofeed zu einem Laserlichtschnitt, was den Platzbedarf verringern und dazu beitragen könnte, BAW-Geräte näher an Anwendungen am Krankenbett zu bringen. Darüber hinaus könnte der FCL, je nach Eingangsparameter, für die Verwendung bei der Multiplexierung von Geräten, der Zellstrukturierung oder der Bildung von Organoiden geändert werden.

Die Isolierung von Krebszellen ist jedoch nur ein erster Schritt. Ein ständig wachsendes Forschungsgebiet konzentriert sich auf die Messung der Materialeigenschaften von biologischen Zellen. Die Kenntnis der Materialeigenschaften kann zu einem verbesserten diagnostischen Einblick führen und ist eine entscheidende Information bei der Entwicklung von akustofluidischen Systemen, die auf der relativen Kompressibilität und den Dichteunterschieden zwischen dem Objekt in der Flüssigkeit und der Flüssigkeit beruhen, welche den akustischen Kontrastfaktor (acoustic contrast factor - ACF) definieren. Die Hypothese wird untersucht, ob bekannte statische Materialeigenschaften einer Knochenkrebszellkultur mit niedrigem und hohem Metastasierungspotenzial als Prädiktor für die dynamischen Materialeigenschaften verwendet werden können. Die Krebszellen wurden in einem akustischen Feld platziert und ihre Bewegung wurde mit Referenzobjekten in der Flüssigkeit verglichen, um die Materialeigenschaften der Krebszellen zu berechnen. Die Studie zeigte keinen Unterschied in den dynamischen Materialeigenschaften zwischen den beiden Krebszellkulturen mit unterschiedlichem Metastasenpotenzial. Dies ist von Bedeutung, da die in dieser Studie verwendeten Krebszellen mit zunehmender Bösartigkeit kleiner werden. Die Krebszellen mit höherem Metastasierungspotenzial sind daher aufgrund ihrer geringeren Größe,

aber ähnlichem ACF schwieriger zu manipulieren, was eine wichtige Erkenntnis ist. Darüber hinaus beinhaltet diese Studie eine umfassendere Analyse, indem die Steifigkeit der Ursprungszellkultur verändert und ein numerisches Modell implementiert wurde, das den Einfluss verschiedener Materialeigenschaften wie Steifigkeit, Kompressibilität und Dichte aufzeigt. Die gewonnenen Erkenntnisse zeigen, dass es eine grosse Lücke im Verständnis zwischen der Kopplung von dynamischen und statischen Materialparametern gibt, die es zu beseitigen gilt.

Die Frau mit dem Knochentumor wäre durch akustofluidische Geräte nicht geheilt worden. Aber die hier vorgestellte Forschung hätte bei der Erkennung ihres Tumors helfen und zu Erkenntnissen über ihren Krankheitsverlauf führen können.

Nomenclature

Roman alphabet

c	speed of sound	$[\text{m s}^{-1}]$
$d_{k\lambda}, d_{i\mu}$	piezoelectric charge coefficient	$[\text{C N}^{-1}]$
D, D_i	dielectric displacement	$[\text{C m}^{-2}]$
E	external electric field	$[\text{J}]$
E_S	energy stored	$[\text{J}]$
E_{ac}	acoustic energy density	$[\text{J m}^{-3}]$
E_k	electric field	$[\text{N C}^{-1}]$
f	frequency	$[\text{Hz}]$
h	height	$[\text{m}]$
k	viscous wavenumber	$[\text{m}^{-1}]$
k_0	inviscid wavenumber	$[\text{m}^{-1}]$
n	resonance mode number	$[-]$
\mathbf{n}	surface normal	$[-]$
p	pressure field	$[\text{Pa}]$
P	polarization density	$[\text{C m}^{-2}]$
P_{inc}	incident power	$[\text{J s}^{-1}]$
P_L	power loss	$[\text{J s}^{-1}]$
P_R	reflected power	$[\text{J s}^{-1}]$
P_T	transmitted power	$[\text{J s}^{-1}]$
Q	flow rate	$[\text{m}^3 \text{s}^{-1}]$
Q_n	quality factor of the n -th resonance	$[-]$
r	radius	$[\text{m}]$
r_c	critical radius	$[\text{m}]$
R_I	reflection coefficient from material 1 to 2	$[-]$
$s_{\lambda\mu}^E$	mechanical compliance tensor	$[\text{m}^2 \text{N}^{-1}]$

Nomenclature

t	time	[s]
T	period of oscillation	[s]
T_I	transmission coefficient from material 1 to 2	[-]
U	Gor'kov potential	[J]
\mathbf{v}	velocity field	[m s ⁻¹]
\mathbf{v}_2	acoustic streaming velocity	[m s ⁻¹]
V	voltage	[V]
w	width	[m]
Z	characteristic acoustic impedance	[kg m ⁻² s ⁻¹]

Greek alphabet

γ	damping factor	[-]
γ_λ	strain vector	[-]
δ	characteristic viscous boundary layer thickness	[m]
ϵ_{ik}	permittivity constant for mechanical stress	[C ² m ⁻² N ⁻¹]
ϵ_0	vacuum permittivity	[8.85 · 10 ⁻¹² C ² m ⁻² N ⁻¹]
η	dynamic viscosity	[Pa s]
η_B	bulk viscosity	[Pa s]
λ	acoustic wavelength	[m]
ρ	density field	[kg m ⁻³]
σ_μ	stress vector	[N m ⁻²]
φ	scalar velocity potential	[m ² s ⁻¹]
Φ	acoustic contrast factor	[-]
ω	angular frequency	[s ⁻¹]

Operators

$\square \cdot \square$	scalar product
$\langle \square \rangle$	time average
$\nabla \square$	gradient
$\nabla \cdot \square$	divergence

$\text{Re}[\square]$ real part of complex number

Subscripts

\square_0	equilibrium quantities
\square_1	first-order perturbations
\square_2	second-order perturbations
\square_{ARF}	acoustic radiation force
\square_l	lower
\square_u	upper
\square_r	resonance
\square_A	amplitude
\square_I	interface

Superscripts

\square^D	constant dielectric displacement
\square^E	constant electric field
\square^σ	constant stress

Abbreviations & Acronyms

ACF	acoustic contrast factor
AF	acoustofluidic
AFM	atomic force microscope
A.k.a.	also known as
ARF	acoustic radiation force
AS	acoustic streaming
BAW	bulk acoustic wave
BC	boundary conditions
CK	cytokeratin
CT	computed tomography

Nomenclature

CTC	circulating tumor cell
ctDNA	circulating tumor deoxyribonucleic acid
DIRE	deep reactive ion etching
DLD	deterministic lateral displacement
DNA	deoxyribonucleic acid
E.g.	<i>exempli gratia</i>
EMT	epithelial-mesenchymal transition
EpCAM	epithelial cell adhesion molecule
Eq.	equation
ERSPC	european randomized study of screening for prostate cancer
FCL	feedback control loop
FEM	finite-element method
Fig.	figure
ICP	inductively coupled plasma
IfB	Institute for Biomechanics
IMES	Institute for Mechanical Systems
LM5	lung metastasis 5 cell line
LoC	lab-on-a-chip
LW	linewidth
M	material
MEMS	micro-electromechanical systems
MET	mesenchymal-epithelial transition
microRNA	micro ribonucleic acid
MRI	magnetic resonance imaging
MS	microstreaming
μ TASs	miniaturized total analysis systems
PCA	prostate cancer antigen
PET	positron emission tomography
PLCO	prostate, lung, colorectal, and ovarian cancer screening trial
PS	polystyrene
PSA	prostate specific antigen
PML	perfectly matched layer

PT	piezoelectric transducer
PZT	lead zirconium titanate
RBC	red blood cell
RT-DC	real-time deformability cytometry
SaOs-2	Sarcoma Osteogenic-2 cell line
SAW	surface acoustic wave
1D	one dimensional
2D	two dimensional
3D	three dimensional

1

Introduction

Cancer is omnipresent as it arises from the very DNA that defines who we are. The instability of the genome is a characteristic of most cancers [1], whereas cancer is a group of highly heterogeneous diseases [2] which involve abnormal cell growth and the invasion and spreading of cancerous cells to other parts of the body [3]. Due to the inherent genomic instability, together with other instability promoting factors such as carcinogens [4] and radiation [5], one out of three people will be directly affected by cancer [6]. The motivation for this thesis is therefore not hard to find.

Even though this life altering disease is commonplace, layman knowledge of its history and diagnostic methods is limited and definitions used in popular science are imprecise. To introduce a few core concepts and refine definitions, this first chapter of the thesis contains a short historical introduction to cancer in section 1.1. A brief overview on how cancer migrates through the body is presented in section 1.2. Current methods of how to isolate these circulating tumor cells from bodily fluids are described in section 1.3, which leads into the research topic of acoustofluidics, in section 1.4, which is the manipulation of objects in fluids using pressure waves. Bulk acoustic wave devices (BAW) are introduced with a few applications in sections 1.4.1 and 1.4.2. Using BAW devices to isolate cells from a fluid is introduced in section 1.5, with a special focus on how this isolation process can be made more reliable and automated in section 1.5.1. The reliable determination of the optimal excitation frequency is followed by a short overview of how to measure material properties of biological cells, in section 1.6, and how acoustofluidics can complement already known static material properties with dynamic material properties, as seen in section 1.6.2. This chapter is concluded by the thesis outline and the research questions

which arise from the gaps that become apparent when studying the state of the art.

1.1 A brief history of cancer

The Merriam-Webster dictionary defines cancer as

Cancer (ˈkan(t)-sər) *Noun* • [Latin, crab, cancer] a malignant tumor of potentially unlimited growth that expands locally by invasion and systemically by metastasis.[7]

This straightforward definition disguises the complexity of this grotesquely fascinating family of diseases. The word tumor is mentioned in the definition of cancer. Tumors are a neoplasm, which can roughly be translated to new growth [8]. New growths do not necessarily need to be harmful, thus some tumors can be classified as non-malignant or benign [9].¹ The transition from benign, via pre-malignant, to malignant is part of a process in which cells within the tumor have a gain of function allowing them to invade nearby and distant tissue. Once the cellular machinery is exploited for an uncontrollable, potentially unlimited growth, and allows for cancer cell to spread through the body, thus posing a significant health risk, we talk about cancer.

Cancer received its modern name around 400 BC [10], described by early Greek physicians as *Karkinos*, the Greek word for crab, when documenting lumps under the skin that bore resemblance to a crab buried in the sand. The Greek physicians, although introducing much of the nomenclature we are familiar with, were however not the first to report the disease in a medical context. The Egyptian physician Imhotep provides the first described medical case of cancer which dates back to 2500 BC [11], and despite the four and a half millennia that have elapsed since then, cancer is the second most reported cause of death in the USA [12]. To combat this prevalent disease, whereas cancer is an umbrella disease for more than 100 diseases [13], research has gone into the description, detection and treatment of cancer in order to alleviate the burden. Here, burden is meant in the literal sense of a weight being carried, as *onco-*, latinized from the Greek word *ónkos*, roughly translatable to a "bulk, size, swelling, mass, weight" is the namesake of the study of cancer, oncology. Even though one cancerous growth is not the same as another, as there is a high inter- and even intra-patient variability [2], some

¹This does not mean that all benign tumors are not a health risk, as benign tumors can influence the function of vital organs by reducing nutrient uptake and blood flow, increasing hormonal output and/or press on nerves. [9]

fundamental traits have been described. In the *magnum opus* work of Hanahan and Weinberg [3] eight hallmarks of cancer cells are described: "self-sufficiency in growth signals, insensitivity to anti-growth signals, evading apoptosis, limitless replicative potential, sustained angiogenesis, abnormal metabolic pathways, evasion of the immune system, and tissue invasion and metastasis."²

An additional trait not specifically treated by Hanahan and Weinberg are the marks that are left on the body of people afflicted by the disease, even after the demise of the person. Characteristic tiny holes have been found in the shoulder and skull bones of people probably affected by skin or breast cancer [15], leaving a ghostly mark of the burden once carried. These spotted traces lead far back into ancient history. Although not pathologically confirmed, the 2 million year old jawbone of a homo habilis presented the marking of a peculiar form of lymphoma, a tumor developed from lymphocytes, endemic to southeastern Africa which could be considered one of the earliest fossil record of cancer in the human family tree [16]. But these are just traces of this often deadly disease. In the arid Atacama desert in the southern tip of Peru, bodies can be almost perfectly preserved due to a warm breeze consistently blowing across the surface of the clay soil, whereas the clay soil is capable of leeching fluids out of anything buried in it. This led to the nearly perfect mummification of bodies of the Chiribayan tribe, which were excavated in the 1990s and led to some unexpected findings. A woman in her mid-thirties who lived approximately one thousand years ago presented with a bone tumor with radiating spikes on the proximal head of the humerus [17]. Unlike the negative mold of tumors found previously, this is the positive and direct evidence of a tumor in its making, unearthed in the broad daylight of the archaic landscape.

The model organism used for this thesis is a parental bone cancer cell line with a low metastatic potential and its high metastatic potential counterpart. Bone cancers are classified as an orphan disease, due to their low prevalence in the general population and the resulting difficulty in collecting samples. Further confounding is that bone cancers are a heterogeneous group of already rare malignancies. These bone cancers have a high mortality rate and peak in children and adolescents [18, 19]. Of these, osteosarcoma, a bone forming tumor [20], accounts for nearly half of all bone associated tumor cases. The diagnosis is made by radiological investigation and a biopsy is taken for a histological evaluation. If the diagnosis is made at an early stage, meaning that cancerous cells have not spread, the general treatment procedure is pre-operative chemotherapy, surgical resection and post-operative chemotherapy, resulting in a 5-year survival rate of nearly 60%. However, even if major advances have been made despite its

²The two hallmarks "abnormal metabolic pathways and evasion of the immune system" were added in the 2011 to the original six hallmarks of cancer presented in 2000 [14].

classification as an orphan disease, the 5-year survival rate is below 30% if the diagnosis is made after the cancer cells have already spread [21]. Thus highlighting how important an early diagnosis is. The low survival rate can in part be led back to the fact that cancer is usually treated with a one size fits all approach consisting of surgery, chemo- and radiotherapy. There is a shift away from this practise and towards a more patient specific approach under the umbrella term of personalized oncology [22]. A significant question currently being tackled is how to get the information needed in order to treat the specific disease that a patient is suffering from.

1.2 Cancer cells in bodily fluids

There is a plethora of cancer detection methods. Depending on the type of cancer, these methods include visual inspection and tissue biopsies for melanoma [23], cervical smears for cervical cancer [24], considering family history and high risk genes for breast, ovarian, and contralateral breast cancer [25], ultrasonography for breast [26], thyroid [27] and skin [28] cancer, magnetic resonance imaging (MRI) for the detection of breast cancer [29], computed tomography (CT) scan [30] or positron emission tomography (PET) scan [31] for lung cancer, endoscopy for gastrointestinal cancer [32], prostate specific antigen (PSA) [33] and solid biopsies for prostate cancer whereas at least 10 individual samples are suggested per prostate [34] to name not even a fraction of the methods employed, demonstrating the tremendous need and almost frantic search for diagnostic methods. Individual diagnostic methods have limited validity, as seen in the case of prostate cancer, a type of cancer which will effect one out of six men in the USA [35]. A long held gold standard diagnostic method is PSA detection. However the Prostate, Lung, Colorectal, and Ovarian Cancer Screening Trial (PLCO) [36] and European Randomized Study of Screening for Prostate Cancer (ERSPC) prospective studies with 76'693 and 182'000 subjects [37], respectively, concluded that "at best PSA screening modestly decreased prostate cancer-related mortality" [38]. Therefore other diagnostic markers, such prostate cancer antigen (PCA) 3, are suggested to ensure a higher certainty of true positives [39]. The number of true positives can be increased by combining multiple diagnostic methods. Nevertheless, misdiagnosis is common as in the case of breast cancer, the second leading cause of tumor mortality in women in the USA [40], where manual palpation [41], mammography [42, 43, 44] and ultrasound [45] all have demonstrated limitations with dire consequences. And what is true for prostate and breast cancer, is true for other types of cancers as well.

Cancer detection methods can be highly invasive and painful, require complex and expensive equipment, expose patients to radiation, have a size limitation for

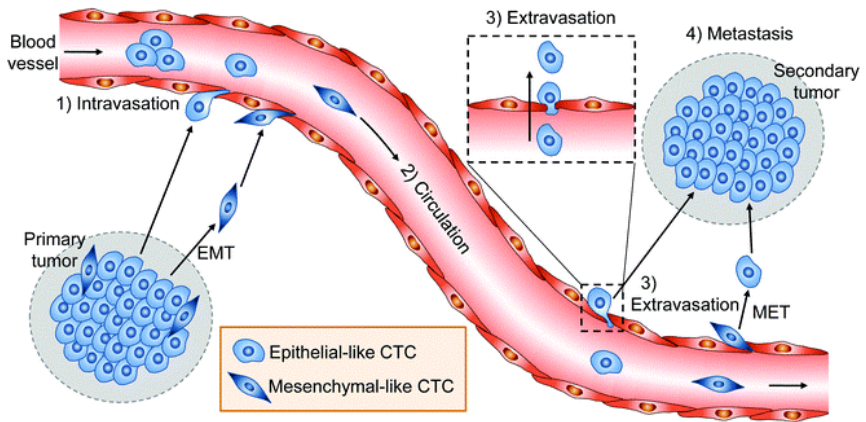


Fig. 1.1: The metastatic process of a tumor of epithelial origin. A primary tumor is formed. The cells forming the tumor continue to replicate and gather more mutations, including an epithelial mesenchymal transition (EMT) which increases the cell's motility within tissue. The cancerous cells can spread through the body via different routes, in the case depicted here by a cell entering the circulatory system, a process termed 1) intravasation. The cancerous cells 2) circulate until they 3) exit the circulatory system and form a 4) secondary tumor. The biological cells sometimes go through mesenchymal-epithelial transition (MET), which is likened to the reverse process of EMT. Reproduced from Ref. [50] with permission from the Royal Society of Chemistry.

detection, or be a combination of any of these traits to name just a few common drawbacks [46, 47, 48]. In addition, even if a highly invasive solid biopsy can be taken, which at least has a high informational value, there is still the risk that one solid biopsy will introduce a single biopsy bias in both time and space [49]. A minimally invasive method with a high informational content could improve the outcome of patients suffering from cancer, and if possible a temporal monitoring of the disease would be striven for.

One hallmark of cancer, mentioned in section 1.1, is the process of cancerous cells spreading throughout the body to form distant lesions, a process that accounts for 90% of cancer related deaths [51]. Linguistically, this process is honored by the Greek term metastasis or beyond standstill, and is non homogeneous between cancer types and is currently not fully understood [52]. What is known, is that cancer cells can be found in many fluids such as pleural effusions [53], lymphatic fluid [54] and cerebrospinal fluid [55] on their way to four common metastatic

sites, the liver, bone, brain and lung [56].³ Therefore, choosing any of these bodily fluids as a liquid biopsy would be interesting, as collecting samples is in most cases minimally invasive, does not require the patient to be in the clinic for a long period of time, and can be done in predetermined time intervals. Another bodily fluid in which cancer cells can be found is blood [59]. The process of cancer spreading through the circulatory system relies on cancer cells disseminating from the primary tumor and intravasation into blood or lymphatic vessels [59] as seen in Fig. 1.1, whereas cancer cells in the cardiovascular system are termed circulating tumor cells (CTC)s [60].

CTCs are very rare, at approximately 1 - 10 CTCs per ml of blood [61], which is in stark contrast to the $5 \cdot 10^9$ erythrocytes and $10 \cdot 10^6$ leukocytes per milliliter of whole blood [62]. Luckily, only approximately one out of forty CTCs gives rise to micrometastasis and 0.01% will develop into macrometastasis [63]⁴. Even though the amount of CTCs found in blood is low, blood samples are easy to obtain in large quantities and therefore offer an interesting opportunity to gain diagnostic insight, if the CTCs can be isolated from the fluid and isolated from other biological cells found in the circulatory system [65].

1.3 Classification of cell isolation methods

There are a vast amount of sorting methods available to isolate objects, such as cancer cells, out of fluids. One way to isolate objects is to employ microfluidics, a technology with its origin in micro-electromechanical systems (MEMS) and is commonly defined as miniaturized total analysis systems (μ TASs) or lab-on-a-chip (LoC) devices. Microfluidics enables the precise manipulation of fluids and rapid sample processing at the sub-millimetre scale [66]. The span of devices for cell isolation using microfluidics is very broad. Although there are many possible classification categories, microfluidic sorting methods are frequently classified by two characteristics [67] namely if they are

- label-dependent or label-free and
- passive or active.

³These common metastatic sites are highly dependent on the type of primary tumor and are not limited to the sites presented here. Furthermore, other bodily fluids can contain cancer cells such as urine [57] whereas the isolation of cancer cells from urine [58] was omitted.

⁴Micrometastasis are 0.2-2 mm in size and are therefore nearly impossible to detect via mammogram, MRI, ultrasound, PET, or CT scans [64].

The following examples are by no means comprehensive, nor does the classification of a method being label-dependent or -free, exclude it being passive or active, thus allowing for all four permutations of the classifications.

1.3.1 Label-dependency

Staining biological tissue can be traced back to at least 1714 [68] when Saffron was used to stain muscle tissue. Repeating this experiment nowadays shows that this Saffron staining is far from effective. Luckily, the technique has been continuously refined over the centuries [69]. In current laboratory settings, the use of tissue staining has become omnipresent, despite the labeling process being a labour intensive task that requires skilled personnel which is susceptible to an observer bias.

One of the staining methods widely used is immunofluorescent labeling, a method with decades of optimization to look back upon [70]. In the case of immunofluorescent imaging, a molecule of interest is targeted with antibodies able to attach to the molecule of interest. The antibody used to detect the molecule can already be tagged with a fluorophore, or be detected by a secondary antibody with a fluorescent tag, resulting in images that are both a pleasure to look at and with a high informational content concerning the localization and abundance of the molecule of interest. The method of molecule detection via an antibody is not limited to attaching a fluorophore. Antibodies, or secondary antibodies, can be linked to all kinds of material, such as bubbles [71], and elastomeric [72] or magnetic objects [73]. Finding a molecule, or biomarker, that is unique to cancer cells and CTCs could therefore aid in the identification and isolation of cancer and the metastatic spreading of cancer. With preference, this biomarker should be present on the cell surface.

One biomarker that can be present on the surface of a biological cell that is frequently targeted is the Epithelial Cell Adhesion Molecule (EpCAM) [74]. However, as can be derived from the name, EpCAM is present on the biological cells that stem from epithelial tissue and therefore should not be in the circulatory system, including CTCs, therefore EpCAM is not limited to CTCs. To aid in the detection, further biomarkers can be used such as cytokeratins (CK) for additional positive selection or CD45⁵ for the negative selection of leukocytes [76]. These additional steps to avoid false negative results are however still not sufficient as healthy blood samples will still contain between 0 - 20% CK positive cells [77, 78]. Furthermore, when cancer cells undergo epithelial-mesenchymal transition (EMT), they can lose the EpCAM marker [79], as seen in Fig. 1.1, which

⁵The initialism CD is used for cluster of differentiation, cluster of designation or classification determinant [75].

increases their motility. Lastly, our model organism is a mesenchymal-derived sarcoma, which unlike epithelial-derived carcinomas, does not typically present the EpCAM marker [80]. A label-free method is therefore highly sought after.

1.3.2 Passive and active methods

Passive methods

Passive methods rely on the geometric design of a fluidic device to separate objects in a fluid from the fluid or from other cell populations in the fluid. Depending on the geometric design, different forces can be exploited. One common design incorporates a spiral, either etched into the device or molded, where inertial forces [81] drive the separation process. In addition, inertial forces can be used in straight channels, using so called pinched flows [82] and hydrodynamic spreading [83]. A further passive separation method is deterministic lateral displacement (DLD) [84], capable of handling a wide size range from exosome up to biological cells with the efficiency determined by the size, shape, deformability, and electrical properties of the objects in the fluid. For DLD, tilted pillar arrays are utilized which generate a fluid bifurcation and thus object dependent streamlines between the pillars [85]. Methods that do not rely on the biophysical difference of cells are transient cellular adhesion [86, 87], slowing down the biological cell when they rollover a functionalized surface, or cellular immobilization [88] which has non-affinity based approaches as well [89]. Another popular design choice is to include geometric constraints in the microfluidic device. One drawback of this sorting by size is that the viability of biological cells can be reduced [90, 91].

Depending on the passive method, the drawbacks are: low flow rates, clogging, biases introduced due to deformability differences and non specific binding or not binding at all [92, 93, 94]. Methods that are label-free and have less affinity for clogging even at high flow rates are therefore desired.

Active methods

Active methods are dependent on an external field. The origin of the external field can be magnetic, electric, optic, etc. When considering magnetic fields, there are both label-free and label-dependent solutions. Label-free solutions can be employed for blood cells with a natural iron content, such as red blood cells [95, 96]. And although macrophages and monocytes are not inherently magnetic, the difference in internalization rate of iron nanoparticles for macrophages and monocytes can be exploited to separate the two cell populations [97], which technically

is a label-free method as the cells passively take up the nanoparticles. Another way to avoid labelling is by exploiting the magnetic properties of ferrofluids to isolate label-free biological cells [98]. But, the vast majority of magnetic field dependent applications are based on label-dependent solutions, where magnetic objects are attached to biological cells [73], thus demonstrating a clear limitation of magnetic field based methods.

Electric fields are exploited based on the intrinsic dielectric properties of cells for the label-free manipulation of biological cells. This method is termed dielectrophoresis and, amongst others, utilizes microelectronic array [99] or insulating posts that create a nonuniform electric field [100]. A common drawback, shared with magnetic fields, is that this method is limited by the interaction of the biological cells with the electric field.

Optic fields have found applications in cell isolation by generating an optic field by a short laser pulse [101] or by creating a potential well that acts or as optical tweezers for cell manipulation [102]. Additionally, optical tweezers can be used to measure fundamental forces within acoustic systems [103, 104, 105]. One limitation of these systems, albeit being label-free, is that the optical manipulation tends to be for one object at a time. This low throughput limits its application where many biological cells need to be analyzed simultaneously.

The presented active methods have all shown promise in their respective fields, but the drawbacks are clear when considering methods that are dependent on labels, specific material properties or are limited by a low throughput. Therefore a label-free method with a higher throughput is desirable.

1.4 Acoustofluidics

Acoustic fields can be exploited to manipulate objects in a fluid. This method of object manipulation in a fluid is contactless, does not need to be dependent on a label and does not diminish the cell viability or proliferation [106].

An acoustofluidic setup requires a device, a function generator and an actuator, which tends to be piezoelectric material. If the experiment needs to be monitored in real time, the most common way is to implement an optical setup with a live video feed. There are other ways to observe an experiment in real time, but optical methods are straightforward in their readout, standardized to build and calibrate. Unfortunately, these optical systems have a large drawback, which is their size, a limitation that is addressed as a part of the outlook.

Although most acoustofluidic setups are similar in their design, there is a wide variability between acoustofluidic devices in which the manipulation of the object takes place. One classification of these devices is made based on how that the energy is instilled into the system which is needed to influence the position of the object in the fluid. Surface acoustic wave (SAW) devices make up one of the two large sub-classes of acoustofluidic devices [107]. Although SAW devices, and their many variations, have shown much promise [108, 109, 110], the focus of this thesis lies on a second large sub-class of acoustofluidic devices, termed bulk acoustic wave (BAW) devices.

1.4.1 BAW devices

Bulk acoustics gets its name from the fact that the whole acoustofluidic device is vibrating and such devices are called BAW devices. BAW devices are capable of manipulating the position of objects within a fluid. A common way to enable this manipulation of the position is to establish standing pressure waves in a fluid cavity.⁶ The process of how to establish such standing pressure waves is detailed in this section and is graphically represented in Fig. 1.2. A voltage potential is applied via a function generator at the electrodes of a piezoelectric transducer (PT) in order to induce mechanical vibrations of the PT. The vibrational amplitude of the PT is linearly related to the pressure amplitude in the device, whereas the acoustic energy density within the fluid cavity scales to the power of two with respect to the pressure amplitude [114]. If the acoustic pressure must be increased beyond the maximal output voltage of the function generator, an amplifier will be inserted in the electric signal pathway between the function generator and the acoustofluidic device. As the PT is mechanically coupled to the BAW device, for instance via a cured electrically conductive epoxy, the mechanical vibrations are transmitted into the device and the whole device starts to vibrate. The vibrations, amongst other effects, cause the wall of the fluid cavity to oscillate, thus creating travelling pressure waves within the fluid cavity. Given the correct excitation frequency, the travelling pressure waves which are reflected off of the hard wall of the fluid cavity are superimposed onto the incoming traveling pressure waves and a standing pressure wave can be established. The standing pressure wave is characterized in part by spatially fixed points of maximal and zero pressure regions. Objects in the fluid interact with the travelling or standing pressure wave within the system and scatter the pressure

⁶Sharp edges in BAW devices can act as a geometric nonlinearity [111] thus inducing acoustic streaming and trapping of objects at certain regions of the sharp edges in the device, but such sharp edge designs [112] and the modeling thereof [113] are out of the scope of this thesis where the focus lies on objects manipulation through standing pressure waves.

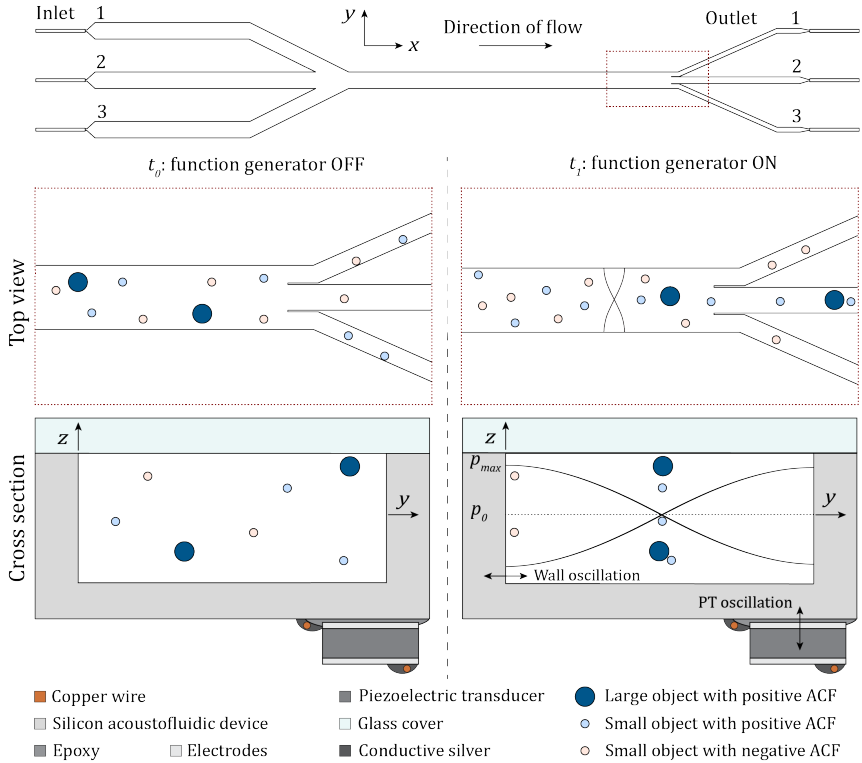


Fig. 1.2: Overview of a BAW acoustofluidic device. The schematic is of a BAW device used for this thesis as seen in Fig. 3.4 and 4.1. There are three inlets, which all can be filled with either a sample solution, buffer fluid or sealed shut. The flow is in the positive x -direction, and the fluid and objects in the fluid can exit via one of the three outlets. The cross section shows a generic BAW device with a top cover made out of glass and a silicon body in which a fluid cavity has been etched. The PT is glued to the silicon base material via a conductive epoxy. The copper wires are electrically and mechanically connected via conductive silver. The solution in the fluid cavity contains small (light blue) and large (navy blue) objects with a positive and small (salmon) objects with a negative acoustic contrast factor (ACF). At t_0 , no voltage is being applied to the PT, and therefore the PT is not oscillating thus the objects are randomly distributed in the fluid and leave through any outlet. At t_1 the function generator is turned on and the PT starts to oscillate. This causes the wall to oscillate and, given the correct excitation frequency, a standing wave is formed. This forces the objects to the pressure nodes, if they have a positive ACF, or to the antinodes, if they have a negative ACF, whereas the larger objects experience a larger force and thus move faster. If a $\lambda/2$ -mode is excited, the positive ACF objects exit the device through outlet 2 and the negative ACF objects exit through outlets 1 and 3. Important to note is that at t_1 the top view only shows one standing pressure wave location, although the standing wave is present within the whole channel. The image is not drawn to scale.

wave. The scattering of the pressure waves results from the relative difference between the density and compressibility of the fluid and the object in the fluid. The difference in density and compressibility between the fluid and the object in the fluid can be reported as an acoustic contrast factor (ACF). The acoustic potential in the system, termed the Gor'kov potential, which can be likened to the gravitational potential of a ball resting on a hillside, can be used to model standing pressure waves in the fluid cavity. The objects in the fluid minimize their potential by migrating to areas where the acoustic Gor'kov potential is minimal, similar to a ball which is denser than the surrounding air rolling down a hill to minimize its gravitational potential, e.g. the regions of zero pressure for an object with a positive ACF. The force acting on the object is termed the acoustic radiation force (ARF) and is, amongst other parameters, dependent on the ACF and the volume of the object. The larger the ACF and the volume, the larger the force acting on the object in the fluid. The ACF can be either positive, e.g. biological cells or metals in water, or negative, e.g. oil or air bubbles in water.

1.4.2 Applications of BAW acoustofluidics

There is a wide variety of BAW device designs geared to specific applications for both inorganic and organic materials. Inorganic materials in fluids can be focused in the pressure nodes, if they have a positive ACF, as demonstrated by the use of acoustofluidics for 3D metal printing [115]. In addition to inorganic materials, acoustofluidics has found many biomedical applications such as in the formation of cell spheroids [116], cell media exchange [117] and patterning of cells for the use in tissue bioengineering [118, 119]. Another common application of BAW devices is the isolation of cell (sub-)populations, which is the method further explored in this thesis. A basic BAW device design for such an application is found in Fig. 1.2 and is the focus of this thesis.

1.5 Isolating cells from fluids using BAW acoustofluidics

Early biomedical applications to isolate biological cells date back to 1986 [120], where traveling waves were used to demonstrate BAW devices for the manipulation of blood samples. The work continued [121, 122, 123] and eventually, first strides were made to isolate cells from fluids using acoustics [124, 125]. After these proof-of-concept studies, a wide range of augmented devices have been used to isolate cancer cells. One method that depends on standing pressure

1.5. Isolating cells from fluids using BAW acoustofluidics

waves⁷ is a label-dependent method which uses elastomers that are attached to biological cells [72], demonstrating that acoustofluidics is not always label-free. The working principle is that the elastomers have a negative ACF and thus the biological cell with the elastomer label can be guided away from other cells into pressure antinodes and therefore be isolated. Acoustofluidics however does not depend on labelling and some of the drawbacks that arise when using labelling techniques were mentioned in section 1.3.1. Utilizing acoustofluidics' full potential of being independent of labels would be advantageous. The label-free isolation of biological cells has been demonstrated by a large group of publications [127, 128, 129, 130]. Exploiting the ACF between biological cells and a fluid has been successfully demonstrated in many cases for the manipulation of cancer cells in a suspension [131, 132, 72, 133, 134].⁸

Important to note, is that the drawbacks of acoustofluidics have so far been neglected in this chapter. It must be mentioned, that acoustofluidics does suffer from similar limitations as other active and passive methods, such as a limited flow rate due to the time needed for the objects to focus and clogging of the devices. Furthermore, air bubbles trapped in the device will fundamentally alter the shape of the acoustic field, preventing any kind of focusing of the objects. Nevertheless, this method does hold of promise for certain tasks and could become an industry standard if certain limitations are tackled. The difficulty to accurately and dynamically determine the optimal excitation frequency needed to maintain the standing pressure wave is one limitation addressed in this thesis.

1.5.1 Stability of an optimal excitation frequency

BAW devices are driven by resonance phenomena which result in standing pressure waves within the fluid cavity. When considering one dimensional line focusing, as demonstrated in Fig. 1.2, the number of lines in which the objects can be focused is given by the desired number of pressure nodes, as objects with a positive ACF with respect to the fluid are forced towards the pressure nodes. The wavelength of the standing pressure wave with the desired number of pressure nodes is determined as two times the width of the fluid cavity divided by the desired number of pressure nodes. The optimal excitation frequency for a desired amount of pressure nodes of a standing pressure wave in a BAW acoustofluidic

⁷Sharp edges in BAW devices can be used to isolate cancer cells [126] but will not be discussed in this thesis.

⁸When considering the broader field of acoustofluidics, including SAW, there are many more examples for cancer cell isolation [135, 136, 137], sometimes in combination with cell material property measurement using methods such as real-time deformability cytometry [138].

device can therefore be determined via the speed of sound of the fluid in which objects are suspended divided by the wavelength with the desired amount of pressure nodes. E.g. for one focusing line and hence one pressure node, the wavelength is twice the width of the fluid cavity and the optimal excitation frequency is the speed of sound of the fluid in the fluid cavity divided by two times the width of the fluid cavity. For two focusing lines and hence two pressure nodes, the wavelength of the standing pressure wave is the width of the fluid cavity and the optimal excitation frequency is the speed of sound of the fluid in the fluid cavity divided by the width of the fluid cavity. These are however idealized cases as there are many reasons for the optimal excitation frequency to deviate from the theoretical resonance frequency such as imprecision during the fabrication, which has many different steps performed in a clean room, and the manual attachment process of the PT. The PT is usually attached manually with an epoxy, damping the system. Furthermore, there is thermal detuning that takes place as the mechanical vibration of the PT is in parts converted into heat, which heats up the BAW device. The resulting frequency shift of the optimal excitation frequency can be up to 2 kHz per °C change [139].

Many attempts have been made to increase the predictability of the optimal excitation frequency, such as increasing the fabrication precision during clean room processes [140]. Or instead of trying to increase the predictability and stability, there is a push to use MEMS production technologies which do not rely on the manual placement of the piezoelectric transducer [141, 142, 143, 144]. However, these devices are more complex to produce and are still in their infancy. In addition, all the proposed solutions do not necessarily result in an improved outcome of an experiment, as they only indirectly influence the outcome of the experiment.

There is an apparent need for an easy to implement control system which can autonomously determine the optimal excitation frequency, without increasing the cost and keeping the manufacturing complexity low. Control systems that have been explored for this use case mainly focus on two parameters. One parameter is the impedance of the system [145, 146, 147] and the other is the electric current [148]. These input parameters however might not lead to an improved outcome as they do not rely on the experimental outcome as an input parameter directly and therefore might not be ideal input parameters [149]. Therefore, attempts have been made to increase the reliability of these parameters to automatically detect the optimal excitation frequency by adding calibration steps [150] or lookup tables [147]. Both attempts increase the manual work load without guaranteeing an increased device performance. A solution, proposed as early as 1996 [151], would be to directly take the real time experimental outcome as the input pa-

parameter. The idea is to design a feedback control loop (FCL), where the live optical output is compared to an ideal optical output. If the current output does not fit the optimal output the frequency is varied until it is. Chapter 3 therefore demonstrates an optical FCL which can automatically and continuously find the optimal excitation frequency based on a desired amount of pressure nodes for the line focusing demonstrated in Fig. 1.2. The FCL does this without an increase of cost or complexity of the system and can be implemented into any optical setup that has a computer controllable frequency generator.

Once these acoustofluidic devices are more reliable and can be run without supervision, the question naturally arises as of what to do with the isolated cells. Amongst others, much research has gone into describing the mechanical phenotype of biological cells.

1.6 Measuring cellular properties

The biomechanical phenotype has gained importance in recent times and is determined by parameters such as the biological cell's density, viscosity and stiffness. Some gold standard methods to measure the stiffness of a cell are magnetic tweezers [152], atomic force microscopy (AFM) [153] and micropipette aspiration [154]. The stiffness is then usually given as the Young's modulus a.k.a the E-Modulus describing linear elastic behaviour of a cell. This linear elastic behaviour indicates a material region where all of the energy that is instilled into the system can be released again without any permanent alteration to the object subjected to the mechanical stress. Although these are powerful and established methods, there are certain limitations; the cells are adherent, only one mechanical parameter of the cell of interest is measured at a time and/or the measurement is based on one region of the biological cell. An alternative method to measure the stiffness, which does not rely on adherent cells, is real-time deformability cytometry (RT-DC) [155].

Although these methods have led to a vast catalog of stiffness data for various cell types in adherent and non-adherent states, the reported material properties stem from (quasi-)static measurements. The dynamic material properties of cells are increasingly important for the use in oncotripsy [156, 157], ultrasound neuromodulation [158, 159] and sonogenetics [160]. Values of interest for these applications are, for instance, the dynamic compressibility or the ACF. The compressibility is the inverse of the bulk modulus, a value that is derived from forces acting on the whole body of the biological cell. The relative dynamic compressibility and the relative density of the object with respect to the surrounding fluid are the two components that define the ACF. The ACF can be

either positive or negative and the larger the absolute value, the more the object will interact with the acoustic field. This interaction with the acoustic field will determine if the cells can be isolated from other cells in a fluid and is therefore particularly interesting when considering applications of isolating cells from fluids.

1.6.1 Material properties of cancer cell

Some solid tumors, such as breast and prostate tumors, can be felt by manual palpation [161, 162, 163], if the tissue of the solid tumors is statically stiffer than the healthy tissue around it [164, 165, 166, 167], whereas stiffer tumors usually indicate a less favorable outcome [168]. One notable exception are Osteosarcomas, which arise from bone which is the hardest tissue in the body [169] and are therefore weaker than their tissue of origin [170]. This is relevant for this thesis, as the origin of the primary tumor of the Sarcoma Osteogenic (SaOs)-2 cell line used in this thesis is a bone, whereas the location of the primary tumor was not reported [171].

Conversely to the stiffness increase of the solid tumors and the less favorable outcome of stiffer solid tumors, an increase of the metastatic potential is correlated to a decrease the stiffness of the cancer cell [172, 173]. This gives rise to a biomechanical difference between healthy cells and cancer cells, and between sub-populations of cancer cells with different metastatic potentials, which can be exploited. The model cell lines that were used in this thesis follow the pattern that higher metastatic potential cells have a decreased static E-modulus [153].⁹

1.6.2 Acoustofluidics to measure cellular properties

BAW acoustofluidics could be harnessed to determine dynamic material properties of cells and compare them to the already known static material parameters in order to give a qualitative assessment of the relevance of static material properties to predict dynamic material properties. A dynamic material property, which is

⁹There is much controversy around the topic of tumor mechanics, already starting with fundamental questions about the terminology of stiffness, solid and interstitial stress and which role each of these three components play in the promotion of tumor growth and metastasis [174, 175] which is out of the scope of this thesis. For interested readers, the review by Mohammadi and Sahai [176] gives a great overview of the biological basis, otherwise completely neglected in this thesis, of the tissue stiffening, the clinical relevance of the stiffening and a quick note on the paradox of how solid tumors tend to be stiffer than their environment, but the cells within the tumor tend to be less stiff than their undifferentiated counterparts, and if the stiffening of the tumor environment might even be a key factor for cancer cells to increase their metastatic potential [168].

relative to the fluid in which the objects are suspended, that can be measured with acoustic fields is the ACF. The ACF can be determined by measuring dynamic compressibility [177, 178, 179] and complementing the measurement with the density, whereas the density is assumed [177], or measured with methods such as a neutrally buoyant sample [178] or defocusing of the particle during sedimentation [179]. Combined, these measurements [177, 180, 178, 179, 181] have led to some insights to the dynamic behaviour of cells, as summarized in Table 4.1.

However, the comprehensive overview of the ACF in Table 4.1 was not straightforward to compile. One, because the data was not always given as an absolute value and had to be read from a graph. Two, the dynamic compressibility was given together with the density of the biological cell, but the fluid in which the measurement was made was not reported. Thus the ACF is estimated based on an educated guess of the fluid. In addition, although the mechanical properties of biological cells were altered [178] and cancer cell lines with different metastatic potential [177] were analyzed, no direct link to the underlying cell mechanics has been made in literature.

Little is known about the correlation between the static stiffness of the biological cell and the ACF. Chapter 4 tries to shine light into this developing area of research by selectively increasing and decreasing the cellular stiffness of a biological cell and comparing the ACF of the treated biological cells to untreated biological cells. The change of ACF observed would, based on the known stiffness difference between the low metastatic bone cancer cell line and its higher metastatic potential counterpart, lead to a change of the ACF, but this was not observed. Therefore the parameter space was explored to illustrate that biological cells are poorly represented in the dynamic domain by just considering one static material parameter.

1.7 Thesis outline & research questions

The acoustic manipulating of exosomes, isolating cells from pleural effusion samples and novel designs for acoustofluidic devices capable of programmable pumping, mixing, cell focusing and trapping, are some applications that were looked into during the duration of this thesis. This thesis however focuses on how to use acoustofluidics to isolate and measure the material properties of bone cancer cells from a liquid biopsy. Therefore only two research questions will be discussed in greater detail in this thesis:

1. Is there a way to continuously and autonomously excite a PT at the excitation frequency optimal for line focusing, as seen in Fig. 1.2?

2. Can cancer cells be isolated from fluids, with the only prior knowledge about the biological cell being their static material properties?

The mathematical framework needed to understand acoustofluidic phenomena is introduced in chapter 2. The theoretical background is concisely stated, but still comprehensive enough that current applications of acoustofluidics can be described. This mathematical framework can aid in providing a rough estimate if a BAW device design will be able to manipulate a certain type of object. This chapter can further act as an insight to determine current obstacles and help evaluate solutions to overcome these obstacles in order to push the usability of acoustofluidic devices even further.

With an introduction to acoustofluidics as a whole and the theoretical framework having been established, the first research question of an automated way to find and dynamically alter the optimal excitation frequency for a BAW device is answered for specific cases in chapter 3.

The second research question is discussed in chapter 4 and focuses on what we can learn about cancer cells being measured by acoustic fields and what the general implications could be for acoustics based applications, for applications beyond acoustics, and for biological tissue beyond single cancer cells. Thus indicating where current limitations of gold standard methods are, where acoustophoresis fits in, and where it does not.

Lastly, the thesis concludes by placing the introduced work in a broader context of its usefulness to the acoustofluidic and greater scientific community. Based on previous research and the research presented in this thesis, an attempt is made to inspire future research into this topic, to continue to push the limits of acoustofluidics, which still has untapped potential.

2

Theoretical background

To observe the phenomena of acoustofluidics and to operate an acoustofluidic device, a fundamental mathematical understanding of acoustofluidics is not strictly necessary, which is practical if the technology wants to transition out of research settings. However, advanced knowledge is needed in order to design acoustofluidic devices, as this knowledge helps understand why certain designs produce the desired phenomena and, equally important, what the limitations might be. The purpose of this chapter is to define the parameter space in which experiments can be conducted, and what expected outcome can be reached.

The acoustic phenomena exploited in the examples in chapter 1 all depend on energy to be instilled into the system. Therefore, section 2.1 gives an overview of the driving element of acoustofluidics, piezoelectric transducers (PT)s. This includes a brief overview of the choice of material and the piezoelectric effect. This is followed by the piezoelectric equations of state in section 2.2. An example of how to determine the 1D resonance frequency is given in section 2.3 with a subsequent practical tip for PT selection. The quality of resonance is shortly described in section 2.4. After the actuation method is mathematically described, the governing equations of fluid motion are introduced in section 2.5. These are simplified in section 2.6 to yield first-order solutions presented in section 2.7 which together with the boundary conditions in section 2.8 are used to describe the acoustic pressure wave in a fluid in section 2.9, with a focus on standing pressure waves. Based on these mathematical formulations, the movement of an object through a fluid can be determined as shown in 2.10 by deriving the force exerted by the acoustic field and from this the material parameters can be described as seen in section 2.11.

2.1 Piezoelectric transducers

The acoustic field within an acoustofluidic device which is exploited to observe the acoustic phenomena described in chapter 1 is established by an actuating element. In many cases these actuators are PTs. PTs are used in applications that need a high precision oscillatory frequency such as ultrasound devices [182] and quartz watches [183]. Depending on the application, PTs are made from crystals or ceramics. Crystalline piezoelectric materials are used in watches due to their high vibrational stability over time. The disadvantages of crystalline material is that the vibrations produced are generally small and thus unsuitable for applications in BAW acoustofluidics.¹ Ceramic materials, albeit being less vibrationally stable, are therefore chosen as the vibrational amplitudes are larger [184]. Piezoelectric materials can maintain an internal polarization without an external electric field. The piezoelectric effect is defined by

$$\mathbf{D} = \epsilon_0 \cdot \mathbf{E} + \mathbf{P} \quad (2.1)$$

whereas \mathbf{D} is the dielectric displacement, ϵ_0 is the permittivity in vacuum, \mathbf{E} is external electric field and \mathbf{P} is the polarization density as seen in Fig. 2.1.

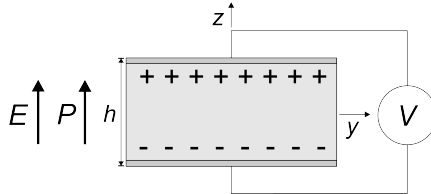


Fig. 2.1: A PT, with the height h and electrodes on the top ($z = +h/2$) and bottom ($z = -h/2$) is attached to a voltage source V with the direction of the electric field \mathbf{E} and polarization density \mathbf{P} indicated.

As energy is stored due to the electrical and mechanical properties of the PT, an external electric field can induce a mechanical deformation of the PT and thus movement of the PT can be induced.

2.2 Piezoelectric equations of state

The dielectric polarization equation 2.1 only describes the piezoelectric effect. To describe the motion of the PT the piezoelectric equations of state need to be formulated

¹SAW devices often use crystalline Lithium Niobate as PTs.

2.2. Piezoelectric equations of state

$$\gamma_{ij}(\sigma_{kl}, E_m) = \sum_{k=1}^3 \sum_{l=1}^3 s_{ijkl}^E \sigma_{kl} + \sum_{m=1}^3 E_m d_{ijm}, \quad (2.2)$$

$$D_n(\sigma_{kl}, E_m) = \sum_{k=1}^3 \sum_{l=1}^3 d_{nkl} \sigma_{kl} + \sum_{m=1}^3 \varepsilon_{mn}^\sigma E_m \quad (2.3)$$

where $\gamma_{ij}(\sigma_{kl}, E_m)$ is the mechanical strain, s_{ijkl}^E is the mechanical compliance, σ_{kl} is the mechanical stress, d_{ijm} and d_{nkl} are the piezoelectric charge coefficient, E_m is the electric field, $D_n(\sigma_{kl}, E_m)$ is the dielectric displacement and ε_{mn} is the permittivity constant for mechanical stress, i, j and $n = 1, 2, 3$, the superscript \square^E and the superscript \square^σ denote measurements under constant electric field and constant stress, respectively. The amount of subscripts can be reduced using [185]

ij	11	22	33	23, 32	13, 31	12, 21
λ	1	2	3	4	5	6
kl	11	22	33	23, 32	13, 31	12, 21
μ	1	2	3	4	5	6

Using the abbreviated subscripts and the symmetry of the stress and strain tensors, the piezoelectric equations of state can be written in matrix-vector notation

$$\begin{bmatrix} \gamma_1 \\ \gamma_2 \\ \gamma_3 \\ \gamma_4 \\ \gamma_5 \\ \gamma_6 \end{bmatrix} = \begin{bmatrix} s_{11} & s_{12} & s_{13} & s_{14} & s_{15} & s_{16} \\ s_{21} & s_{22} & s_{23} & s_{24} & s_{25} & s_{26} \\ s_{31} & s_{32} & s_{33} & s_{34} & s_{35} & s_{36} \\ s_{41} & s_{42} & s_{43} & s_{44} & s_{45} & s_{46} \\ s_{51} & s_{52} & s_{53} & s_{54} & s_{55} & s_{56} \\ s_{61} & s_{62} & s_{63} & s_{64} & s_{65} & s_{66} \end{bmatrix} \cdot \begin{bmatrix} \sigma_1 \\ \sigma_2 \\ \sigma_3 \\ \sigma_4 \\ \sigma_5 \\ \sigma_6 \end{bmatrix} + \begin{bmatrix} d_{11} & d_{21} & d_{31} \\ d_{12} & d_{22} & d_{32} \\ d_{13} & d_{23} & d_{33} \\ d_{14} & d_{24} & d_{34} \\ d_{15} & d_{25} & d_{35} \\ d_{16} & d_{26} & d_{36} \end{bmatrix} \begin{bmatrix} E_1 \\ E_2 \\ E_3 \end{bmatrix}, \quad (2.4)$$

$$\begin{bmatrix} D_1 \\ D_2 \\ D_3 \end{bmatrix} = \begin{bmatrix} d_{11} & d_{12} & d_{13} & d_{14} & d_{15} & d_{16} \\ d_{21} & d_{22} & d_{23} & d_{24} & d_{25} & d_{26} \\ d_{31} & d_{32} & d_{33} & d_{34} & d_{35} & d_{36} \end{bmatrix} \cdot \begin{bmatrix} \sigma_1 \\ \sigma_2 \\ \sigma_3 \\ \sigma_4 \\ \sigma_5 \\ \sigma_6 \end{bmatrix} + \begin{bmatrix} \varepsilon_{11} & \varepsilon_{12} & \varepsilon_{13} \\ \varepsilon_{21} & \varepsilon_{22} & \varepsilon_{23} \\ \varepsilon_{31} & \varepsilon_{32} & \varepsilon_{33} \end{bmatrix} \begin{bmatrix} E_1 \\ E_2 \\ E_3 \end{bmatrix}. \quad (2.5)$$

or

$$\gamma_\lambda = \sum_{\mu=1}^6 s_{\lambda\mu}^E \sigma_\mu + \sum_{j=1}^3 E_j d_{j\lambda}, \quad (2.6)$$

$$D_i = \sum_{\mu=1}^6 d_{i\mu} \sigma_\mu + \sum_{j=1}^3 \varepsilon_{ij}^\sigma E_j. \quad (2.7)$$

Using the Einstein summation convention

$$\bar{v} \cdot \bar{u} = \sum_{i=1}^n v_i u_i = v_1 u_1 + v_2 u_2 + \cdots + v_n u_n \quad (2.8)$$

results in the more common form [114]

$$\gamma_\lambda = s_{\lambda\mu}^E \sigma_\mu + d_{k\lambda} E_k, \quad (2.9)$$

$$D_i = d_{i\mu} \sigma_\mu + \varepsilon_{ik} E_k. \quad (2.10)$$

2.3 1D resonance frequency

Equations 2.9 and 2.10 can be used to derive the resonance frequency of a PT. To start off with a simple 1D problem, the following assumptions are made. The PT is circular with electrodes on the top and bottom as in Fig. 2.1. Only the strain in z -direction is considered and shear propagation is omitted. All vector quantities are assumed to be perpendicular to the electrode surfaces so the only constitutive parameters of relevance s_{33} , d_{33} and ε_{33} are in polarization direction. The electrical circuit is assumed to be open, therefore the electric field \mathbf{E} compensates the polarization \mathbf{P} which leads to $\mathbf{D} = 0$. Given this assumptions, Perez *et al.* [186] take equations 2.9 and 2.10 and by solving the resulting partial differential equation with free end boundary conditions come to the resonance frequency f_r

$$f_n = \frac{n}{2h} \sqrt{\frac{1}{s_{33}^D \cdot \rho}} \quad (2.11)$$

where h is the height of the PT, ρ is the density and the superscript \square^D indicates a constant dielectric displacement. The lead zirconium titanate (PZT) Pz26 PTs used during this thesis were purchased from Ferroperm. Plugging in the material property values provided by Ferroperm into Eq. 2.11, assuming a height of 1 mm, and choosing the first harmonic $n = 1$, the resonance frequency is

$$f_1 = \frac{1}{2 \cdot 0.001m} \sqrt{\frac{1}{1.05 \cdot 10^{-11} \frac{m^2}{N} \cdot 7.7 \cdot 10^3 \frac{kg}{m^3}}} = 1.758 \text{ MHz}. \quad (2.12)$$

The complexity of deriving the resonance frequency, even for a strongly simplified case, can already be seen from the numerous assumptions that need to be made. As this thesis aims to be close to applications in acoustofluidics, therefore an alternative method to estimate the resonance frequency is provided. Ferroperm provides a solver for the resonance frequencies of a PT of arbitrary geometry for all materials that they offer. The resonance frequency of a disc Pz26 PT with a diameter of 1.12 mm and a height of 1 mm has the first thickness resonance mode at 1.758 MHz, which corresponds perfectly to the result of Eq. 2.12. Furthermore the first planar resonance is given at 1.973 MHz, so the calculator even gives more information that is closer to applications. Not indicated by the solver is that higher order harmonics are possible as well and here is where purely relying on a solver without an understanding of the fundamentals is a pitfall which needs to be avoided.

If the aim is to fully describe a BAW device, it would be useful to start with simple derivations such as the one presented by Perez *et al.* [186] and when understood continue to more general problems. For users of acoustics more focused on applications, this thesis suggests another approach. The first step would be to define the width of the fluid cavity as this automatically defines the range of optimal excitation frequencies needed for object manipulation as seen in Eq. 2.46. Next a solver, for instance the one provided by Ferroperm, could be used to estimate the correct dimensions of the PT, with the frequency defined by Eq. 2.46 being similar or equal to the resonance frequency of the thickness mode of the PT, whereas the mathematical framework presented here might help in providing an educated guess of the optimal dimensions of the PT. Any fabrication imprecision and thermal detuning which would lead to a miss-match of the resonance frequency of the fluid cavity and PT chosen can then be handled by a FCL as presented in chapter 3.

2.4 The Q -factor

As Eq. 2.11 demonstrates, there is an infinite amount of resonance frequencies. These resonance frequencies can be characterized via the dimensionless quality (Q)-factor [149], which describes the ratio of stored to dissipated energy in a given cycle

$$Q := 2\pi f_r \cdot \frac{E_S}{P_L} \quad (2.13)$$

where E_S is the energy stored, P_L is the power loss, and f_r is the resonance frequency at which the measured response is maximal. Important to note, is that each resonance frequency has its own Q -factor. The magnitude of the Q -factor varies significantly between resonances, and must therefore be determined for each resonance frequency

$$Q = \frac{f_r}{\Delta f} = \frac{f_r}{f_u - f_l}. \quad (2.14)$$

whereas the lower f_l and the upper frequency f_u are chosen dependent on the method of measurement. For both admittance [187] and displacement [114] measurements of the Q -factor, f_l and f_u are chosen as

$$f_{l,u} \left(\frac{\text{maximal admittance}}{\sqrt{2}} \right) \quad (2.15)$$

and

$$f_{l,u} \left(\frac{\text{maximal displacement}}{\sqrt{2}} \right), \quad (2.16)$$

respectively. Interesting to note is that, even though f_l and f_u are chosen in a similar manner, the Q -factors measured with displacement measurements are reduced by approximately 20% when compared to Q -factors measured from admittance measurements. The choice of the frequencies is graphically represented in Fig. 2.2.

The resonance frequency of the bulk PT actuator is an important starting point to design BAW devices, as the mechanical vibrations of the PT reach maximal amplitudes which are orders of magnitudes larger than at off resonance frequencies. A BAW device however is comprised of an actuator and a fluid cavity. In order to further the mathematical understanding of acoustofluidic devices, the governing equations of fluids are introduced, which lead to the basic requirements to establish standing pressure waves in a fluid cavity.

2.5 Governing equations

The applications of acoustofluidics introduced in chapter 1 are based on acoustic forces acting on objects in a fluid. For the case of the motion of a viscous fluid, the governing equations are the compressible Navier-Stokes equation

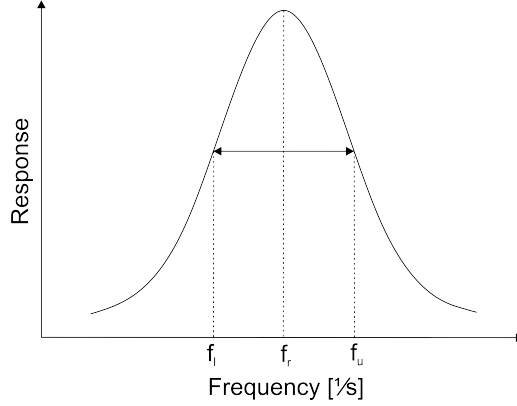


Fig. 2.2: Graphical explanation on how to chose the correct frequencies depending on the method chosen to acquire the data. The method how to chose f_l and f_u varies between measurement methods. f_r however always corresponds to the largest response, independent of the measurement method [149].

$$\rho \left[\frac{\partial \mathbf{v}}{\partial t} + (\mathbf{v} \cdot \nabla) \mathbf{v} \right] = -\nabla p + \eta \nabla^2 \mathbf{v} + \left(\eta_B + \frac{\eta}{3} \right) \nabla (\nabla \cdot \mathbf{v}), \quad (2.17)$$

and the kinematic continuity equation

$$\frac{\partial \rho}{\partial t} = -\nabla \cdot (\rho \mathbf{v}) \quad (2.18)$$

whereas $\rho(x, y, z, t)$ is the density field of the fluid, $\mathbf{v}(x, y, z, t)$ is the velocity field, η the dynamic shear viscosity, η_B is the bulk viscosity, $p(x, y, z, t)$ the pressure field and t is a time variable. It is important to note that the fluid is assumed to be barotropic

$$p = p(\rho). \quad (2.19)$$

2.6 Perturbation theory

Eq. 2.17, 2.18 and 2.19 are general and can be simplified. In order to reduce the complexity of the governing equations, the perturbation theory [188] gives an approach to linearize the equations around an equilibrium state. It is assumed that

$$|\rho_1| \ll \rho_0, \quad |p_1| \ll \rho_0 c_0^2, \quad \text{and} \quad |\mathbf{v}_1| \ll c_0, \quad (2.20)$$

where c_0 is the speed of sound of the fluid. If these assumptions hold true, the fields can be decomposed into their equilibrium state and n -th order perturbations and are given by

$$p = p_0 + p_1 + p_2 + \dots, \quad (2.21)$$

$$\rho = \rho_0 + \rho_1 + \rho_2 + \dots, \quad (2.22)$$

$$\mathbf{v} = \mathbf{v}_0 + \mathbf{v}_1 + \mathbf{v}_2 + \dots \quad (2.23)$$

where the equilibrium states are denoted by the index 0 and the fluid can be assumed to be quiescent

$$\mathbf{v}_0 = \mathbf{0}. \quad (2.24)$$

2.7 First-order solutions

The zeroth-order terms are defined as the equilibrium states and can be expanded upon with higher-order terms. When considering the first-order perturbations and neglecting any higher order perturbations ($2 \dots n$) the equations 2.17 and 2.18 can be written as

$$\rho_0 \frac{\partial \mathbf{v}_1}{\partial t} = -\nabla p_1 + \eta \nabla^2 \mathbf{v}_1 + \left(\eta_B + \frac{\eta}{3} \right) \nabla (\nabla \cdot \mathbf{v}_1), \quad (2.25)$$

$$\frac{\partial \rho_1}{\partial t} = -\rho_0 \nabla \cdot \mathbf{v}_1, \quad (2.26)$$

where ($\square_1 \cdot \square_1$) terms are neglected due to smallness. Furthermore, the first-order density is related to the pressure through the equation of state

$$\rho_1 = \frac{1}{c_0^2} p_1. \quad (2.27)$$

The first-order fields are assumed to have a harmonic time-dependency which can be expressed by the factor $e^{-i\omega t}$, where ω is the angular frequency. Using the time harmonic ansatz, the fields can be written as

$$p_1(x, y, z, t) = \tilde{p}_1(x, y, z) e^{-i\omega t}, \quad (2.28)$$

$$\mathbf{v}_1(x, y, z, t) = \tilde{\mathbf{v}}_1(x, y, z) e^{-i\omega t}, \quad (2.29)$$

$$\rho_1(x, y, z, t) = \tilde{\rho}_1(x, y, z) e^{-i\omega t}. \quad (2.30)$$

The tilde over complex amplitudes of the pressure, velocity and density fields is introduced in order to highlight that $\tilde{\square}_1(x, y, z, t) \neq \tilde{\square}_1(x, y, z)$.

2.8 Boundary conditions

Acoustofluidic devices usually consist of many different materials. One way to characterize the materials used are through their characteristic acoustic impedance Z

$$Z = \rho_0 c_0 \quad (2.31)$$

which is an equation that holds true for both solids and fluids. If two arbitrary materials M_1 and M_2 , with Z_1 and Z_2 , respectively, are placed in contact with each other, there will be an acoustic interface between them as seen in Fig. 2.3.

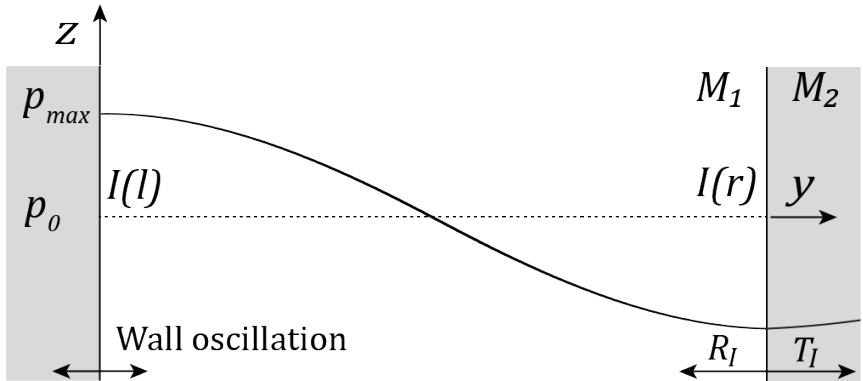


Fig. 2.3: Pressure wave between two materials M_1 (white) and M_2 (grey), with Z_1 and Z_2 , respectively. An oscillation at the wall, defined by the interface on the left-hand side $I(l)$ creates a pressure wave within the fluid. The travelling pressure wave with the pressure amplitude $p = p_{max}$ propagates in positive y -direction until the wave meets the wall on the right-hand side. At the right-hand side interface $I(r)$, the wave is then reflected R_l and transmitted T_l based on the reflection and transmission coefficients for the material combination. The transmitted wave can have an altered wavenumber, which is dependent on the speed of sound of the material M_2 .

Considering a one dimensional case, this interface will have characteristic reflection R_l and transmission T_l coefficients for power

$$R_I = \left(\frac{Z_2 - Z_1}{Z_2 + Z_1} \right)^2 = \frac{P_R}{P_{inc}}, \quad T_I = \frac{4Z_1 Z_2}{(Z_1 + Z_2)^2} = \frac{P_T}{P_{inc}} \quad (2.32)$$

where the subscript \square_I denotes the interface, P_R is the reflected power, P_{inc} is the incident power, P_T is the transmitted power and the power in the system is assumed to be conserved

$$R_I + T_I = 1. \quad (2.33)$$

For two materials with a similar acoustic impedance $Z_1 = Z_2$ the wave gets fully transmitted as $T_I = 1$, as is commonly the case for the interface between the actuating element and the acoustofluidic device. This acoustic matching is important to facilitate the power transfer which would otherwise lead to the heating of the actuating element, a low signal-to-noise ratio, and signal distortion [189]. Other conditions found in acoustofluidics are the hard wall and soft wall boundary conditions (BC), where the interface is between the fluid cavity and the acoustofluidic device.

Soft wall BC: If the wall is considered to be acoustically much softer than the fluid, this can be approximated by

$$\frac{Z_{wall}}{Z_{fluid}} \rightarrow 0 \quad (2.34)$$

which results in $R_I = 1$ and $T_I = 0$. The acoustic wave and thus the energy is reflected and remains in the fluid. This can be expressed as the relation of the pressure at the interface as

$$p_1 = 0. \quad (2.35)$$

Hard wall BC: If the wall is considered to be acoustically much harder than the fluid, this can be approximated by

$$\frac{Z_{wall}}{Z_{fluid}} \rightarrow \infty \quad (2.36)$$

and therefore $R_I = 1$ and $T_I = 0$ remains the same as for the soft wall BC. When dealing with BAW acoustofluidic devices made of silicon and glass with a fluid cavity in which the positions of objects in the fluid are manipulated, this hard wall BC is common and can be expressed as

$$\mathbf{n} \cdot \nabla p_1 = 0 \quad (2.37)$$

whereas \mathbf{n} is the surface normal. The above mentioned cases are idealized. The acoustic impedance is for common materials given in table 2.1 and the resulting values for R_I and T_I are given in table 2.2.

Material	Z [$\text{kg m}^{-2} \text{s}^{-1}$]
Water	$1.49 \cdot 10^6$
Air	$0.00034 \cdot 10^6$
Silicon	$19.79 \cdot 10^6$
Glass	$12.59 \cdot 10^6$
PZT	$30.8 \cdot 10^6$

Tab. 2.1: Characteristic acoustic impedance values for common materials used in acoustofluidics taken from [190].

Wave from <i>material</i> to <i>material</i>	R_I	T_I	Approximated BC
<i>Water</i> to <i>silicon</i>	0.75	0.25	hard-wall
<i>Water, silicon, PZT</i> to <i>air</i>	1.0	0.0	soft-wall
<i>PZT, glass</i> to <i>Silicon</i>	0.01	0.99	impedance matching

Tab. 2.2: R_I Reflection and T_I transmission coefficients at the interface and the resulting BC for a wave traveling from a *material* to *material*.

Due to the acoustic impedance mismatch at the interface between materials of an acoustofluidics device, incident traveling waves are reflected and the superposition with their reflected wave results in a standing pressure wave. This standing pressure wave between the interfaces can be used to precisely manipulate objects in fluids, and therefore knowing how to establish a standing pressure wave is a crucial step in order to predict object motion.

2.9 Acoustic waves in a fluid

Standing pressure waves in a fluid cavity are the basis for BAW devices. With the BCs being established, and the pressure fields having been introduced, the standing pressure wave is introduced mathematically. Starting from the first-order solutions Eq. 2.25, 2.26, 2.27, with Eq. 2.28, 2.29, 2.30 and assuming an inviscid fluid ($\eta = \eta_B = 0$) and taking the time harmonic ansatz, the Helmholtz equation is

$$\nabla^2 p_1 = -k_0^2 p_1 \quad (2.38)$$

whereas

$$k_0 = \frac{\omega}{c_0} = \frac{2\pi}{\lambda} \quad (2.39)$$

is the inviscid wavenumber and λ is the wavelength. The superposition of two plane propagating pressure waves in opposite direction, for instance in the y -direction, is given by

$$p_1(y, t) = g(y + c_0t) + h(y - c_0t) \quad (2.40)$$

where $g(y + c_0t)$ and $h(y - c_0t)$ are arbitrary functions and Eq. 2.40 is known as the d'Alembert solution. A special case is the superposition of two sinusoidal traveling waves with opposed propagation direction, same amplitude and same frequency. The superposition of these counterpropagating waves results in a plane standing pressure wave. The formation of a standing pressure wave can be expressed by g and h as a harmonic ansatz function

$$g(y + c_0t) = \frac{p_A}{2} e^{-i(k_0y + \omega t)} \quad (2.41)$$

$$h(y - c_0t) = \frac{p_A}{2} e^{i(k_0y - \omega t)} \quad (2.42)$$

with the pressure amplitude $p_A/2$ for each traveling wave, where it is assumed that the pressure amplitude is known for the standing pressure wave built up by the PT. The superposition according to Eq. 2.40 yields

$$p_1(y, t) = \frac{p_A}{2} (e^{-ik_0y} + e^{ik_0y}) e^{-i\omega t} = p_A \cos(k_0y) e^{-i\omega t}. \quad (2.43)$$

Important to note is that for the introduced complex numbers, only the real parts are physically meaningful:

$$\text{Re}[p_1(y, t)] = p_A \cos(k_0y) \cos(\omega t) \quad (2.44)$$

resulting in a standing pressure wave with spatially fixed pressure nodes and antinodes. For this case the frequency can be calculated as

$$f = \frac{c_0}{2\pi} k_0. \quad (2.45)$$

A hard wall BC implies a pressure anti-node at the wall, and therefore a velocity node. If the materials were such that the soft wall BC would apply, there would be a pressure node and a velocity anti-node at the wall in the case of a standing pressure wave. The frequency for a standing pressure wave with hard wall boundary conditions in a BAW device is given by [191]

$$f = \frac{c_0}{\lambda_n} = \frac{c_0 n}{2w}, \quad (2.46)$$

where w is the width of the channel, λ_n is the n -th wavelength and the fluid cavity is between the walls which are located $y = 0$ and $y = w$. E.g. for $n = 1$

the wavelength is double the cavity width w and is termed a $\lambda/2$ -mode. For $n = 2$ the wavelength is the width of the cavity w and is termed the λ -mode.

Determining the frequency at which a standing pressure wave is established is crucial for applications in BAW. To elucidate the largest response possible, it is beneficial to match the frequency at which a standing pressure wave is established with the resonance frequency of the PT for the given boundary conditions. But the theoretical frequencies only give a first indication of an optimal driving frequency. Finding the optimal frequency to drive the PT in order to create a standing pressure wave within a acoustofluidic device is discussed at length in chapter 3, where an automatized method is introduced.

2.10 The acoustic radiation force

Based on the second-order equations of the fluid, standing pressure waves, and the boundary conditions, the forces acting on an object can be calculated. The force results from the interaction between the incoming and scattered wave from the object. This can be described as the acoustic radiation force ARF or \mathbf{F}_{ARF} . The ARF on an object in a fluid can be calculated by integrating the stress vector over the surface $S(t)$ of the object in the fluid

$$\mathbf{F}_{\text{ARF}} = \left\langle \int_{S(t)} \boldsymbol{\sigma} \cdot \mathbf{n}(t) dS \right\rangle. \quad (2.47)$$

whereas $\langle \square \rangle = \frac{1}{T} \int_T \square dt$ denotes the time averaging over an oscillation period $T = 1/f$. Given a fluid that can be assumed to be inviscid ($\eta = \eta_B = 0$), the ARF on a spherical object which is a weak point scatterer with a radius r much smaller than the wavelength $r \ll \lambda$ away from a wall and alone in the system is commonly approximated as the negative gradient of the Gor'kov potential [192]

$$\mathbf{F}_{\text{ARF}} = -\nabla U, \quad (2.48)$$

with the Gor'kov potential

$$U = \frac{4\pi}{3} r^3 \left[f_1(\tilde{\kappa}) \frac{1}{2\rho_0 c_0^2} \langle p_1^2 \rangle - f_2(\tilde{\rho}) \frac{3}{4} \rho_0 \langle \mathbf{v}_1^2 \rangle \right] \quad (2.49)$$

where r is the radius of the object, $\langle p_1^2 \rangle$ the first order time averaged square of the incident acoustic pressure and $\langle \mathbf{v}_1^2 \rangle$ the first order time averaged square of the incident acoustic velocity. Furthermore, the monopole coefficient $f_1(\tilde{\kappa})$ which is related to the relative compressibility and the dipole coefficient $f_2(\tilde{\rho})$ which is related to the relative density. The resulting monopole and dipole scattering modes are visualized in Fig. 2.4. The monopole coefficient f_1 is given by

$$f_1 = 1 - \frac{\kappa_p}{\kappa_0} \quad (2.50)$$

whereas κ_p is the compressibility of the object in the fluid and κ_0 is the compressibility of the fluid. The compressibility of a fluid

$$\kappa_0^{\text{fluid}} = \frac{1}{\rho_0 c_0^2}. \quad (2.51)$$

The compressibility of an elastic solid is however defined as

$$\kappa_0^{\text{solid}} = \frac{1}{K} = \frac{3(1 - 2\nu)}{E} \quad (2.52)$$

where K is the bulk modulus, ν is the Poisson's ratio and E is the Young's modulus. The dipole coefficient f_2 is given by

$$f_2 = \frac{2(\rho_p - \rho_0)}{2\rho_p + \rho_0} \quad (2.53)$$

ρ_p is the density of the object in the fluid. Compared to the monopole mode, which is illustrated by a breathing motion, the dipole mode is comparable to a rigid body oscillation of the object, whereas the oscillation is normal to the wavefront. The coefficients are sometimes also expressed in relative terms

$$f_1(\tilde{\kappa}) = 1 - \tilde{\kappa}; \quad \tilde{\kappa} = \frac{\kappa_p}{\kappa_0}, \quad (2.54)$$

and

$$f_2(\tilde{\rho}) = 2\frac{\tilde{\rho} - 1}{2\tilde{\rho} + 1}; \quad \tilde{\rho} = \frac{\rho_p}{\rho_0}. \quad (2.55)$$

Equation 2.49 is valid for a 3D case, but for simplicity reasons the next section on the ACF will only consider one dimension.

2.11 The acoustic contrast factor

The \mathbf{F}_{ARF} defined in Eq. 2.48 and 2.49 can be simplified to one dimension in the y -direction [194]

$$\mathbf{F}_{ARF} = 4\pi r^3 E_{ac} k_y \sin \left[2k_y \left(y + \frac{w}{2} \right) \right] \Phi(\tilde{\kappa}, \tilde{\rho}) \mathbf{e}_y. \quad (2.56)$$

whereas $k_y = \frac{\omega}{c_0}$ is the wavenumber in an inviscid fluid in y -direction and the acoustic energy density

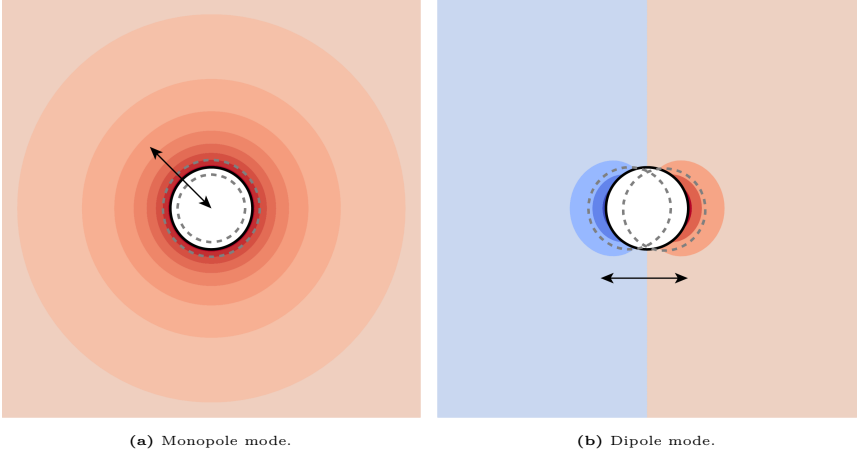


Fig. 2.4: Visualization of monopole and dipole mode of an object in a fluid. The black circle is the unperturbed object. The dashed grey circles are the perturbations caused by an incoming standing pressure wave in horizontal direction. The arrow indicated the direction of the oscillation. Red indicates a positive pressure amplitude and blue indicates a negative pressure amplitude of the scattered waves radiating away from the object. The open source O-SAFT library [193] was used to create the mode shapes and the graphs are generated with $r = 1 \mu\text{m}$, $f = 1 \text{ MHz}$, $c_0 = 1500 \text{ m s}^{-1}$, $\rho_0 = 1000 \text{ kg m}^{-3}$, $\rho_p = 1050 \text{ kg m}^{-3}$, $E = 3.2 \text{ GPa}$, $\nu = 0.35$, and $p_A = 100 \text{ kPa}$.

$$E_{\text{ac}} = \frac{p_a^2}{4\rho_0 c_0^2} \quad (2.57)$$

and Φ is the acoustic contrast factor (ACF)

$$\Phi(\tilde{\kappa}, \tilde{\rho}) = \frac{1}{3} f_1(\tilde{\kappa}) + \frac{1}{2} f_2(\tilde{\rho}). \quad (2.58)$$

A table of relevant Φ values is given in table 4.1, whereas objects with a positive ACF migrate to pressure nodes as seen in Fig. 1.2 and 2.5 and objects with a negative ACF migrate to pressure anti-nodes, given the radius of the object is not below the critical radius r_c , seen in chapter 3 and Eq. 3.7. When an object moves through a fluid, the object will experience a counter force the direction of its motion, which is termed the Stokes' drag, valid in 3D, [195, 196]

$$\mathbf{F}_{\text{str}} = -6\pi\eta r \mathbf{v}_p, \quad (2.59)$$

where \mathbf{v}_p is the velocity of the object. The object velocity v_y in the y -direction can be calculated by balancing the ARF with the Stokes' drag [197].

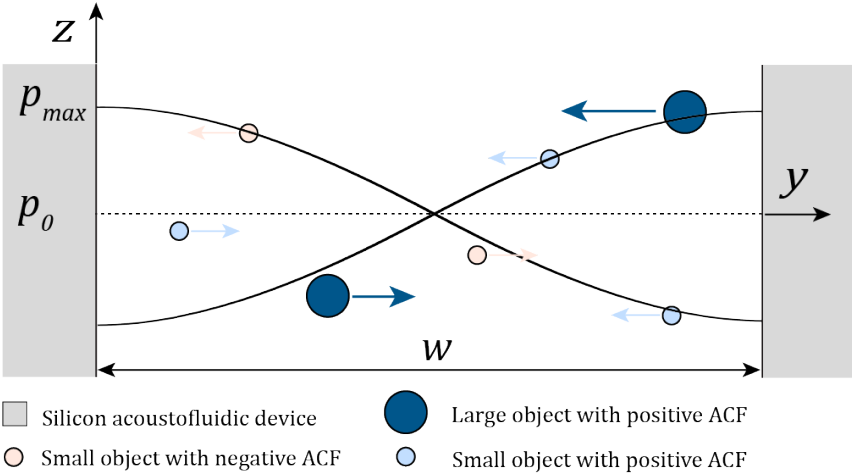


Fig. 2.5: ARF of a λ -half-mode acting on small and large objects with a positive ACF and on a small objects with a negative ACF. The positive ACF objects are pushed to the pressure node in middle of fluid cavity where the pressure is zero. The negative ACF objects are pushed away from the pressure node to the pressure antinode, where the pressure is maximal. The arrows indicate the direction of the ARF, but not the magnitude.

$$v_y = \frac{2\Phi}{3\eta} r^2 k_y E_{ac} \sin \left[2k_y \left(y + \frac{w}{2} \right) \right]. \quad (2.60)$$

with $v_y = \frac{\partial y_p}{\partial t}$ and given an object at starting position y_0 at time $t = 0$, the transverse path $y_p(y_0, t)$ can be calculated [197]

$$y_p(y_0, t) = \frac{1}{k_y} \arctan \left\{ \tan \left[k_y \left(y_0 + \frac{w}{2} \right) \right] \exp \left(\frac{4\Phi}{3\eta} (k_y r)^2 E_{act} t \right) - \frac{w}{2} \right\}. \quad (2.61)$$

Using a reference object with a known ACF, the E_{ac} of the field can be calculated. By inserting the E_{ac} into the Eq. 2.61, the ACF of a object can be determined, which is further discussed in chapter 4.

2.12 Mathematical basis for future applications

The definition of the ACF and how to measure it concludes this chapter and the mathematical framework necessary to understand and exploit fundamental phenomena observed in acoustofluidics. Future applications that will push the limits of acoustofluidics even further will need to rely on a more complex mathematical framework. Some examples of theories put forward that might aid in this regard are where the viscosity [198, 199], thermoviscous effects [200, 201, 202], viscoelastic effects [203, 204], object shape and material [205] and object-object interactions [206] are accounted for.

3

Optical feedback control loop for the precise and robust acoustic focusing of cells, micro- and nanoparticles

This chapter was published as an article in the special issue AI in microfluidics in the journal Lab on a Chip

Harshbarger, C., Gerlt, M., Ghadamian, J., Bernardoni, D., Snedeker, G., Dual, J. (2022). Optical feedback control loop for the precise and robust acoustic focusing of cells, micro- and nanoparticles. Lab on a Chip. Reproduced from Ref. [207] with permission from the Royal Society of Chemistry.

3.1 Abstract

Despite a long history and the vast number of applications demonstrated, very few market products incorporate acoustophoresis. Because a human operator must run and control a device during an experiment, most devices are limited to proof of concepts. On top of a possible detuning due to temperature changes, the human operator introduces a bias which reduces the reproducibility, performance and reliability of devices. To mitigate some of these problems, we propose an optical feedback control loop that optimizes the excitation frequency. We investigate the improvements that can be expected when a human operator is replaced for acoustic micro- and nanometer particle focusing experiments. Three experiments previously conducted in our group were taken as a benchmark. In addition to being automatic, this resulted in the feedback control loop displaying a superior performance compared to an experienced scientist in 1) improving the particle focusing by at least a factor of two for $5\ \mu\text{m}$ diameter PS particles, 2)

increasing the range of flow rates in which $1\ \mu\text{m}$ diameter PS particles could be focused and 3) was even capable of focusing $600\ \text{nm}$ diameter PS particles at a frequency of $1.721\ \text{MHz}$. Furthermore, the feedback control loop is capable of focusing biological cells in one and two pressure nodes. The requirements for the feedback control loop are: an optical setup, a run-of-the-mill computer and a computer controllable function generator. Thus resulting in a cost-effective, high-throughput and automated method to rapidly increase the efficiency of established systems. The code for the feedback control loop is openly accessible and the authors explicitly wish that the community uses and modifies the feedback control loop to their own needs.

3.2 Introduction

The Kundt's tube described in 1866 [208] is based on acoustophoresis, a contactless, label-free, and non-invasive method to actively control the position of particles over a wide range of sizes using acoustic pressure waves.[209]

In 1938 Hillary W. St. Clair filed, to our knowledge, the first patent related to acoustophoresis "Sonic flocculator and method of flocculating smoke or the like".[210] Continued research on both the theoretical as well as the experimental aspect of acoustophoresis has led to a vast number of applications such as acoustic particle levitation,[211] acoustic holograms[212] and tweezers,[213] aiding in 3D mechanical characterization[214] and isolating cancer cells from blood[129] to name only a few.

Despite a long history, a plethora of publications in the field and interesting applications demonstrated in research, only a small number of companies offer products based on acoustic particle manipulation.[215] There are many reasons for this such as the currently imprecise manufacturing which could be tackled by improved cleanroom processes[140] or by improving the predictability or reliability of devices using more complex production methods or designs.[141, 142, 143, 144] As for the enhanced understanding of the fundamental principles of acoustophoresis, aiding in device design, various computational models have been created.[216, 217, 218, 219] Aiding these computational models, deep learning can be used to find a device design that creates a desired acoustic potential.[220]

The beforehand mentioned approaches to improve the performance of acoustic devices place an emphasis on improving the theoretical device performance. When considering a prevalent application of acoustophoresis, focusing micro- and nanometer particles,[221, 222, 223, 224, 225, 226, 227] additional methods have sought to further increase the experimental outcome. A successful outcome is

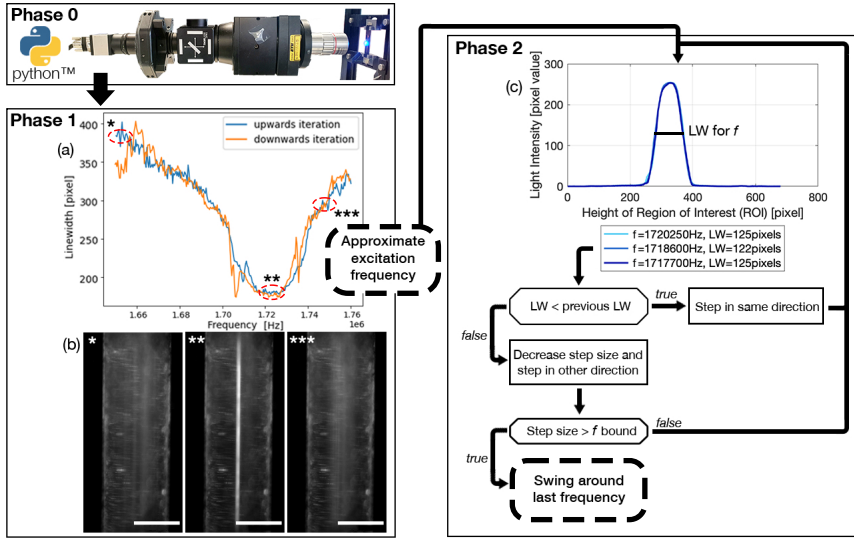


Fig. 3.1: Schematic overview of the feedback control loop (FCL). *Phase 0* initializes the FCL and the video stream from the device being filmed (blue dot) by the uEye camera (grey metal housing above the black arrow on the left) is taken by a screen capture function and fed into the FCL. *Phase 1* (a) Recorded particle linewidths (LW), a measure for particle focusing, for *phase 1* of the FCL using $5\ \mu\text{m}$ PS particles focused in the center of the device by an acoustic standing wave for the frequency range $1.66 - 1.78\ \text{MHz}$ with a $600\ \mu\text{L min}^{-1}$ flow rate. The function generator was controlled by the FCL, sweeping through the frequency spectrum with $400\ \text{Hz}$ steps to find the minimal linewidth. (b) * $t = 0\text{s}$, ** $t = 68\text{s}$, *** $t = 110\text{s}$ are images, where the asterisk (*) correlates the graphical readout of the frequency sweep to the red dashed circles of (a) of the upwards iteration (blue data entries). *Phase 2* on the right indicates how the approximate excitation frequency of *phase 1* is used to initialize *phase 2*, which ultimately leads to the determination of an optimal excitation frequency. For clarity, a safeguard against continuously stepping in the wrong frequency direction is left out of the schematic. (c) 3 different frequencies obtained from *phase 2* are plotted against each other and corresponds to the *phase 2* of (a), indicating the precision of *phase 1* and illustrates that for simple systems, such as a glass capillary and $5\ \mu\text{m}$ PS particles, *phase 1* might be sufficient and that a more precise excitation frequency does not result in a significantly narrower linewidth. White scale bar (b): $500\ \mu\text{m}$

achieved by reducing the influence of acoustic streaming vs. the acoustic radiation force. Due to the size dependent scaling, seen in Eq. 3.2 and 3.6, this becomes increasingly difficult if the particles' size is decreased to below 1 micron. In addition, temperature changes must be taken into account, which result in a detuning of the device and therefore lower pressure amplitudes. An approach is to control

the excitation frequency of the piezoelectric transducer which is enabling the focusing via a feedback control loop (FCL). This is accomplished by measuring the resonance response of the system and thus indirectly effects the outcome of the experiment. Two parameters are currently being used to measure the resonance, which are the impedance of the system[145, 146, 147] or the electric current.[148] The measured resonance behavior of the system is then used to tune the excitation frequency of the driving piezoelectric transducer. These state of the art methods of which parameters can be used to implement a FCL are summarized in table 3.1.

	Measured parameter	Year published
Goddard <i>et al.</i> [145]	Impedance	2006
Suthanthiraraj <i>et al.</i> [146]	Impedance	2012
Kalb <i>et al.</i> [147]	Impedance	2018
Farmehini <i>et al.</i> [148]	Electric current	2021

Tab. 3.1: Summary of state of the art methods.

It however has been noted that these approaches, which are based on measuring electric signals, might not be able to correctly identify the optimal excitation frequency of a coupled system consisting of the piezoelectric transducer and the microfluidic channel.[149] To try and elevate this shortcoming, the system can be characterized *a priori* to an experiment to try and find the corresponding resonance frequencies[150] or an FCL can be combined with a lookup table.[147] However, all methods require additional electrical equipment and while increasing the performance of a system, they only indirectly influence the performance, especially for particles close to the critical radius as actuating the system at resonance does not guarantee an optimal streaming suppression. An optical FCL has been reported only in the context of particle positioning[151] which uses a visual input to control the position of one particle in two dimensions. An optical FCL, which directly takes the desired outcome as the control signal, has not been presented before. Our goal was therefore to expand on the idea of an optical FCL, schematically represented in Fig. 3.1, which directly effects the performance of a system classified by the quality of the particle focusing. The shift from a resonance control to an optical control can also help in finding the optimal excitation frequency when acoustic streaming is present. Thus being able to focus particles that otherwise would be dominated by acoustic streaming. The FCL uses the particle linewidth (LW) as the parameter to optimize, where the LW is the spread of the particles in the microfluidic channel of a device, Fig. 3.2. The FCL can easily be integrated into any preexisting setup that allows for an optical readout during the experiment, increasing the sample throughput

whilst not increasing the cost.

Optically automatizing the determination of an optimal excitation frequency leads to an increase of the acoustic force acting on the particles of interest. This lead to an improved performance of acoustophoretic devices when compared to three benchmark tests[140] by 1) narrowing the focusing of the particles by at least a factor of two for $5\ \mu\text{m}$ PS particles, 2) increasing the range of flow rates in which $1\ \mu\text{m}$ diameter PS particles could be focused and 3) focusing particles with a diameter as small as $600\ \text{nm}$ (Fig. 3.3). The manipulation of such small particles is a significant step, since in state of the art publications, a very complicated setup needs to be utilised to manipulate particles in this size range,[228] or no fluid flow could be applied.[229] Finally, we demonstrate the versatility of the setup by showing two different types of devices and modes of operation (Fig. 3.4) using biological cells. The above mentioned augmented performance, based on automatising the focusing, is needed for applications to be successful outside of laboratory settings. We therefore believe that our novel optical FCL can be used as a foundation to further the development and integration of acoustophoresis into market products.[215, 107] This is in line with the increasing need of simpler and more adaptable lab on a chip devices.[230]

3.3 Theoretical background

3.3.1 Acoustic radiation force (ARF)

The FCL demonstrated in this paper allows to precisely focus particles of interest. This focusing exploits the ARF which, given a spherical particle with a radius much smaller than the acoustic wavelength in an inviscid fluid, is commonly approximated as the negative Gradient of the Gor'kov potential[192]

$$\mathbf{F}_{\text{ARF}} = -\nabla U, \quad (3.1)$$

with the Gor'kov potential

$$U = \frac{4\pi}{3} r^3 \left[f_1(\tilde{\kappa}) \frac{1}{2\rho_0 c_0^2} \langle p_1^2 \rangle - f_2(\tilde{\rho}) \frac{3}{4} \rho_0 \langle \mathbf{v}_1^2 \rangle \right] \quad (3.2)$$

where r is the radius of the particle, ρ_0 is the density of the fluid, c_0 the speed of sound of the fluid, $\langle p_1^2 \rangle$ the first order time averaged square of the incident acoustic pressure and $\langle \mathbf{v}_1^2 \rangle$ the first order time averaged square of the incident acoustic velocity. Furthermore, the monopole coefficient $f_1(\tilde{\kappa})$ which is related to the relative compressibility and the dipole coefficient $f_2(\tilde{\rho})$ which is related to the relative density

$$f_1(\tilde{\kappa}) = 1 - \frac{\kappa_p}{\kappa_0} \quad (3.3)$$

$$f_2(\tilde{\rho}) = 2 \frac{\rho_p - \rho_0}{2\rho_p + \rho_0} \quad (3.4)$$

where κ_p is the compressibility of a particle, κ_0 is the compressibility of the fluid and ρ_p is the density of the particle. A standing wave is required for a large ARF magnitude. The resonance frequency for the n -th ultrasonic resonance mode of a one-dimensional standing wave with hard wall boundary conditions is [191]

$$f_{res}^{1D} = \frac{c_0 n}{2w} \quad (3.5)$$

where w is the width of the channel.

3.3.2 Stokes' drag force

In addition to the ARF, a second force, the Stokes' drag force produced by the acoustic streaming velocity \mathbf{v}_{str} , acts on the particle in the fluid [195, 196]

$$\mathbf{F}_{str} = 6\pi\eta r(\mathbf{v}_{str} - \mathbf{v}_p), \quad (3.6)$$

where η is the dynamic viscosity of the fluid and \mathbf{v}_p the velocity of the particle. In addition to the Stokes' drag force resulting from the acoustic streaming velocity \mathbf{v}_{str} , the Stokes' drag force results from the viscous resistance for particles moving through a fluid and is therefore always present for $\mathbf{v}_p \neq \mathbf{0}$. The Stokes' drag force, no matter the origin, scales with r (Eq. 3.6) and the ARF scales with r^3 (Eq. 3.1). This means that overall the Stokes' drag force always dictates the motion of the particle, but the influence of the Stokes' drag force coming from the acoustic streaming velocity is diminished compared to the ARF as particles get larger. Therefore, there is a radius, termed the critical radius, above which the ARF cannot overcome the Stokes' drag force stemming from the particle motion, but can overcome the Stokes' drag force resulting from the acoustic streaming velocity. This critical radius can be analytically approximated in 1D [191]

$$r_c^{1D} = \sqrt{\frac{3\psi}{2\Phi}} \delta \quad (3.7)$$

where ψ is a geometry dependent factor and the acoustic contrast factor Φ

$$\Phi = \frac{1}{3} f_1(\tilde{\kappa}) + \frac{1}{2} f_2(\tilde{\rho}), \quad (3.8)$$

and the viscous boundary layer δ

$$\delta = \sqrt{\frac{\eta}{\pi\rho_0 f}}. \quad (3.9)$$

Exempli gratia, the 1D analytical critical radius r_c of a polystyrene particle in water, $\Phi \approx 0.165$ at $f = 1.75$ MHz in a rectangular microfluidic channel, therefore $\psi = \frac{3}{8}$, [231] is $r_{c,a}^{1D} = 0.78 \mu\text{m}$. The numerical model for our specific geometry which describes the diminished influence of the acoustic streaming compared to the influence of the ARF described by Gerlt *et al.*, [115] resulted in a numerical critical radius $r_{c,n} = 0.35 \mu\text{m}$. This still does not match our experimental findings as will be seen in table 3.2 and Fig. 3.4, hence providing further evidence that the critical radius for a given system is not known prior to an experiment. [232]

3.4 Materials & Methods

3.4.1 Setup

The setup employed is analogous to the one used in Gerlt *et al.* [115] The fluid flow through a circular glass capillary (76 mm length, 1 mm outer diameter, 0.75 mm inner diameter) and a glass - silicon - glass device (device: 50 mm length, 12 mm width, 1.4 mm thickness; focusing channel: 15 mm length, 1 mm width, 0.2 mm height) was controlled by volumetric syringe pumps (Nemesys, Cetoni). A function generator, connected to the computer running the FCL, (AFG-2225, GW Instek) powered the piezoelectric transducers. The signal from the function generator was amplified (325LA Linear Power Amplifier, Electronics & Innovation) and monitored using an oscilloscope (UTD2025CL, UNI-T). For optical data acquisition a custom made setup from THORLABS consisting of specifically selected parts from the Cerna® series was used. The video feed generated with a 5x objective (M Plan Apo 5x / 0.14, Mitutoyu) and a uEye camera (UI-3160CP Rev. 2.1, iDS, 1920 x 1200 pixels, 60 fps), as shown in Fig. 3.1 *phase 0*, was captured from one of the two computer screens and fed into the FCL running on PyCharm 2021.1.3 (Edu) with Python 3.8.

3.4.2 Glass capillary

In order to compare the device performance as best as possible, the tests were performed with the same glass capillaries, piezoelectric transducers and production procedure that was used by Gerlt *et al.* [115] The glass capillary (TW100-4, World Precision Instruments) has two piezoelectric transducers (10 mm length, 2 mm width, 1 mm thickness, Pz26, Meggitt Ferroperm) glued on using an electrically

Chapter 3. Optical feedback control loop for the precise and robust acoustic focusing of cells, micro- and nanoparticles

conductive Epoxy glue (H20E, Epoxy Technology). Copper cables (0.15 mm diameter) were attached to the piezoelectric transducers and the electrical connection was established with an electrically conductive silver paste.

3.4.3 Glass-silicon-glass device

The glass-silicon-glass device, seen in in Fig. 3.4(c), was produced by bonding a 500 μm thick glass wafer to a 200 μm thick silicon wafer. Channels were patterned onto the exposed silicon wafer using photolithography (resist: S1828, Shipley, 4'000 rpm; developer: AZ351B, Microchemicals). The full thickness of the silicon wafer was etched away with an inductively coupled plasma (ICP) deep reactive ion etching (DRIE) machine (Estrellas, Oxford instruments). Following the etching, a 700 μm thick glass wafer was anodically bonded onto the exposed silicon wafer. The wafer was then diced into individual chips with a wafer saw (DAD3221, Disco corporation). Fused silica capillaries ($164 \pm 6 \mu\text{m}$ outer diameter, $100 \pm 6 \mu\text{m}$ inner diameter, Molex) were inserted into the inlets and outlets of the chips and fixed with a two-component glue (5 Minute Epoxy, Devcon). The piezoelectric transducers, Epoxy glue, wiring and an electrically conductive silver pasted are the same ones used for the glass capillaries.

3.4.4 Polystyrene particles

Green fluorescent polystyrene (PS) particles (microParticles GmbH, Germany) with diameters of $5.19 \pm 0.14 \mu\text{m}$, $1.08 \pm 0.04 \mu\text{m}$ and $600 \pm 20 \text{ nm}$ were used for all experiments in Fig. 3.3 and all experiments were conducted with 0.5% v/v.

Cell culture

The bone cancer cells used is the SaOs-2 cell line. The cell line was kept at the standard 37°C and 5% CO₂ and 95% air. The cell media used is DMEM - F12 Ham (D8437, Sigma) supplemented with 10% fetal bovine serum (10270106, Thermo) and 1% P/S. The cells were passaged when 60% confluency was reached. The diameter of the cells is $15.73 \pm 0.42 \mu\text{m}$ (CellDrop BF, DeNovix) .

3.4.5 Feedback control loop (FCL)

The FCL, shown schematically in Fig. 3.1 and available on Gitlab, is implemented in the widely used programming language Python and is split into 3 phases,

- *Phase 0*: Initialization of the system.
- *Phase 1*: Approximate determination of an optimal excitation frequency.

- *Phase 2*: Precise determination and stabilisation of the optimal excitation frequency.

A highlight of the code is the `ImageGrab` function. This allows the user to continuously capture the image directly from the computer screen of the computer controlling the imaging system in order to use the image for the FCL to determine the linewidth. This ensures that any preexisting optical setup can be utilized. Therefore, the imaging system does not need to be adapted to the FCL, thus being an augmentation without any additional costs. It is recommended to use two monitors, such that the plotting does not interfere with the screen capture. In the following description, `this` typeset was used to highlight variables.

Phase 0: The connection to the function generator is established and all necessary Python libraries are loaded. Libraries required are `pyserial`, `opencv-python`, `keyboard`, `termcolor`, `numpy`, and `matplotlib`. For setups that deviate from the setup demonstrated here, the script needs to be altered in order to accommodate for different function generators. In addition, the parameters for the experiment need to be set, such as where the frequency sweep starts and where it stops, defined as `freq_min`, `freq_max`. `freq_min` and `freq_max` can either be defined manually starting at a frequency defined by experience or calculated using a user defined `percentage` interval. In this phase, the region of interest (ROI) needs to be chosen and the code creates a background image, which is used for a background subtraction later on, if needed. In addition to the listed parameters and working directories, parameter sets for *phase 1* and *phase 2* need to be defined. These parameters depend on the flow rate, input voltage, particle concentration and size to name a few. Exemplary values that were used for the experiments can be found in the code on Gitlab. As to be expected, the time required for each phase highly depends on the set of parameters and the frequency range chosen. *Phase 1* of Fig. 3.1 for instance took ~4 minutes.

The set of parameters that need to be defined for *phase 1* is comprised of: `initial_time_delay_1` which is the initial time delay for system to settle, `frequency_step_size_1` which is the frequency step size, `time_delay_1` which is the time delay between frequency steps.

The set of parameters that need to be defined for *phase 2* is comprised of: `wait_time_transition_2` which is the time delay for the system to settle between *phase 1* and *phase 2*. `frequency_step_size_2` which is the frequency step size. `time_delay_2` which is the time delay between the frequency steps. `threshold` which is the threshold value for a change of direction, if the linewidth has not improved in the past `|threshold|` iterations. `swing_value` which is the value with which the step size is multiplied with after changing the direction

of iteration. The `swing_value` is therefore $\in (0, 1)$. `freq_bound` is the lower frequency boundary for a minimal step size. In our experience, a `|freq_bound| = 20` [Hz] leads to optimal results.

Phase 1: The FCL steps through from the lowest to the highest set frequency and once the highest frequency is reached, starts to step down again, as shown in Fig. 3.1(a), which is the plot generated after *phase 1* is completed. The FCL then automatically sets the frequency to the approximate excitation frequency determined by the best average linewidth from the up- and downward iteration. The linewidth calculation is demonstrated in Fig. 3.2, for the up- and downward iteration. The up- and downward iteration allows for an averaging of the best linewidth to double-check the optimal frequency. The up- and downward iteration shown in Fig. 3.1 is not necessarily needed, as the curves look similar enough, but the lower the flow rate and the smaller the particle size, the more important the up- and downward iteration becomes, as the ARF decreases with decreasing particle size. The theoretical resonance frequency f_{res}^{1D} calculated using Eq. 3.5 can differ from both the empirically chosen frequency and the frequency found by the FCL. This highlights how precarious finding an approximately optimal excitation frequency is, and that even experienced users can introduce human error, especially as many devices show focusing over a multiple hundred kHz range, exemplary seen in Fig. 3.1(a), therefore making it is easy to pick an excitation frequency which is far off from an optimal excitation frequency.

Phase 2: in *phase 1*, the functionality of the FCL is limited to finding an approximate starting value for the optimal excitation frequency. Once the approximate excitation frequency is found, *phase 2* narrows down the range of the optimal excitation frequency, as illustrated in Fig. 3.1(c). To initialize *phase 2*, the FCL takes the linewidth of the approximate excitation frequency determined in *phase 1* and sets the linewidth as the best previous linewidth. Then the FCL starts to iterate downwards with the step size `frequency_step_size_2`. The linewidth for each step (`cur_linewidth`) is compared to the best previous linewidth (`best_linewidth`). If `best_linewidth` is wider than `cur_linewidth`, `best_linewidth` is set to `cur_linewidth`. If `best_linewidth` is narrower than `cur_linewidth` an internal counter (`count`) is increased by 1. This is done until `count = threshold`. Once `count = threshold` is reached, continuing to step in the same direction does not yield a narrower linewidth. Therefore `frequency_step_size_2` is then multiplied by `swing_value`, `count` is set to zero and the FCL steps in the opposite direction with the decreased step size. This process is continued until `frequency_step_size_2` is smaller than `freq_bound`. When `freq_bound` is reached, the step size is kept constant for the remainder of the experiment and the FCL continuously oscillates around the frequency.

This can be used to balance out any fluctuations in concentration, flow rate or temperature, to name a few common disturbances.

It is recommended that for a first rough characterization of the system *phase 1* is run at high flow rates, e.g. $100 \mu\text{L min}^{-1}$ and above, with particle diameters of at least a few micrometer diameter and in a large frequency range, e.g. $\pm 10\%$ of the expected resonance frequency. In a second round of characterisation, the **frequency step sizes** and **frequency range** can be decreased and shifted symmetrically around the approximately optimal excitation frequency and **time_delays** can be increased for an even more precise approximate excitation frequency. The thus found approximate excitation frequency can be constant over multiple days and experiments when using multi micrometer diameter particles. For particles around one micrometer in diameter or smaller it is recommended to use *phase 2*.

Linewidth calculation

The linewidth was chosen as the parameter that the FCL optimizes, and in our case is defined as the spread of particles over the microfluidic channel, thus being a measure for the focusing of the particles. The linewidth is determined differently in *phase 1* and *phase 2*.

In *phase 1* the linewidth is calculated by taking the sum of the pixel values of all the pixels in the direction of flow (indicated by the x -axis in Fig. 3.2(c)) and is plotted over the width of the channel (indicated by the y -axis in Fig. 3.2(c)). The linewidth is then calculated using a Gaussian fit as the region in which 2 standard deviations, or $\sim 70\%$ of the total sum of the pixels, are located. This linewidth readout is then plotted over the frequency range as shown in Fig. 3.1(a).

In *phase 2*, as seen in Fig. 3.1(c), 3.4(e) and (g), the pixel distribution over the whole channel is displayed for a given frequency, where the pixel values range from 0 (pure black) to 255 (pure white). The resulting pixel value is the average pixel value of all the pixels in the direction of flow (indicated by the x -axis in 3.4(e) and (g)) and is plotted over the width of the channel (indicated by the y -axis in 3.4(e) and (g)). The linewidth is calculated the same way as for *phase 1*, but multiple frequencies are plotted, providing live output of how the particle distribution is evolving. The linewidth is given in the legend, with the corresponding frequency.

Chapter 3. Optical feedback control loop for the precise and robust acoustic focusing of cells, micro- and nanoparticles

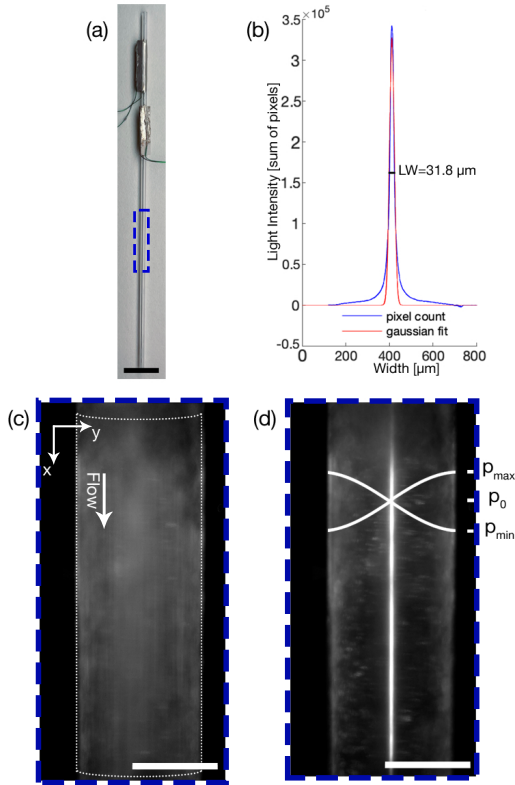


Fig. 3.2: (a) Glass capillary with two piezoelectric transducers and the ROI for all results generated using the glass capillary indicated by a blue dashed box. (b) Evaluation of the linewidth of the experiment shown in (d) using a self written MATLAB code, where a Gaussian fit is used to include $\sim 70\%$ of all particles. (c) $5 \mu\text{m}$ PS particles when the FCL is inactive at $t = 0 \text{ s}$. (d) Focused $5 \mu\text{m}$ PS particles at $f = 1.7204 \text{ MHz}$, $V = 20V_{pp}$ and a flow rate of $100 \mu\text{L min}^{-1}$ at $t = 1.12 \text{ s}$. Black (a) and white (c) and (d) scale bars: $5000 \mu\text{m}$ respectively $500 \mu\text{m}$.

3.5 Results

The data presented provides a brief overview of some of the use cases where the FCL can be employed to increase device performance and throughput, whilst being independent of a human operator. Fig. 3.3 and table 3.2 compare the relative performance between an excitation frequency determined empirically[140]

and the excitation frequency defined by the FCL. All experiments were conducted with 0.5% v/v.

Flow rate [$\mu\text{L min}^{-1}$]	LW for an empirical f [μm]	LW for FCL defined f [μm]
5 μm diameter PS particles		
100	59.54 (± 2.67)	31.80 (± 0.58)
300	149.02 (± 4.26)	48.51 (± 0.28)
500	273.17 (± 3.92)	80.27 (± 0.71)
700	373.19 (± 6.65)	114.27 (± 0.57)
900	439.65 (± 5.67)	162.55 (± 1.31)
1 μm diameter PS particles		
5	65.02 (± 3.92)	**
10	277.62 (± 18.20)	**
15	*	92.21 (± 0.72)
20	372.93 (± 10.42)	104.61 (± 0.26)
25	*	144.14 (± 0.63)
30	411.29 (± 9.94)	172.41 (± 0.89)
35	*	216.66 (± 1.91)
40	*	225.83 (± 1.14)
45	*	257.22 (± 2.22)
50	*	259.76 (± 1.88)
600 nm diameter PS particles		
5	*	77.23 (± 1.50)
10	*	127.42 (± 1.57)
15	*	170.37 (± 10.48)
20	*	242.52 (± 1.80)
25	*	275.95 (± 3.74)
30	*	264.81 (± 2.61)

Tab. 3.2: Comparison of the LW between the empirically defined excitation frequency and the frequency found by the FCL (FCL). This data corresponds to the data from Fig. 3.3. * no data available from previous experiments. ** data was excluded due to particle trapping.

Chapter 3. Optical feedback control loop for the precise and robust acoustic focusing of cells, micro- and nanoparticles

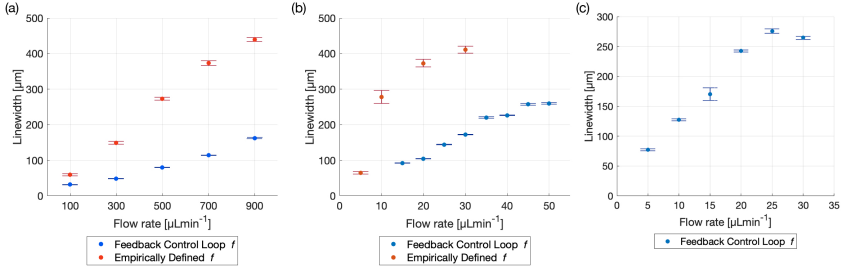


Fig. 3.3: Comparison of particle focusing in a glass capillary with a empirically defined excitation frequency[115] vs. an optimal excitation frequency found by the FCL for different particle sizes and flow rates. All results were generated with the same setup and capillary driving both piezoelectric transducers at $V = 20V_{pp}$ and the precise linewidth can be found in table 3.2. **(a)** Comparison of $5\mu\text{m}$ diameter PS particles for the flow rates: 100, 300, 500, 700 and 900 μLmin^{-1} . The excitation frequency defined by the FCL is $f = 1.7204$ MHz. The improved linewidth is not only seen in the smaller linewidths at higher flow rates, but also in the smaller error bars, indicating a more precise and robust focusing. **(b)** The focusing of 1 μm diameter PS particles using an empirically defined frequency was possible for the flow rate of $5\mu\text{Lmin}^{-1}$. At $10\mu\text{Lmin}^{-1}$ the linewidth was already close to half of the diameter of the capillary and at higher flow rates, the focusing was nearly non existent. Employing the FCL, which found the frequency at $f = 1.7204$ MHz, focusing was possible even with flows up to $50\mu\text{Lmin}^{-1}$. **(c)** 600 nm diameter PS particles could be focused by the FCL, when utilizing *phase 1* and *phase 2*. The frequency defined by the FCL from *phase 1* was 1.7202 MHz and *phase 2* further iterated and found an improved excitation frequency at 1.72075 MHz. Even at high flow rates, e.g. $25\mu\text{Lmin}^{-1}$ and $30\mu\text{Lmin}^{-1}$ the linewidth was still smaller than half of the capillary diameter.

3.5.1 Improved focusing of 5 micrometer diameter PS particles

There is significant demand for narrow LWs at high flow rates to increase the throughput while minimizing clogging and it was recently demonstrated that flow rates of up to $1000\mu\text{Lmin}^{-1}$ are relevant and achievable for cell separation.[233] Flow rates of up to $900\mu\text{Lmin}^{-1}$ were demonstrated, in[115] albeit the focusing drastically decreased at high flow rates, Fig. 3.3. The FCL presented here is capable of focusing the PS particles down to a narrower LW, with an increased stability, where the stability increase is defined as the reduced size of the error of the measurements, as illustrated in Fig. 3.3 and table 3.2. The FCL resulted in a LW which was half as narrow as the LW that resulted from determining the excitation frequency empirically for a flow rate of $100\mu\text{Lmin}^{-1}$ (94mm s^{-1}). For higher flow rates, the LW remained narrower by even larger margins and at a $900\mu\text{Lmin}^{-1}$ (850mm s^{-1}) flow rate the LW resulting from the FCL was about the same width as the LW for a flow rate of $300\mu\text{Lmin}^{-1}$ for the empirically determined frequency. The frequency chosen for this comparison is $f = 1.7204$

MHz, found using only *phase 1* of the FCL as in Fig. 3.1. Technically, *phase 2* could have been run as well, but as the LW was already half of the LW when using the empirically determined excitation frequency ($f = 1.74$ MHz), *phase 2* was omitted.

3.5.2 Higher flow rate for 1 micrometer diameter PS particles

Decreasing the particle size increases the difficulty to focus the particles as the ARF decreases and therefore more precise excitation frequencies are required. Focusing of $1\mu\text{m}$ diameter PS particles for instance is possible however, above $10\mu\text{L min}^{-1}$ Gerlt *et al.*[115] were not able to focus $1\mu\text{m}$ PS particles, as the excitation frequency determined empirically has a limited precision. The FCL demonstrates that $1\mu\text{m}$ particles can be focused beyond $10\mu\text{L min}^{-1}$. Even at 5 times the flow rate ($50\mu\text{L min}^{-1}$ instead of $10\mu\text{L min}^{-1}$) the particle LW was still narrower with the frequency chosen by the FCL, compared to the empirically chosen frequency in Fig. 3.3. The lack of focusing of the FCL of 5 and $10\mu\text{L min}^{-1}$ flow rates can be attributed to PS particles being trapped in the device whereas the trapping can only be overcome at higher flow rates. As for the $5\mu\text{m}$ PS particles, only *phase 1* was used to generate this data.

3.5.3 600 nanometer diameter PS particle focusing

Particle sizes greater than one micrometer in diameter are important, but with improving device designs and manufacturing precision, focusing of nanometer particles is a realistic aim. Building on the corpus of nanometer particle trapping[234] and separation,[235] the FCL demonstrated the capability to use bulk acoustic wave (BAW) devices to focus nanometer particles. When the particle radius is around the critical radius r_c the acoustic streaming and thus the Stokes' drag force resulting from the acoustic streaming can dominate the movement of the particles in the fluid, therefore *phase 1* and *phase 2* of the FCL were run in order to find an excitation frequency at which the dominating force was still the ARF. Eq. 3.7 indicates that the analytical and numerical critical radius where the AS dominates and no focusing is possible is $r_{c,a}^{1D} = 0.78\mu\text{m}$ respectively $r_{c,n} = 0.35\mu\text{m}$. The focusing of 600 nm diameter PS particles however show that both the analytical and the numerical solution both provide critical radii above which focusing was demonstrated in Fig. 3.3. While[115] was not able to find any focusing of 600 nm diameter particles, the FCL presented here could identify excitation frequencies at which the 600 nm diameter particles could be focused. Even at higher flow rates, such as $30\mu\text{L min}^{-1}$, the excitation frequency determined by the FCL proved to be good enough for focusing particles.

Chapter 3. Optical feedback control loop for the precise and robust acoustic focusing of cells, micro- and nanoparticles

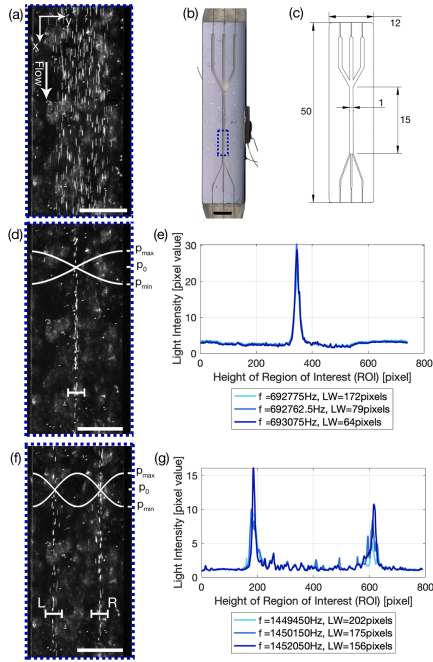


Fig. 3.4: Glass-silicon-glass device used for the manipulation of biological cells. (a) SaOs-2 cells when the FCL is inactive and a cell concentration of $0.361E5$ cells / ml. (b) Image of the device and the ROI indicated by the dashed blue box. The top and the bottom of the device have a beige coloring due to the Epoxy glue used to glue the capillary connections. A piezoelectric transducer is glued onto the side of the device at half of the height on the right hand side. (c) Sketch of the device with the dimensions given in mm. Device: 50 mm length, 12 mm width, 1.4 mm thickness; focusing channel: 15 mm length, 1 mm width, 0.2 mm height (d) SaOs-2 cells focusing in the center of the channel of the device with a linewidth of $31.28 \pm 0.98 \mu\text{m}$ at $f = 0.7101$ MHz and a flow rate of $10 \mu\text{L min}^{-1}$. The white cross-bar indicating the focusing is not to scale. (e) Plot of 3 frequencies and the corresponding linewidths for *phase 2*. (f) Cells focusing in two lines. The left-hand-side (L) linewidth is $33.01 \pm 5.27 \mu\text{m}$ and the right-hand-side (R) linewidth is $36.15 \pm 1.00 \mu\text{m}$ at $f = 1.453$ MHz and a flow rate of $10 \mu\text{L min}^{-1}$. (g) Plot of 3 frequencies and the corresponding linewidths for *phase 2*. (e) & (g) were re-plotted with altered colors and a reduced amount (three) of plotted frequencies. The voltage was $30 V_{pp}$. The lighting angle and the video settings, mainly a high exposure time set new at the beginning of each experiment, result in the bright cells. Black and white scale bar: $5000 \mu\text{m}$ respectively $500 \mu\text{m}$.

3.5.4 Glass - silicon - glass device and $n = 1, 2$ resonance mode

The glass capillary was used to demonstrate the focusing of PS particles using the FCL and to quantify the performance increase of the system. To further

elucidate how powerful the FCL is, a glass-silicon-glass device was used. The glass-silicon-glass device demonstrates that the FCL is capable of not only finding an improved excitation frequency for other setups than glass capillaries and PS particles, but can furthermore focus biological cells in an $n = 1$ resonance mode as detailed in Eq. 3.5. $n > 1$ resonance modes are however also important in many processes. By altering the frequency range, and only the frequency range, the FCL is able to define the optimal frequency for resonance modes $n > 1$, such as the $n = 2$ resonance mode shown in Fig. 3.1(f) and (g). This is made possible, as the FCL is searching for the narrowest LW, and only chooses to look at one line, thus enabling this feature of the FCL. Therefore it is not surprising that the LWs for the resonance modes $n = 1$ and $n = 2$ are approximately the same (Fig. 3.4(d) $31.28 \pm 0.98 \mu\text{m}$ compared to (f) (L) $33.01 \pm 5.27 \mu\text{m}$ and (R) $36.15 \pm 1.00 \mu\text{m}$, which also corresponds to the line width found for the $5 \mu\text{m}$ PS particles with a flow rate of $100 \mu\text{L min}^{-1}$ ($31.80 \pm 0.58 \mu\text{m}$). Another interesting readout to point out from Fig. 3.4(e) and (g) is that, by keeping the total cell number constant, the pixel value of the light intensity drops by half if the mode is increased from $n = 1$ (e) to $n = 2$ (g) which is as expected as there are half as many cells per modal line, and indicates that the FCL could be used to read out sample concentration. Another value to note is that in Fig. 3.1(c) the pixel value is 255, indicating a pure white line, which is expected as the video shows a stream of white in the middle. The cells, which are too few in number to form a continuous line in the channel even when focused, and therefore leave black spots in between the individual cells, have a much smaller average pixel value. Thus indicating that using higher concentrations is beneficial as this suppresses background noise, while at the same time allows for a higher sample concentrations and thus results in a higher sample throughput.

3.6 Conclusions

The FCL was compared against 3 experiments previously conducted in our lab[115] and demonstrates a superior performance compared to experienced scientists in 1) reducing the linewidth by at least a factor of two for $5 \mu\text{m}$ PS particles, 2) increasing the range of flow rates in which $1 \mu\text{m}$ diameter PS particles could be focused and 3) identifying an excitation frequency for which 600 nm diameter PS particles could be focused. Furthermore, the FCL is capable of manipulating biological cells and resonance modes of n greater than 1.

These results indicate that by replacing the human operator by an optical FCL, *ceteris paribus*, the performance of a device can be augmented by automating otherwise laborious tasks. This replacement increases the device reliability without increasing the production complexity, increases the throughput, overall yields

narrower focusing and focusing of 600 nm diameter PS particles can be achieved. A limitation, was that for small particles and low flow rates, such as 1 μm diameter PS particles at 5 μLmin^{-1} and 10 μLmin^{-1} , particles were trapped at the piezoelectric transducers. This could be prevented by adapting the code to search for an optimal excitation frequency and then placing a frequency offset on the found frequency as the ARF decreases with sub-optimal frequency selection. This idea could also be used to find an excitation frequency in which all particles are focused, and then placing a small offset in order to separate the particles by size. A further limitation was that particles below 600 nm diameter could not be focused. Provided an advanced imaging system with a higher resolution, we believe that even smaller particles could be focused. Research groups with devices already mounted on high resolution optical systems could for instance use the screen capture functionality function as an adapter for their optical system and test this hypothesis.

The FCL relies on an optical input to minimize the particle linewidth. The frequency thus chosen and continuously adapted by the FCL is therefore not necessarily the exact resonance frequency of the system, which sets the presented FCL apart from previously reported FCLs. As the FCL requires no additional equipment, provided that the setup has an optical readout and the function generator can be controlled by a computer, we thus present a cost-effective, high-throughput and automated method to rapidly increase the efficiency of established systems used for particle focusing. The source code for the FCL is openly accessible; ideas and augmentations from the community are welcomed.

4

Measuring and simulating the biophysical basis of the acoustic contrast factor of biological cells

This chapter is available on arxiv as a preprint.

Harshbarger, C., Pavlic, A., Bernardoni, D., Viol, A., Snedeker, J., Dual, J., Silván U. (2023).¹

4.1 Abstract

The acoustic contrast factor (ACF) is calculated from the relative density and compressibility differences between a fluid and an object in the fluid. To name but one application, knowing the ACF of a biological cell represents a crucial step in the design of acoustophoretic systems, for instance to isolate cancer cells from a liquid biopsy such as blood without labels or physical contact. For biological cells the static compressibility is different from the high frequency counterpart relevant for the ACF. In this study, we started by characterizing the ACF of low vs. high metastatic cell lines with known associated differences in phenotypic static E-modulus. The change in the static E-modulus, however, was not reflected in a change of the ACF, prompting a more in depth analysis of the influences on the ACF. We demonstrate that static E-modulus increased biological cells through formaldehyde fixation have an increased ACF. Furthermore, the static E-modulus decreased biological cells treated with actin polymerization inhibitor cytochalasin

¹This chapter is an extension of the work previously presented at Acoustofluidics 2022 [236].

D have a decreased ACF. Complementing these mechanical tests, a numerical COMSOL model was implemented and used to parametrically explore the effects of cell density, cell density ratios, dynamic compressibility and therefore the dynamic bulk modulus. Collectively the combined laboratory and numerical experiments reveal that a change in the static E-modulus alone might, but does not automatically lead to a change of the dynamic ACF for biological cells. This highlights the need for a multiparametric view of the biophysical basis of the cellular ACF, as well as the challenges in harnessing acoustophoretic systems to isolate circulating cells based on their mechanical properties alone.

4.2 Introduction

Carl Jung states "The greater the contrast, the greater the potential." [237]. This is true in the field of acoustofluidics (AF), the frequency dependent acoustic pressure wave driven manipulation of particles in a fluid. In the case of AF, the contrast is termed the acoustic contrast factor (ACF) Φ , and arises from relative density and compressibility differences between a fluid and an object in the fluid as described by Yosioka and Kawasima [194]. The greater the ACF, the greater the acoustic potential and the more the object in the fluid will interact with the pressure wave. Changes to either the object or the fluid will lead to a change of potential, whereas the acoustic potential in an AF system is termed the Gor'kov potential [192]. Exploiting the acoustic contrast between biological cells and a fluid has been successfully demonstrated multiple times for the manipulation of cancer cells in suspension [131, 132, 72, 133, 134]. Therefore, AF is a promising diagnostic tool when considering the spreading of cancer cells through bodily fluids, a process known as metastasis which is responsible for 90% of cancer related deaths [238]. In order for cancer cells to enter the metastatic state, they undergo a wide range of changes, including a decrease in their static E-modulus [173], which leads to a different mechanical phenotype between the cancer cells located within the primary tumor and the disseminated cancer cells. This decrease in the static E-modulus can be measured by gold standard measurement techniques such as magnetic tweezers [152], AFM [153] and micropipette aspiration [154]. Although the presented methods are powerful and established, there are certain limitations such as that the biological cells are adherent on tissue culture plastic, that only one mechanical parameter of the cell of interest is measured and that the measurement is based off of one small region of the biological cell. An alternative method to measure the static E-modulus, which relies on the deformation of the entire biological cell and does not rely on adherent cells, is real-time deformability cytometry (RT-DC) [155]. Although these methods have led to a vast catalog of static E-moduli for various cancer cell types in adherent and non-adherent states, the reported material properties stem

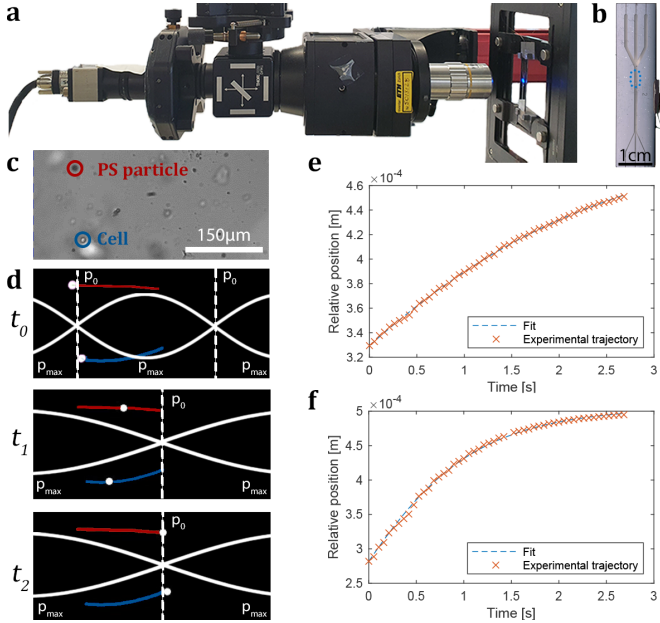


Fig. 4.1: (a) Image of the vertical setup showing the camera (far left) and the AF device being imaged (far right). (b) AF device imaged with the ROI indicated by the blue dashed box. A piezoelectric transducer glued to the side or bottom of the device establishes an acoustic field within the device. (c) Frame of a video of a cell and PS particle in suspension within the AF device. Wherever possible, the cells were prealigned in a λ mode. (d) The analysis of the particle motion is performed in multiple steps: The video recording of every experiment is split into single images and converted to black and white. The object trajectories are indicated in the same colors as the PS particle and cell in c and are generated using the Fiji Plugin TrackMate. At t_0 and $1.42 \text{ MHz} \pm 2 \text{ kHz}$ the cells and PS particle are located in pressure nodes of the λ mode where $p_0 = 0$, as both objects have a positive acoustic contrast factor. The frequency is changed to $742.1 \text{ kHz} \pm 2 \text{ kHz}$, which alters the location of the zero pressure nodes. This causes the PS particles and biological cells to migrate during t_1 away from their previous position to the middle of the channel. At t_2 the objects are again at the zero pressure nodes $p_0 = 0$ of the $\lambda/2$ mode, thus having minimized their acoustic potential. (e, f) The plots show the position of a biological cell (e) and PS (f) particle during the migration from a high pressure to a low pressure region of the $\lambda/2$ mode. The fit is with respect to the pressure within the system using Eq. 4.22. Using a self written Matlab script, the ACF of the biological cells can be back-calculated.

from (quasi-)static measurements. Considering emerging ultrasound frequency technologies to detect and treat cancer, such as oncotripsy [156, 157], the question needs to be answered if static material parameters are sufficient or if lookup

tables for material properties need to be extended with values stemming from dynamic measurements. Such dynamic material properties can be measured with AF, by focusing cells using ultrasound frequencies, as illustrated in Fig. 4.1. By focusing the biological cells in a suspension with polystyrene (PS) particles with a known ACF, the ACF of the biological cells can be calculated. This method of measuring the ACF is contactless, label-free and does not decrease cell viability [239].

There is a growing body of literature where the ACF of biological cells is measured [177, 180, 178, 179] as summarized in table 4.1 and new ACF values reported in Fig. 4.2. The work prior to this study however mostly results in measurements of the compressibility of biological cells from which the ACF can be calculated, whereas the density is assumed [177], measured with methods such as a neutrally buoyant sample [178] or measured by defocusing of the particles during sedimentation [179]. Further publications resulted in lookup tables for cell lines with different metastatic potentials [180] and ACF comparisons between fixed and non-treated biological cells [178].

Beside these few studies, little is known about the correlation between the known static E-modulus of biological cells and the dynamic ACF. To help broaden the understanding of the applicability of known material parameters to ultrasound frequency applications we increased the static E-modulus [240] of the bone cancer cell Sarcoma Osteogenic (SaOs)-2 using the protein crosslinking fixative formaldehyde [241] and decreased static E-modulus [242] using the actin polymerization inhibitor cytochalasin D [243] (CD). After these treatments the ACF of the biological cells are measured in a Phosphate Buffer Solution (PBS). Furthermore, the SaOs-2 parental cell line is paired with its highly metastatic counterpart Lung Metastasis (LM)5, with the known static E-modulus measured of 0.95 kPa and 0.8 kPa, respectively [153] when measured with RT-DC. Thus demonstrating the limitations of trying to predict the ACF when only taking a change in static E-modulus into account. To further place the experimental results into context, a numerical model, seen in Fig. 4.3 is introduced. The parameter space investigated with the model includes the density, compressibility and static E-modulus, as seen in Fig. 4.4. Thus aiming at closing gaps of unknown dynamic material properties of cells which would be useful for cancer diagnosis and treatment.

4.3 Results

We used a vertical setup composed of a widefield microscope to image the PS particles and cell migrate through the fluid, as seen in Fig. 4.1. The AF device

was placed in a vertical orientation to potentially eliminate rolling along the glass surface and the 3 inlet configuration can improve the prefocusing efficiency, if needed. The standing pressure wave was established by a piezoelectric transducer powered by a sinusoidal signal of a function generator increased in magnitude by an amplifier. The frequencies used are in the $742.1 \text{ kHz} \pm 2 \text{ kHz}$ range and were varied for optimal focusing. A summary of the ACFs of previous publications is, together with the results of this study, summarized in table 4.1. The ACF measured in PBS of the low metastatic potential cell line SaOs-2 is taken as the baseline and is 0.037 ($n = 25$). SaOs-2 formaldehyde fixed cells have an ACF of 0.050 ($n = 10$). SaOs-2 cells treated with cytochalasin D have an ACF of 0.022 ($n = 12$). The higher metastatic potential cell line LM5 have an ACF of 0.037 ($n = 12$). The average cell diameter for each condition was measured and is reported in table 4.1.

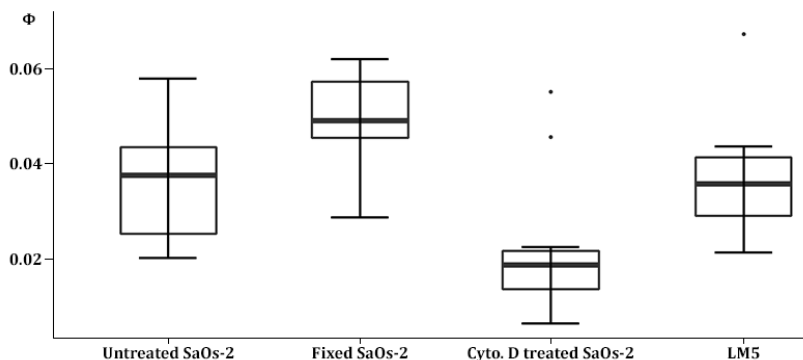


Fig. 4.2: The ACF measured in PBS of the low metastatic potential cell line SaOs-2 is taken as the baseline and is 0.037 ($n = 25$). SaOs-2 formaldehyde fixed cells have an ACF of 0.050 ($n = 10$). SaOs-2 cells treated with cytochalasin D have an ACF of 0.022 ($n = 12$). The higher metastatic potential cell line LM5 have an ACF of 0.037 ($n = 12$).

The base numerical model of a SaOs-2 cell is constructed as described in the Methods, and is composed of a cytoplasm-nucleoplasm-nucleolus structure as shown in Fig. 4.3. The cell and all the layers are assumed to be spherical. The radius for the SaOs-2 cell is taken from the measurements reported in table 4.1 ($8.80 \mu\text{m}$). The outer radius of the nucleoplasm ($6.66 \mu\text{m}$) is computed from previously reported [153] nucleus-cell volume ratio of 0.434, while the radius of the nucleolus ($2.14 \mu\text{m}$) follows from the nucleolus-nucleus volume ratio of 1/30 reported by Guttman and Halpern [244]. The mass density in each layer

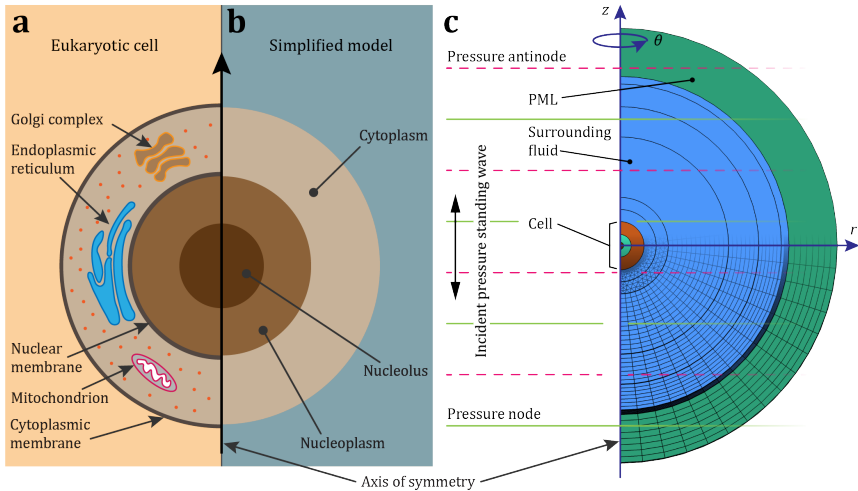


Fig. 4.3: Numerical model of a eukaryotic cell. The ACF and its dependencies are extracted from the numerical model. (a) The structure of a typical eukaryotic cell. (b) Simplification of the representation of the cell into three layers, namely, cytoplasm, nucleoplasm, and nucleolus. (c) Geometry of an axisymmetric finite-element method model of a eukaryotic cell, surrounded by fluid and perfectly-matched layer (PML).

is computed according to the mass density ratios of the three characteristic cellular layers, as reported by Kim and Guck [245], while imposing an assumed apparent density of the whole cell of 1060 kg m^{-3} . The static E-modulus of each cellular layer is assigned based on the ratios used in the literature [156], such that the apparent static E-modulus computed through the rule of mixture results in $E = 1 \text{ kPa}$, as reported from RT-DC measurements [153]. The initial bulk modulus of individual cellular layer is assigned based on the reported 2% lower speed of sound in nucleus compared to the cytoplasm [246].

In the first step shown in Fig. 4.4(a), the SaOs-2 model, with the density and static E-Modulus taken from literature, is calibrated by varying the bulk modulus K of all the layers through a common multiplier to match the experimentally measured ACF of 0.037. The bulk modulus of the calibrated SaOs-2 model therefore follows as 2.49 GPa for the cytoplasm and 2.24 GPa for the nucleus (nucleoplasm and nucleolus combined). Figure 4.4(b) shows how the bulk modulus in the range of interest connects to the Poisson ratio for the relatively low static

E-modulus of 1 kPa, reported for SaOs-2 cells [153].

The base numerical model of a LM5 cell is then formed by keeping all the material properties of individual cell layers from the calibrated SaOs-2 cell model, but changing the volume of the cell to the volume measured in experiments. In addition, the nucleus-cell volume ratio was changed from 0.434 to 0.569, according to previously reported [153] values. These changes lead to a decrease in the ACF for the base LM5 cell to 0.031 whereas the value measured in experiments is $\sim 27\%$ higher at 0.037. The decrease in the ACF is due to the increased nucleus-cell volume ratio that decreases the apparent density and the apparent bulk modulus of the cell. In Fig. 4.4(c) we explore how a change in the density and bulk modulus across the three layers of a cell through common multipliers could cause the increase in the ACF that would match the experimentally measured ACF of 0.037 (red line). In Fig. 4.4(d), we demonstrate that changing the E-modulus across the cell layers does not directly affect the ACF as long as the bulk modulus and the density are kept at a fixed value.

4.4 Discussion

Our results reveal that formaldehyde-fixed cells, presumed to have an increased static E-modulus, have an increased ACF compared to untreated cells. Furthermore biological cells treated with the actin depolymerizing drug cytochalasin D, known to reduce the static E-modulus, have a decreased ACF. This simultaneous change of static E-modulus and ACF is particularly interesting when considering that a decrease in the static E-modulus correlates to an increase of the metastatic potential of cancer cells [172], especially as the static E-modulus of an object can be linked to its compressibility (Eq. 4.15 and 4.16) and thus to the ACF of the object, as demonstrated by Eq. 4.19. This dependence could potentially be used to predict the increased ACF of the static E-modulus increased biological cells and the decreased ACF of static E-modulus decreased biological cells as presented in this study. To test this predictability a hypothesis can be formulated, that the more malignant cells have a decreased ACF and thus interact less with the acoustic field. This hypothesis can be tested with the parental cancer cell line with low metastatic potential SaOs-2 with a static E-modulus of 0.95 kPa and the high metastatic potential cell line LM5 with a static E-modulus of 0.8 kPa, both static E-moduli were measured with a RT-DC system [153]. Contrary to the hypothesis, we found that the difference between the ACFs of the two cell lines with different metastatic potential is only in the range of a few percent, even though the sample size is limited. Nevertheless, this opens up the question if the static E-modulus change is the causation for a change of the ACF or if the change is merely correlated. The broader implication is that forming a hypothesis

Chapter 4. Measuring and simulating the biophysical basis of the acoustic contrast factor of biological cells

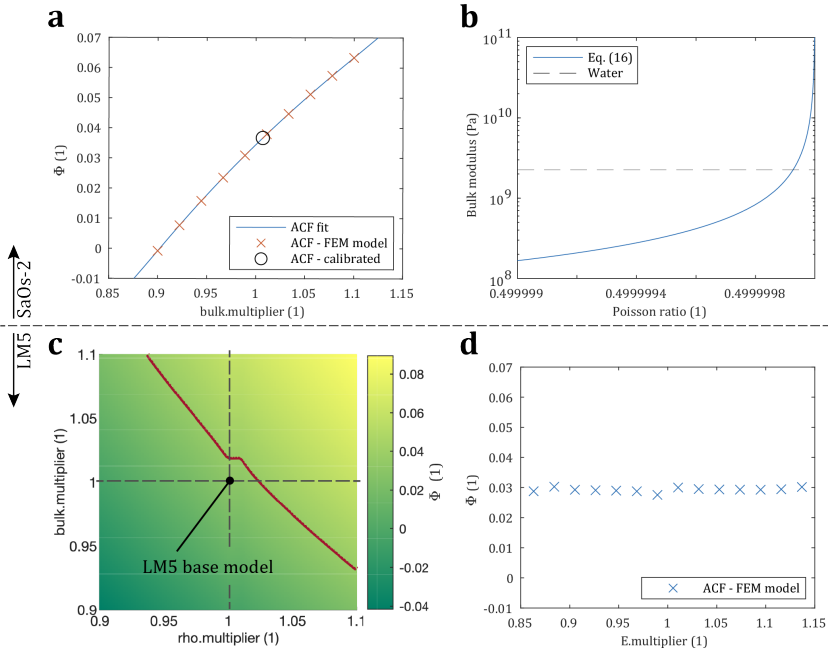


Fig. 4.4: (a) The ACF of a SaOs-2 cell depending on the bulk modulus multiplier (bulk.multiplier) common to the three layers of the SaOs-2 model with a constant static E-modulus. To calibrate the model, the bulk multiplier is tuned to the value that yields the ACF of 0.037 measured experimentally. (b) The Poisson's ratio corresponding to the range of bulk modulus relevant for our study, computed from Eq. 4.16 with a constant static E-modulus; the bulk modulus of water is shown for reference. (c) The calibrated layer-based material properties from the SaOs-2 model were used as a basis for the LM5 model, changing only the volume of the cell and the nucleus-cell volume ratio according to experimental observations [153]. The base LM5 model underestimates the ACF at 0.0309, compared to the experimentally measured value of 0.037. The common bulk modulus multiplier and density multiplier are varied in (c) to indicate the combination changes in the density and bulk modulus that provide the experimentally measured ACF (denoted with the red line). (d) Varying the E-modulus, while keeping the bulk modulus and the density constant, does not influence the ACF.

about dynamic material properties based on known static material properties can lead to imprecise answers and the current literature reflects this uncertainty and caution must be exercised when making these assumptions.

Cushing *et al.* [178] found that fixing the biological cells with formaldehyde leads to an increase of the compressibility together with a decrease of the density. This leads to an overall decrease of the ACF, which is contrary to the increase of the ACF found in our study. Important to note is that in Cushing *et al.* the measurement of the compressibility was done by speed of sound measurements on a population of biological cells in suspension and not on individual biological cells as was used during this study, which could account for some discrepancies. Furthermore, although the static E-modulus of the cell should have been increased by the fixation, the authors do not try to link the static E-modulus and the dynamically measured compressibility.

Wang *et al.* [180] demonstrated another method to measure the density and compressibility of biological cells. Although no statistical analysis was performed, they demonstrated that the compressibility increases with the metastatic potential. The change in the density however did not follow a trend when compared to their metastatic potential. The authors do not specify in which fluid the measurement was performed, therefore it is not possible to precisely calculate the ACF. Assuming PBS as the fluid in which the experiments were conducted, we calculate the ACF of the low and high metastatic cell lines. For these assumed values of the ACF, we could not find a correlation between the metastatic potential and the ACF, in part stemming from the simultaneous change of the compressibility and density.

Summa summarum, there are many gaps in the literature when considering the dynamic properties of biological cells in acoustic fields. Slightly different methods lead to different trends concerning the ACF, and no correlation is attempted to be made between known static material properties and the dynamically measurement data. This is unfortunate as most literature on cell mechanics reports the static E-modulus, which is the standard output for gold standard methods such as the quasi-static AFM.

One major limiting factor to date hindering the direct comparison is that most publications deal with measuring only one material property such as the static E-modulus or the dynamic compressibility. This one parametric view is not sufficient for even the simplest cell mechanics models such as the elasticity theory which requires at least two parameters to describe cell mechanics [248], as seen in Eq. 4.16. This can then necessitate estimates of further material properties such

as the Poisson's ratio ν , and whichever ratio is chosen has orders of magnitude impact on the calculated static bulk or E-modulus. This can quickly be seen from the common assumption that cells are incompressible, meaning that $\nu = 0.5$ and would therefore imply an infinitely large bulk modulus as seen from Eq. 4.16 and Fig. 4.4(b). In order to try to shed some light on the usefulness of static mechanical properties reported for various cell lines, we provide a computational model for a cell in an acoustic field. This model is insofar interesting as it is a multiparametric model where the mechanical properties, such as the E-modulus and the bulk modulus, can be varied independently. The computational model shows on the one hand that the E-modulus can be varied without changing the ACF as seen in Fig. 4.4(c). This supports previous findings and the results from our experiments, that a change in E-modulus might be correlated with a change in the ACF but does not necessarily need to be the causation. Therefore the hypothesis that the static E-modulus alone can be used to predict the dynamic material properties must be rejected. To further demonstrate this possible independence, the computational model shows that there is a parameter space where a variation of the apparent bulk modulus and density can result in the same ACF as seen in Fig. 4.4(b). This finding is further supported by the findings of Wang *et al.* where a change in metastatic potential altered both the density and dynamic compressibility, thus defying a trend between metastatic potential and the ACF. There is another method to measure dynamic properties of a cell (e.g. bulk modulus) - scanning acoustic microscopy [248], which confirms our predictions of the Poisson's ratio, and confirms that the E-modulus can vary independently of the bulk modulus. This means that most known material properties have an undefined influence on dynamic measurements and prior knowledge cannot be exploited, such as static E-modulus measurements from quasi-static methods such as AFM or RT-DC. This is problematic for applications such as the acoustic focusing and sorting of cells in liquid biopsies, potential cancer treatment methods such as oncotripsy, ultrasound neuromodulation [158, 159] and sonogenetics [160]. This indicates an unmet need for dynamic material properties which in parts could be potentially alleviated by AF.

4.5 Methods

4.5.1 Theoretical background: Acoustic scattering and streaming

The presented work deals with objects in fluids. In order to predict the motion of the objects, the fundamental equations of the motion of the fluids need to be introduced. The motion of a viscous fluid is governed by the compressible

Navier-Stokes equations

$$\rho \left[\frac{\partial \mathbf{v}}{\partial t} + (\mathbf{v} \cdot \nabla) \mathbf{v} \right] = -\nabla p + \eta \nabla^2 \mathbf{v} + \left(\eta_B + \frac{\eta}{3} \right) \nabla (\nabla \cdot \mathbf{v}), \quad (4.1)$$

and the continuity equation

$$\frac{\partial \rho}{\partial t} = -\rho \nabla \cdot \mathbf{v}, \quad (4.2)$$

with the velocity \mathbf{v} , pressure p , the dynamic viscosity η and the bulk viscosity η_B . As the fluid is assumed to be barotropic, the density ρ is assumed to be a function of pressure p only $\rho = \rho(p)$.

The equations are linearized using the perturbation approach [188]. Accordingly, the physical fields are expanded in a series, $\square = \square_0 + \square_1 + \square_2 + \dots$, where \square represents the field, while the subscript denotes the respective order.

First-order (acoustic) problem

For a quiescent fluid at the zeroth order ($\mathbf{v}_0 = \mathbf{0}$), the substitution of the perturbed fields into the governing equations yields the following set of linear first-order equations,

$$\rho_0 \frac{\partial \mathbf{v}_1}{\partial t} = -\nabla p_1 + \eta \nabla^2 \mathbf{v}_1 + \left(\eta_B + \frac{\eta}{3} \right) \nabla (\nabla \cdot \mathbf{v}_1), \quad (4.3)$$

$$\frac{\partial \rho_1}{\partial t} = -\rho_0 \nabla \cdot \mathbf{v}_1, \quad (4.4)$$

with the equilibrium density ρ_0 . The equation of state,

$$\rho_1 = \frac{1}{c_0^2} p_1, \quad (4.5)$$

is connecting the first-order density with the first-order pressure through the speed of sound in the fluid c_0 . The first-order fields are assumed to have a harmonic time-dependency with the factor $e^{i\omega t}$, with the angular frequency $\omega = 2\pi f$.

The acoustic fields, comprised of the velocity \mathbf{v}_1 and pressure p_1 , are assumed to be the sums of background fields (bg) and scattered fields (sc), namely $(\)_1 = (\)_{1\text{bg}} + (\)_{1\text{sc}}$. We assume a one-dimensional plane standing wave along the z -direction of the cylindrical coordinate system. The background velocity field is set to

$$\mathbf{v}_{1\text{bg}} = \text{Re} \left[\frac{\varphi_a}{2} i k \left(e^{ikz} - e^{-ikz} \right) e^{i\omega t} \right] \mathbf{e}_z, \quad (4.6)$$

with the corresponding velocity potential amplitude

$$\varphi_a = -\frac{p_a}{i\omega\rho_0 + \left(\eta_B + \frac{4}{3}\eta\right)k^2}, \quad (4.7)$$

with pressure amplitude p_a , and the wavenumber

$$k = \frac{\omega}{c_0} - \alpha i, \quad (4.8)$$

with the attenuation coefficient for viscous fluids [249]

$$\alpha = \frac{\omega^2}{2c_0^3\rho_0} \left(\eta_B + \frac{4}{3}\eta \right). \quad (4.9)$$

Second-order (streaming) problem

Applying the perturbation theory up to second order to the governing equations, together with taking the time average $\langle \square \rangle = \frac{1}{T} \int_T \square dt$ over an oscillation period $T = 1/f$, results in the equations of acoustic streaming [199],

$$\nabla \langle p_2 \rangle - \eta \nabla^2 \langle \mathbf{v}_2 \rangle - \left(\eta_B + \frac{\eta}{3} \right) \nabla (\nabla \cdot \langle \mathbf{v}_2 \rangle) = -\rho_0 \nabla \cdot \langle \mathbf{v}_1 \mathbf{v}_1 \rangle, \quad (4.10)$$

$$\rho_0 \nabla \cdot \langle \mathbf{v}_2 \rangle = -\nabla \cdot \langle \rho_1 \mathbf{v}_1 \rangle. \quad (4.11)$$

4.5.2 Theoretical background: Acoustic contrast factor

A method to measure the acoustic contrast factor of a biological cell is to subject the biological cell to a standing pressure wave within a fluid cavity. The standing pressure wave is generated by exciting a piezoelectric transducer (PT) glued onto an acoustofluidic device, which transmits the vibration of the PT into the fluid cavity where resonance is established. These vibrations, when assuming a spherical particle with a radius much smaller than the acoustic wavelength in an inviscid fluid, give rise to a potential commonly defined as the Gor'kov potential U [192]

$$U = \frac{4\pi}{3} r^3 \left[f_1(\tilde{\kappa}) \frac{1}{2\rho_0 c_0^2} \langle p_{1\text{bg}}^2 \rangle - f_2(\tilde{\rho}) \frac{3}{4} \rho_0 \langle \mathbf{v}_{1\text{bg}}^2 \rangle \right], \quad (4.12)$$

where r is the radius of the particle, $\langle p_{1\text{bg}}^2 \rangle$ the first order time averaged square of the incident acoustic pressure and $\langle \mathbf{v}_{1\text{bg}}^2 \rangle$ the first order time averaged square of the incident acoustic velocity. Furthermore, the monopole scattering coefficient $f_1(\tilde{\kappa})$ which is related to the relative compressibility between the particle and

the medium and the dipole scattering coefficient $f_2(\tilde{\rho})$ which is related to the relative density between the particle and the medium

$$f_1(\tilde{\kappa}) = 1 - \tilde{\kappa}; \quad \tilde{\kappa} = \frac{\kappa_p}{\kappa_0}, \quad (4.13)$$

$$f_2(\tilde{\rho}) = 2\frac{\tilde{\rho} - 1}{2\tilde{\rho} + 1}; \quad \tilde{\rho} = \frac{\rho_p}{\rho_0}, \quad (4.14)$$

where κ_p is the compressibility of a particle, κ_0 is the compressibility of the fluid and ρ_p is the density of the particle. The compressibility is in this case defined as the the inverse of the bulk modulus K

$$\kappa = \frac{1}{K}. \quad (4.15)$$

The bulk modulus is one parameter needed for the linear elastic description of cell mechanics and is given by

$$K = \frac{E}{3(1 - 2\nu)} \quad (4.16)$$

for a given static E-modulus and Poisson's ratio ν . For fluids, bulk modulus follows as $\rho_0 c_0^2$, and the compressibility as $\kappa_0 = 1/(\rho_0 c_0^2)$. The acoustic radiation force \mathbf{F}_{ARF} is commonly approximated as the negative gradient of the Gor'kov potential U

$$\mathbf{F}_{ARF} = -\nabla U. \quad (4.17)$$

Given an inviscid standing pressure wave defined through Eq. 4.6 and assuming $\eta = \eta_B = 0$, \mathbf{F}_{ARF} can be simplified to a one-dimensional ARF in the z direction

$$F_{\text{rad}}^{1D} = 4\pi r^3 E_{ac} k_z \sin\left(2k_z\left(z + \frac{w}{2}\right)\right) \Phi(\tilde{\kappa}, \tilde{\rho}). \quad (4.18)$$

$k_z = \frac{\omega}{c_0}$ is the wavenumber in an inviscid fluid, w is the width of the channel, $\sin(2k_z(z + w/2)) = 1$ for the maximal force, E_{ac} is the acoustic energy density, the direction of z is shown in Fig. 4.3 and Φ is the acoustic contrast factor

$$\Phi(\tilde{\kappa}, \tilde{\rho}) = \frac{1}{3} f_1(\tilde{\kappa}) + \frac{1}{2} f_2(\tilde{\rho}). \quad (4.19)$$

which is a dynamic quantity related to the scattering of pressure waves on objects and is related to the relative density and compressibility between a fluid and an object in the fluid. A table of relevant Φ values is given in table 4.1, whereas objects with a positive ACF migrate to pressure nodes as seen in Fig. 4.1 and objects with a negative ACF migrate to pressure anti-nodes. The drag force acting on a particle moving through a fluid is given by the Stokes' drag [195, 196]

Chapter 4. Measuring and simulating the biophysical basis of the acoustic contrast factor of biological cells

$$\mathbf{F}_{str} = -6\pi\eta r \mathbf{v}_p, \quad (4.20)$$

where \mathbf{v}_p is the velocity of the particle. Neglecting the particle inertia, the particle velocity v_z in the z direction can be calculated by balancing the ARF with the Stokes' drag [197]

$$v_z = \frac{2\Phi}{3\eta} r^2 k_z E_{ac} \sin\left(2k_z\left(z + \frac{w}{2}\right)\right). \quad (4.21)$$

With $v_z = \frac{\partial z_p}{\partial t}$ and given a particle at starting position z_0 at time $t = 0$, the transverse path $z_p(z_0, t)$ can be calculated [197]

$$z_p(z_0, t) = \frac{1}{k_z} \arctan\left\{\tan\left[k_z\left(z_0 + \frac{w}{2}\right)\right] \exp\left(\frac{4\Phi}{3\eta}(k_z r)^2 E_{ac} t\right)\right\} - \frac{w}{2}. \quad (4.22)$$

The resonance frequency for the n -th ultrasonic resonance mode of a one-dimensional standing wave with hard wall boundary conditions is [191]

$$f_{res}^{1D} = \frac{c_0 n}{2w} = \frac{c_0}{\lambda_n}, \quad (4.23)$$

where w is the width of the channel and λ_n is the wavelength. For $n = 1$ or $n = 2$, the wavelength is equal to $2w$ or w corresponding to the $\lambda/2$ mode or λ mode, respectively.

4.5.3 Setup

The setup is analogous to the one used in Harshbarger *et al.* [207] and is comprised of a function generator (AFG-2225, GW Instek) which is connected to a computer running a code which allowed for the one click change of the frequency. The signal from the function generator is amplified (325LA Linear Power Amplifier, Electronics & Innovation) and monitored using an oscilloscope (UTD2025CL, UNI-T). The amplified signal is passed on to the piezoelectric transducer (PT). The vertical setup seen in Fig. 4.1(a) is built from parts from the THORLABS Cerna® series. The video feed was generated with a 10x objective (M Plan Apo 10x / 0.28, Mitutoyu) and a uEye camera (UI-3160CP Rev. 2.1, iDS, 1920 x 1200 pixels, 60 fps). To positively identify the fluorescent PS in the solution, a blue LED was used. In addition, there was a backlight, shining through the backside of the device, which resulted in brightfield image, but also an increased fluorescent signal of the PS particles. The sample flow was controlled manually whereas the 1 ml syringe was placed vertically in a holder located above the device in order to avoid sedimentation of the PS particles and the cells in the tubing and the device. This vertical orientation is unlike the horizontal orientation presented in

[177, 180, 178, 179]. This vertical orientation is only advisable if the density of the objects in the fluid are in a similar range as the density of the fluid, as is the case for biological cells and PS particles in PBS.

4.5.4 Glass-silicon-glass device

The glass-silicon-glass device, seen in Fig. 4.1(b), is produced by bonding a 500 μm thick glass wafer to a 200 μm thick silicon wafer. The fluidic channel is patterned onto the exposed silicon wafer using photolithography (resist: S1828, Shipley, 4'000 rpm; developer: AZ351B, Microchemicals). The full thickness of the silicon wafer is etched away with an inductively coupled plasma (ICP) deep reactive ion etching (DRIE) machine (Estrellas, Oxford instruments). Following the etching, a 700 μm thick glass wafer is anodically bonded onto the exposed silicon wafer. The wafer is diced into individual devices with a wafer saw (DAD3221, Disco corporation). Fused silica capillaries ($164 \pm 6 \mu\text{m}$ outer diameter, $100 \pm 6 \mu\text{m}$ inner diameter, Molex) are inserted into the inlets and outlets of the device to create a fluidic connection. The capillaries are fixed with a two-component glue (5 Minute Epoxy, Devcon). Piezoelectric transducers (10 mm length, 2 mm width, 1 mm thickness, Pz26, Meggitt Ferroperm) are glued on using an electrically conductive Epoxy glue (H20E, Epoxy Technology). Copper cables (0.15 mm diameter) are attached to the piezoelectric transducers and the electrical connection was established with an electrically conductive silver paste. The final dimensions of the devices is given by: device: 50 mm length, 12 mm width, 1.4 mm thickness; focusing channel: 15 mm length, 1 mm width, 0.2 mm height as seen in Fig. 4.1c. The 3 inlets results in the cells already being slightly prefocused close to the walls before the acoustics is turned on. This makes the prefocusing process in a λ mode efficient, if even needed.

4.5.5 Polystyrene particles

Green fluorescent polystyrene (PS) particles (microParticles GmbH, Germany) with diameters of $10.23 \pm 0.13 \mu\text{m}$ and 2.5 w/v% were used for all experiments.

4.5.6 Cell culture

Two cell lines were used, the low metastatic potential parental cell line SaOs-2 [171] and the highly metastatic cell line LM5. Human SaOS-2 (ATCC, HTB85) cells stem from the American Type Culture Collection (ATCC; Manassas, USA). The LM5 cell line was kindly provided by E. S. Kleinerman (M.D. Anderson Cancer Center, Houston, TX). The LM5 cell line was established in 1999 [250]. In brief, in 1973 Sarcoma Osteogenic (SaOs)-2 cells were isolated from the primary

osteosarcoma of an 11 year old Caucasian girl. The SaOs-2 cells were injected into the tail vein of a nude mouse. After 6 months the mouse was sacrificed and the metastatic lesion was removed from the lung of the mouse. The cells isolated from the lung lesion are again injected into the tail of a new nude mouse. This process is repeated 4 times resulting in the lung metastasis 5 (LM5) cell line. The anatomical origin of the primary tumor from which the SaOs-2 cells were extracted in 1973 is not known. All cell lines are kept at the standard 37°C and 5% CO₂ and 95% air. The cell media used is DMEM - F12 Ham (D8437, Sigma) supplemented with 10% fetal bovine serum (10270106, Thermo) and 1% P/S. The cells were passaged when 60% confluency was reached. The diameter of the cells was measured by the CellDrop BF, DeNovix after removal from the cell culture flask or directly in the video. The results section always indicated how the cell size was measured.

4.5.7 Trajectory measurement protocol

The cells were removed from a T75 culture flask using Trypsin and centrifuged for 5 min at 300 g. After spinning down the cells, the excess culture medium was removed. If needed, the cells were treated by either:

- fixing the biological cells with 1 mL of a 4% formaldehyde solution (ROTI Histofix, CARL ROTH) for 30 minutes at room temperature, whereas formaldehyde functions as a protein crosslinker. Afterwards, the cells were washed twice with PBS to remove the fixative. Or
- with 300 μ L cytochalasin D, which is an inhibitor of actin filament polymerization, whereas the actin filaments play a fundamental role in controlling cell shape and mechanical properties [242]. A cytochalasin D (Sigma-Aldrich) stock solution of 5 mg mL⁻¹ was diluted down to 333 nmol mL⁻¹. The cells were incubated for 30 minutes at room temperature

4.5.8 Image analysis

The generated videos were analysed using Fiji [251]. The videos were converted to an Image Sequence. This allows for the selection of the Image Sequence starting from the first movement of the PS particles and cells in solution until the last frame where movement could be seen. The particles are identified and separated into either PS or cells by using one of two methods: The machine learning software ilastik [252] can be used. This allows for the automatic detection and classification of particles of interest, but requires a training set. For videos with low particle numbers, it is faster to track the particles by hand by going through the Image Sequence frame by frame and marking the particle of interest. The particle tracks are calculated using the Fiji Plugin TrackMate.

4.5.9 Data analysis

The biological cell and PS particle trajectories from TrackMate are imported into a custom MATLAB script. Importing the known material parameters, seen in table 4.1, of the PS particles and PBS and using the trajectory Eq. 4.22, the acoustic energy density E_{ac} within the system can be calculated. Using the extracted E_{ac} , the ACF of the biological cells in the fluid suspension can be calculated. A brief discussion about the normality and robustness of the data can be found in the Sup. Mat. B.1, where the data showed to be normally distributed and not dependent on the observer.

4.5.10 Numerical model

In the scope of our study, we developed a finite element method (FEM) model of an eukaryotic mammalian cell whereas the structure is based on the model of Heyden and Ortiz [156], consisting of nucleolus, nucleoplasm, and cytoplasm, which are modeled as elastic solids. A graphical summary of the simplified model of the cell is given in Figure 4.3.

The FEM model is built in COMSOL Multiphysics® v. 5.6 [253], following and building upon the general approach of Baasch *et al.* [254]. The perturbed equations 4.3, 4.4 and 4.5 of acoustic scattering and equations 4.10 and 4.11 of acoustic streaming are solved consecutively. The scattering is solved in a frequency domain study, while the streaming is computed in a stationary study, using the results of the scattering study as source terms in equations 4.10 and 4.11. The solid domains are modeled via the Solid Mechanics interface, where the appropriate material models are defined. The fluids in the frequency domain study are modeled with a Thermoviscous Acoustics interface with the adiabatic formulation, and afterwards, in the stationary study, with a Creeping Flow interface.

At the first order, we impose the continuity of velocity and stress at the fluid-solid interface. The fluid is modelled as unbounded, and far away from the particle the first-order fields converge to the background fields, defined by Eq. 4.6. At the second order, the no-slip boundary condition is imposed on the Lagrangian velocity of a fluid at the fluid-solid interface, in order to compensate for the oscillations of the interface at the first order. The Lagrangian velocity is defined as the summation of the Eulerian streaming velocity $\langle \mathbf{v}_2 \rangle$ and the Stokes drift [255, 256]

$$\mathbf{v}_{SD} = \left\langle \left(\int \mathbf{v}_1 dt \cdot \nabla \right) \mathbf{v}_1 \right\rangle, \quad (4.24)$$

which consequently translates into the boundary condition

$$\langle \mathbf{v}_2 \rangle = -\mathbf{v}_{SD} \quad \text{at the interface.} \quad (4.25)$$

The streaming due to the attenuation of the background standing wave in the absence of the particle is negligible [199, 254] and was neglected in the present study.

The FEM model is axisymmetric to limit the computational effort. In the frequency domain study, the fluid domain surrounding the cell is surrounded by a perfectly-matched layer (PML) that absorbs any incoming waves, in order to avoid any influence of the outer wall on the cell. For the steady study, where the acoustic microstreaming is computed, the PML is replaced by a no-slip boundary condition, and the wall effects are avoided by ensuring that the fluid domain is large enough.

	Material of interest	$d[\mu\text{m}]$	$\rho[\text{g cm}^{-3}]$	$E[\text{kPa}]$	$\kappa[\text{TPa}^{-1}]$	$\Phi / \text{ACF} [1]$
a	Water	-	0.9966	-	444.8	-
b	NIH/3T3	-	1.079	3 – 5	378	0.083
	MCF-7	-	1.068	0.31 – 0.6	422	0.047
	HEPG2	-	1.087	0.191 – 0.941	428	0.047
	HT-29	-	1.077	4.09	404	0.060
	MCF-12A	-	1.068	-	377	0.083
	RBC	-	1.099	-	331	0.117
	Polystyrene	-	1.050	-	216	0.175
c	HNC Tu686	-	1.025	-	405	0.032
	HNC 686LN	-	1.060	-	428	0.025
	HNC M4e	-	1.080	-	432	0.029
	HNC 37B	-	1.045	-	440	0.012
d	RBC	-	1.101	-	334	0.109
	RBCfx	-	1.091	-	356	0.090
	WBC	-	1.054	-	393	0.051
	WBCfx	-	1.045	-	400	0.042
	DU-145	-	1.062	-	384	0.059
	DU-145fx	-	1.036	-	404	0.036
	MCF-7	-	1.055	-	373	0.066
	MCF-7fx	-	1.035	-	395	0.043
	LU-HNSCC-25	-	1.061	-	377	0.065
	LU-HNSCC-25fx	-	1.040	-	404	0.038
	Polystyrene	5	1.058	-	273	0.143
	Polystyrene	7	1.059	-	276	0.141
	Melamine	10	1.500	-	124	0.363
	PMMA	3	1.184	-	173	0.255
e	MESC2.10	13.2	-	-	-	0.05
	MESC2.10-diff4d	12.2	-	-	-	0.08
f	Core - shell model	4.2	1.619	-	670	(-0.014) - (-0.029)
g	SaOs-2	17.6	-	0.95	-	0.037
	SaOs-2fx	15.0	-	-	-	0.050
	SaOs-2 Cyto. D	18.9	-	-	-	0.022
	LM5	15.5	-	0.80	-	0.037
	Polystyrene	10.2	1.050	-	250	0.167
h	Cytoplasm	17.6	1.099	0.31	402	-
	Nucleoplasm	13.3	0.996	1.78	446	-
	Nucleolus	4.3	1.744	5.36	446	-

Tab. 4.1: Material properties of eukaryotic cells and some reference inorganic materials. The measurement uncertainty of individual results is omitted for the sake of clarity. Size d generally represents the diameter of a cell, particle, or a part of a cell. Φ is the mathematical symbol for the acoustic contrast factor (ACF).

a Values for water from Karlsen and Bruus [247] used in numerical models, with the dynamic viscosity of 0.8538 mPa s and the bulk viscosity of 2.4 mPa s.

b NIH/3T3 - fibroblast cell; MCF-7 - breast cancer cell; HEPG2 - liver cancer cell; HT-29 - colon cancer cell; MCF-12A - breast cell; RBC - red blood cell; Hartono *et al.* [177]; the compressibility $\kappa = 1/K$ is measured via acoustic manipulation at 3.75 MHz, the other properties are referenced within [177]; density of MCF-12A is assumed.

c HNC Tu686, 686LN, M4e, 37B - head and neck cancer cells whereas M4e & 37B have a higher metastatic potential than Tu686 & 686LN; density and compressibility from Wang *et al.* [180]; acoustic manipulation (data assessed from the graphs) at 1.91 MHz. Wang *et al.* do not report the ACF nor the fluid in which the cells were focused. If the fluid is assumed to be PBS, these are the according ACFs.

d 'fx' denotes a fixed sample. RBC - red blood cell; WBC - white blood cell; DU-145 - prostate cancer cell; MCF-7 - breast cancer cell; LU-HNSCC-25 - head and neck squamous cancer cell; PMMA - polymethylmethacrylat; Cushing *et al.* [178]; through speed of sound measurements of neutrally buoyant samples at 3 MHz; Φ in PBS ($c = 1508.2 \text{ m s}^{-1}$ and $\rho = 1004.00 \text{ kg m}^{-3}$).

e MESC2.10 - human embryonic ventral mesencephalic cell; MESC2.10-diff4d - human embryonic ventral mesencephalic cell differentiated in a special medium for 4 days; Augustsson *et al.* [179]; the acoustic contrast Φ is measured via acoustic manipulation at 1.97 MHz; we multiplied the average Φ from [179] by a factor of 3 to match our definition of Φ .

f Loskutova *et al.* [181] demonstrated a negative ACF, whereas the ACF is dependent on the pressure amplitude. Perfluoropentane core and cellulose nanofiber shell.

g SaOs-2 & LM5 - human bone cancer cell line with a lower respectively higher metastatic potential and ACF data generated during this study. Static E-modulus measured using an RT-DC system and taken from Holenstein *et al.* [153]. The cell diameter was measured either by a cell counter or by manually determining the size from the videos used to compute the ACF. Cells were focused in the $742.1 \text{ kHz} \pm 2 \text{ kHz}$ range.

h Data from the calibrated numerical model of the SaOs-2 cell presented in this study.

5

Conclusions and Outlook

The work presented in chapters 3 and 4 adds to already reported applications of acoustofluidics in a research setting. For completeness the work is placed into the context of the current state of the art introduced in chapter 1 and an outlook for the work is presented containing short and long term goals that can be striven for in order to advance this technology, for instance in the use of cancer cell detection and characterization.

5.1 Focusing objects in fluids

The idea of an optical FCL is not novel and was suggested as early as 1996 [151], but was limited to manipulating one $50\ \mu\text{m}$ diameter glass or PS particle at a time without a background flow. Surprisingly, there has been no continued effort in this sub-field of acoustofluidics since then. Despite this, the optically based FCL presented in this thesis proved to be straightforward to design and implement, and outperformed a skilled operator. Not only could the FCL be used to manipulate micrometer sized objects, but demonstrated that $600\ \text{nm}$ diameter PS particles can be manipulated in flow as well. This feat could be achieved, as the FCL does not find the excitation frequency at which standing pressure waves can be established, but the excitation frequency that performs best for the given task, which in the presented case is focusing objects in a fluid. The precise reason why such small objects can be manipulated is yet to be determined. A hypothesis is that the excitation frequency chosen by the FCL is a narrow band where the acoustic streaming in the system is suppressed, or at least negligible in respect to the ARF. Another possible explanation is that there is hydrodynamic interaction which increases the attraction between the objects. Despite the unknown reason for this sub-micrometer focusing, the capability to manipulate nanometer sized

objects is potentially one of the most promising fields for further research, which can be further exploited by considering the buildup time of the acoustic radiation force and acoustic streaming [105]. Despite the functionality of the presented FCL, the setup and code designed and implemented have many drawbacks which should be addressed. Based on the experience and insight gained during this thesis, followup studies suggested are as following.

The FCL could be tested on even higher modes, or on more dimensions that the FCL is controlling, for instance a side view for two dimensional focusing in glass capillaries. Following this proof-of-concept-study of controlling two or more PTs simultaneously, more complex shapes could be realized, such as predefined patterns [118, 119], organoid formation [116] or enabling multiplexing to increase volumetric throughput [257] of BAW devices. In theory, such augmentations should only require an alteration to what the FCL takes as input parameters.

Another route of inquiry is focused on the setup that the FCL is controlling. The FCL was developed and tested on multiple devices, objects, modes and setups, but was always reliant on a video feed. As practical as this is to troubleshoot, develop and quantify, the optical setup occupies a large physical space. One augmentation would therefore be to reduce the optical setup, or substitute the optical setup altogether. One way this could be done, is by replacing the video feed with a light sheet and a detector. The events of objects passing through the light sheet could be taken as the input parameter. This altered setup could greatly reduce the size of the setup. This idea requires a more complex initial setup and calibration, but once implemented could be even more reliable due to less artifacts and latency compared to the video feed. Acoustic handheld nebulizers [258, 259] could act as inspiration, and the electrical circuit needed to drive a BAW device could be miniaturized [260]. Implementing these improvements could make BAW devices more user friendly, efficient, and could lead to bedside applications.

Furthermore, the limitations of the FCL could be tested concerning the size of objects that can be manipulated in flow. The FCL outperformed a skilled human operator and demonstrated nanometer sized object manipulation, whereas one of the limitations observed was the optical setup as the image quality could not adequately quantify the focusing efficiency of objects below 600 nm. Using an augmented optical setup could potentially enable the manipulation of even smaller objects which can be used for cancer detection and classification, such as exosomes. This increase of optical resolution would however come at a cost of the size of the setup. This is a trade off that would need to be made between a more portable setup and the size of the objects that can be manipulated. Much

further down the line, and with devices with built in streaming suppression [261, 262], and further studies on the multibody dynamics in acoustic devices [263, 206], there might even be applications for circulating tumor (ct)DNA [264] or circulating microRNA [265] isolation.

5.2 Measuring cellular material properties

Knowing the ACF of cancer cells is crucial for the adequate design of acoustofluidic devices and measurement protocols. The ACF invariability between the two cancer cell lines with different metastatic potential demonstrated in this thesis, indicates that more malignant cancer cells will interact with the acoustic field in the same order of magnitude as the less malignant cancer cells. However, the cancer cells used in this thesis decrease in size as they get more malignant [153]. Combining this decrease in size with the size dependent Gor’Kov potential leads to the insight that the more malignant cancer cells will have a smaller radiation force acting upon them, thus they are harder to manipulate. Therefore, any future applications isolating cell populations from one another must take the ACF and size into account. This insight is however based off of one measurement method and the overriding question is if these kind of measurements need to be done for every cell line, or if the material properties from static measurements for cell lines would suffice.

One limiting factor is that the lack of reported dynamic material properties hinders a precise placement of these findings in the current literature. This lack however demonstrates the importance of the dynamic material properties presented here. One of the biggest additions that this thesis provides is the Table 4.1 of values for the ACF, which is a comprehensive overview of the field, and can act as a basis for future discussions. Even though the data provided in the Table 4.1, including the results from the experiments performed during the study presented in chapter 4, should be considered as approximated values, a first link of the dependence of the ACF on the static stiffness of a biological cell could be made. This is highly relevant for any application using acoustic fields, including isolating cancer cells from liquid biopsies.

The mechanical properties of biological cells are hard to measure and depending on which static gold standard method is used, the values can span three orders of magnitude [266]. This is further confounded by the fact that there can be orders of magnitude between static and dynamic material properties [267]. This would therefore suggest, that the ACF for each object population to be manipulated by acoustics needs be determined. This process could, to a certain degree, be

automated by using a FCL to control the frequency switch between a λ and λ -half mode for the pre-focusing and focusing and the automated fresh supply of new sample for the measurement of the ACF using acoustofluidic devices, which could lead to an increased throughput of biological cells measured.

The work presented here only looked at single CTCs. The field of CTCs research is however in a notable shift of paradigm, where new research shows that CTC clusters might be the driving factor of metastasis, instead of previously believed individual CTCs [268]. Gold standard methods that rely on adherent cells or microconstrictions cannot capture the mechanics of such clusters well, but acoustofluidics might be a method that could be harnessed to analyze the mechanics of these CTC clusters. These clusters are by definition larger in size, and with an increase in the size, the radiation forces acting upon the object increases, thus increasing the applicability of acoustofluidics to isolate and measure CTC clusters.

Overall, the insights presented show that there is a large gap in the understanding between the coupling of static and dynamic material parameters, which needs to be addressed. And that acoustofluidics could be a potential method to cope with the current shortcomings of gold standard methods.

5.3 Closing remarks

The two sub-fields of acoustofluidics dealt with in this thesis demonstrate the limitations of the current state of the art and possible use cases of acoustofluidics beyond research settings. Given acoustofluidics' traits of being label-free and contactless, and the developed mathematical foundation provided for acoustofluidics, this technology can tackle many problems where objects in a fluid need to be manipulated.

The Merriam-Webster dictionary defines cancer as "a malignant tumor of potentially unlimited growth that expands locally by invasion and systemically by metastasis.". As cancer is caused by the instability of the genome, life will always be faced with cancer, its spreading, and ultimately cancer related death. That, however, does not mean that through persistently challenging the known and currently impossible, an effort can be made to push the needle and reduce the impact of one of the largest health concerns of the century. One thesis at a time.



Appendix to chapter 3

A.1 Python code for the feedback control loop

Folder `feedback-control-loop-main.zip` contains the entire code for the feedback control loop (FCL). The FCL consists of 3 `.py` functions. `main.py` is the code that needs to be run to start the FCL and is where all variables should be set. `image_manipulation.py` is where all the images functions are written while `fuctions.py` contains the code for all the other functions that the FCL needs to operate. The code can also be accessed via Gitlab and is freely usable and modifiable. The authors would gladly discuss any augmentations and offer tech support.

A.2 Experimental data

The `Figures`, `Matlab_Files`, and `Videos` folders contain various subfolders for each experiment that was run with different particle diameters (5 micrometers `5um`, 1 micrometer `1um`, 600 nanometers `600nm` and 450 nanometers¹ `450nm`) and SaOs-2 cells `SaOs`.

The folder `Figures` contains all the plots of the linewidths (LW) at a given flow rate and particle type. As an example of how to find the saved data: the file `.../Figures/1um/15__20220316-151030.png` is the plot of the linewidth for a flow rate of $15 \mu\text{L min}^{-1}$ (indicated by the 15 before __ in file name). After __ the date and time on which the analysis of the videos took place is noted.

¹The image quality was deemed to low to include the readout of this experiment in the results of the paper, but focusing can be seen in the raw video footage.

Appendix A. Appendix to chapter 3

Analogously, the other figures can be found.

The `Matlab_Files` contains all the `.mat` files for each individual video analysis. As an example, the file `.../MatlabFiles/1um/15.mat` contains the LW variables for a $1\ \mu\text{m}$ particle at a flow rate of $15\ \mu\text{L min}^{-1}$. Analogously, the other `.mat` files can be loaded into Matlab program and read.

The `Videos` folder contains all the trimmed videos that were recorded for a given experiment. The videos were trimmed to analyse each flow rate individually. All videos were recorded with a frame rate of 60, while the frame rate of the image capture can be read at the bottom right hand corner of the video itself. As an example, `...Videos/1um/15_1PS.mp4` is a video at a flow rate of $15\ \mu\text{L min}^{-1}$ of a $1\ \mu\text{m}$ particle. The image capture frame rate was FPS: 20.34. Analogously, the conditions of the other videos can be read.

A.3 Experimental data readout

Folder `MatlabCode` contains all the MATLAB code that was used for the calculations and plots of the experiments. Typically, `video_postproc_1_5.m` is the first file that should be run with the correct folder directories. This calculates the LW data from the separate videos and creates MATLAB variables with the LW and individual LW plots. These files can be found in the directory `.../Experiments/1um/Results_Step_1_Linewidth_Calculation` and analogous folders for the different particle diameters and SaOs-2 cells. `lw_post_process_1_5.m` creates plots with the LW at different flow rates. `lw_all_plots.m` is another code that plots all the data points in a MATLAB figure for the different flows. `plotPhase2` plots the figures for the phase 2 of the FCL with the data that the FCL saves during the iterations. `data_management_2.m` can be used to organize the data. This MATLAB code was however not used.

B

Appendix to chapter 4

B.1 Data analysis of the experimental data

The low metastatic parental cell line SaOs-2 was chosen as the baseline. This baseline was not only used to compare effects of treatments on the ACF and to analyse the difference between the metastatic potential and its influence on the ACF, but was used to calibrate the setup and create the workflow for the experiments. The calibration of the setup and the creation of the workflow included a preliminary data analysis on the robustness of the data. This was in part comprised of a check for normality for the two cell lines and two different conditions and a comparison of the outcome between different observers. All data was analysed with R 4.2.1 in R studio.

B.1.1 Data normality

The data sets of the SaOs-2, fixed SaOs-2 and LM5 cells were tested for normality with a Shapiro test. If the p-value of the Shapiro test is greater than 0.05, then the data is considered to be normally distributed [269]. The data was found to be normal as seen in table B.1 and the QQ-plots in Fig. B.1.

Cell type	p-value
SaOs-2	0.4052
Fixed SaOs-2	0.5708
LM5	0.09502

Tab. B.1: The ACF data of the SaOs-2, fixed SaOs-2 and LM5 cells was tested for normality. If the p-value is greater than 0.05 the data is considered normal, which is the case for all cell lines and conditions presented here.

B.1.2 Data comparison between observers

Furthermore, the experiments to measure the ACF for the SaOs-2 cells were repeated by two observers (C.H. and D.B. [270]) to test the inter-observer variability. The measurements do not seem to be observer dependent as seen in table B.2 and Fig. B.2.

Observer	Mean Φ / ACF [1]
D.B.	0.0366
C.H.	0.0372

Tab. B.2: Comparison of the data of two observers where the data did not show a large variation between the observers C.H. and D.B. for the baseline SaOs-2 cells, especially as the data was usually rounded to 3 decimal points which would result in both values for the ACF being 0.037.

B.1. Data analysis of the experimental data

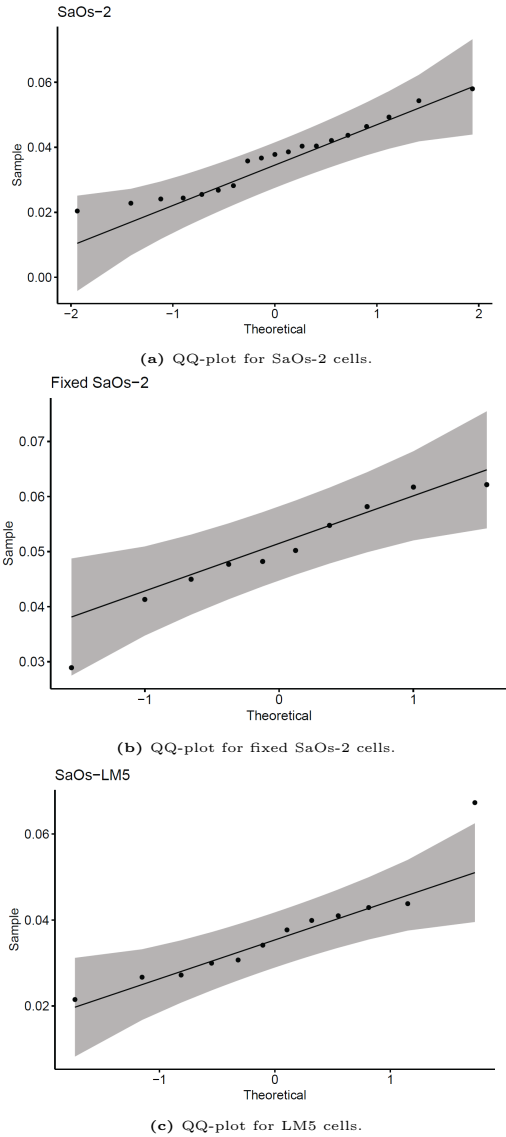


Fig. B.1: QQ-plots for the SaOs-2, fixed SaOs-2 and LM5 cells indicating normality of the data sets.

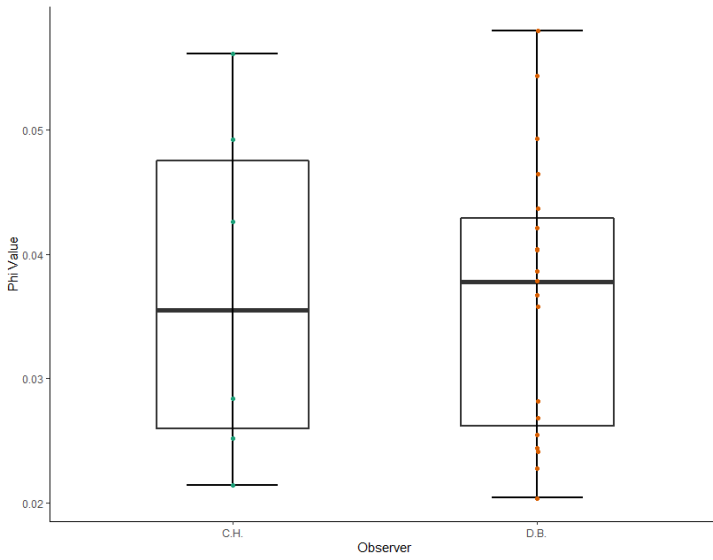


Fig. B.2: Comparison of the data of two observers where the data did not show a large variation between the observers C.H. ($n = 6$) and D.B. ($n = 19$) for the baseline SaOs-2 cells.

Bibliography

- [1] S. Negrini, V. G. Gorgoulis, and T. D. Halazonetis. “Genomic instability—an evolving hallmark of cancer”. In: *Nature reviews Molecular cell biology* 11.3 (2010), pp. 220–228.
- [2] M. Gerlinger et al. “Intratumor heterogeneity and branched evolution revealed by multiregion sequencing”. In: *N Engl J Med* 366 (2012), pp. 883–892.
- [3] D. Hanahan and R. A. Weinberg. “Hallmarks of cancer: the next generation”. eng. In: *Cell* 144.5 (Mar. 2011), pp. 646–674. ISSN: 1097-4172. DOI: 10.1016/j.cell.2011.02.013.
- [4] B. N. Ames and L. S. Gold. “Paracelsus to parascience: the environmental cancer distraction”. In: *Mutation Research/Fundamental and Molecular Mechanisms of Mutagenesis* 447.1 (2000), pp. 3–13.
- [5] D. Belpomme et al. “The multitude and diversity of environmental carcinogens”. In: *Environmental research* 105.3 (2007), pp. 414–429.
- [6] “Cancer facts & figures 2023”. In: *American Cancer Society* (2023).
- [7] Merriam-Webster. “Cancer”. In: *Merriam-Webster.com dictionary*. URL: <https://www.merriam-webster.com/dictionary/cancer> (visited on 11/28/2022).
- [8] J. Folkman and R. Kalluri. “Cancer without disease”. In: *Nature* 427.6977 (2004), pp. 787–787.
- [9] J. Boutry et al. “The evolution and ecology of benign tumors”. In: *Biochimica et Biophysica Acta (BBA)-Reviews on Cancer* 1877.1 (2022), p. 188643.
- [10] S. Retsas. *Palaeo-oncology: The Antiquity of Cancer*. Farrand, 1986. ISBN: 9781850830061.
- [11] J. H. Breasted. “The Edwin Smith Surgical Papyrus: published in facsimile and hieroglyphic transliteration with translation and commentary in two volumes”. In: (1930).
- [12] R. L. Siegel, K. D. Miller, and A. Jemal. “Cancer statistics, 2020”. In: *CA: A Cancer Journal for Clinicians* 70.1 (2020), pp. 7–30.
- [13] NIH. “National Cancer Institute”. In: *Cancer types*. URL: <https://www.cancer.gov/types> (visited on 12/06/2022).
- [14] D. Hanahan and R. A. Weinberg. “The hallmarks of cancer”. In: *cell* 100.1 (2000), pp. 57–70.
- [15] R. Bianchi et al. *The Egyptians*. University of Chicago Press, 1997.
- [16] S. Mukherjee. *The emperor of all maladies: a biography of cancer*. Simon and Schuster, 2011.

Bibliography

- [17] A. C. Aufderheide. *The scientific study of mummies*. Cambridge University Press, 2003.
- [18] L. Mirabello, R. J. Troisi, and S. A. Savage. “Osteosarcoma incidence and survival rates from 1973 to 2004: data from the Surveillance, Epidemiology, and End Results Program”. In: *Cancer: Interdisciplinary International Journal of the American Cancer Society* 115.7 (2009), pp. 1531–1543.
- [19] B. P. Himelstein and J. P. Dormans. “Malignant bone tumors of childhood”. In: *Pediatric Clinics* 43.4 (1996), pp. 967–984.
- [20] A. Luetke et al. “Osteosarcoma treatment—where do we stand? A state of the art review”. In: *Cancer treatment reviews* 40.4 (2014), pp. 523–532.
- [21] P. Picci. “Osteosarcoma (osteogenic sarcoma)”. In: *Orphanet journal of rare diseases* 2.1 (2007), pp. 1–4.
- [22] M. Kalia. “Personalized oncology: Recent advances and future challenges”. In: *Metabolism* 62 (2013), S11–S14.
- [23] E. L. Psaty and A. C. Halpern. “Current and emerging technologies in melanoma diagnosis: the state of the art”. In: *Clinics in dermatology* 27.1 (2009), pp. 35–45.
- [24] P. Martin-Hirsch et al. “Efficacy of cervical-smear collection devices: a systematic review and meta-analysis”. In: *The Lancet* 354.9192 (1999), pp. 1763–1770.
- [25] K. B. Kuchenbaecker et al. “Risks of breast, ovarian, and contralateral breast cancer for BRCA1 and BRCA2 mutation carriers”. In: *Jama* 317.23 (2017), pp. 2402–2416.
- [26] R. Guo et al. “Ultrasound imaging technologies for breast cancer detection and management: a review”. In: *Ultrasound in medicine & biology* 44.1 (2018), pp. 37–70.
- [27] M. A. Kouvaraki et al. “Role of preoperative ultrasonography in the surgical management of patients with thyroid cancer”. In: *Surgery* 134.6 (2003), pp. 946–954.
- [28] M.-L. Bafounta et al. “Ultrasonography or palpation for detection of melanoma nodal invasion: a meta-analysis”. In: *The lancet oncology* 5.11 (2004), pp. 673–680.
- [29] E. A. Morris. “Breast cancer imaging with MRI”. In: *Radiologic Clinics* 40.3 (2002), pp. 443–466.
- [30] G. D. Rubin. “Lung nodule and cancer detection in CT screening”. In: *Journal of thoracic imaging* 30.2 (2015), p. 130.
- [31] L. Schrevels et al. “The role of PET scan in diagnosis, staging, and management of non-small cell lung cancer”. In: *The oncologist* 9.6 (2004), pp. 633–643.
- [32] A. M. Veitch et al. “Optimizing early upper gastrointestinal cancer detection at endoscopy”. In: *Nature reviews Gastroenterology & hepatology* 12.11 (2015), pp. 660–667.
- [33] X. Filella and L. Foj. “Prostate cancer detection and prognosis: from prostate specific antigen (PSA) to exosomal biomarkers”. In: *International journal of molecular sciences* 17.11 (2016), p. 1784.

- [34] S. F. Shariat and C. G. Roehrborn. “Using biopsy to detect prostate cancer”. In: *Reviews in Urology* 10.4 (2008), p. 262.
- [35] A. M. Wolf et al. “American Cancer Society guideline for the early detection of prostate cancer: update 2010”. In: *CA: a cancer journal for clinicians* 60.2 (2010), pp. 70–98.
- [36] G. L. Andriole et al. “Mortality results from a randomized prostate-cancer screening trial”. In: *New England journal of medicine* 360.13 (2009), pp. 1310–1319.
- [37] F. H. Schröder et al. “Screening and prostate-cancer mortality in a randomized European study”. In: *New England journal of medicine* 360.13 (2009), pp. 1320–1328.
- [38] J. R. Prensner et al. “Beyond PSA: the next generation of prostate cancer biomarkers”. In: *Science translational medicine* 4.127 (2012), 127rv3–127rv3.
- [39] G. Ploussard and A. De La Taille. “Urine biomarkers in prostate cancer”. In: *Nature Reviews Urology* 7.2 (2010), pp. 101–109.
- [40] A. Jemal et al. “Cancer statistics, 2007”. In: *CA: a cancer journal for clinicians* 57.1 (2007), pp. 43–66.
- [41] B. W. Park et al. “Clinical breast examination for screening of asymptomatic women: the importance of clinical breast examination for breast cancer detection”. In: *Yonsei medical journal* 41.3 (2000), pp. 312–318.
- [42] D. A. Kennedy, T. Lee, and D. Seely. “A comparative review of thermography as a breast cancer screening technique”. In: *Integrative cancer therapies* 8.1 (2009), pp. 9–16.
- [43] J. G. Elmore et al. “Ten-year risk of false positive screening mammograms and clinical breast examinations”. In: *New England Journal of Medicine* 338.16 (1998), pp. 1089–1096.
- [44] A. Sobti, P. Sobti, and L. G. Keith. “Screening and diagnostic mammograms: why the gold standard does not shine more brightly.” In: *International journal of fertility and women’s medicine* 50.5 Pt 1 (2005), pp. 199–206.
- [45] T. Osako et al. “Diagnostic mammography and ultrasonography for palpable and nonpalpable breast cancer in women aged 30 to 39 years”. In: *Breast cancer* 14.3 (2007), pp. 255–259.
- [46] P. Song et al. “Limitations and opportunities of technologies for the analysis of cell-free DNA in cancer diagnostics”. In: *Nature biomedical engineering* 6.3 (2022), pp. 232–245.
- [47] J. P. Gregg, T. Li, and K. Y. Yoneda. “Molecular testing strategies in non-small cell lung cancer: optimizing the diagnostic journey”. In: *Translational lung cancer research* 8.3 (2019), p. 286.
- [48] K. Pantel, C. Alix-Panabières, and S. Riethdorf. “Cancer micrometastases”. In: *Nature reviews Clinical oncology* 6.6 (2009), pp. 339–351.

Bibliography

- [49] P. Pinzani et al. “Updates on liquid biopsy: Current trends and future perspectives for clinical application in solid tumors”. In: *Clinical Chemistry and Laboratory Medicine (CCLM)* 59.7 (2021), pp. 1181–1200.
- [50] H. Cho et al. “Microfluidic technologies for circulating tumor cell isolation”. In: *Analyst* 143.13 (2018), pp. 2936–2970.
- [51] C. L. Chaffer and R. A. Weinberg. “A perspective on cancer cell metastasis”. In: *Science* 331.6024 (2011), pp. 1559–1564.
- [52] J. Fares et al. “Molecular principles of metastasis: a hallmark of cancer revisited”. In: *Signal transduction and targeted therapy* 5.1 (2020), p. 28.
- [53] V. Bobek et al. “Detection and cultivation of circulating tumor cells in malignant pleural mesothelioma”. In: *Anticancer research* 34.5 (2014), pp. 2565–2569.
- [54] S. I. Mohammed et al. “Lymph-circulating tumor cells show distinct properties to blood-circulating tumor cells and are efficient metastatic precursors”. In: *Molecular Oncology* 13.6 (2019), pp. 1400–1418.
- [55] C. L. Weston, M. J. Glantz, and J. R. Connor. “Detection of cancer cells in the cerebrospinal fluid: current methods and future directions”. In: *Fluids and Barriers of the CNS* 8.1 (2011), pp. 1–9.
- [56] G. Disibio and S. W. French. “Metastatic patterns of cancers: results from a large autopsy study”. In: *Archives of pathology & laboratory medicine* 132.6 (2008), pp. 931–939.
- [57] M. Macgregor-Ramiata et al. “A platform for selective immuno-capture of cancer cells from urine”. In: *Biosensors and Bioelectronics* 96 (2017), pp. 373–380.
- [58] W. Zhang et al. “Antibody-modified hydroxyapatite surfaces for the efficient capture of bladder cancer cells in a patient’s urine without recourse to any sample pre-treatment”. In: *Journal of Materials Chemistry B* 5.40 (2017), pp. 8125–8132.
- [59] M. Zavyalova et al. “Intravasation as a key step in cancer metastasis”. In: *Biochemistry (Moscow)* 84.7 (2019), pp. 762–772.
- [60] D. Lin et al. “Circulating tumor cells: Biology and clinical significance”. In: *Signal transduction and targeted therapy* 6.1 (2021), p. 404.
- [61] C. Alix-Panabières and K. Pantel. “Challenges in circulating tumour cell research”. In: *Nature Reviews Cancer* 14.9 (2014), pp. 623–631.
- [62] P. Paterlini-Brechot and N. L. Benali. “Circulating tumor cells (CTC) detection: clinical impact and future directions”. In: *Cancer letters* 253.2 (2007), pp. 180–204.
- [63] K. J. Luzzi et al. “Multistep nature of metastatic inefficiency: dormancy of solitary cells after successful extravasation and limited survival of early micrometastases”. In: *The American journal of pathology* 153.3 (1998), pp. 865–873.
- [64] K. Naidoo and S. E. Pinder. “Micro-and macro-metastasis in the axillary lymph node: a review”. In: *the surgeon* 15.2 (2017), pp. 76–82.
- [65] C. Alix-Panabières and K. Pantel. “Circulating tumor cells: liquid biopsy of cancer”. In: *Clinical chemistry* 59.1 (2013), pp. 110–118.

- [66] E. K. Sackmann, A. L. Fulton, and D. J. Beebe. “The present and future role of microfluidics in biomedical research”. In: *Nature* 507.7491 (2014), pp. 181–189.
- [67] M. Wu et al. “Acoustofluidic separation of cells and particles”. In: *Microsystems & nanoengineering* 5.1 (2019), p. 32.
- [68] A. van Leeuwenhoek. *Epistolae physiologicae super compluribus naturae arcanis*. Apud Adrianum Beman, 1719.
- [69] B Bracegirdle. “The history of staining”. In: *Conn’s Biological Stains*. Taylor & Francis, 2020, pp. 15–21.
- [70] E. Lazarides. “Immunofluorescence studies on the structure of actin filaments in tissue culture cells.” In: *Journal of Histochemistry & Cytochemistry* 23.7 (1975), pp. 507–528.
- [71] M. Faridi et al. “MicroBubble activated acoustic cell sorting”. In: *Biomedical microdevices* 19.2 (2017), pp. 1–7.
- [72] K. Cushing et al. “Reducing WBC background in cancer cell separation products by negative acoustic contrast particle immuno-acoustophoresis”. In: *Analytica chimica acta* 1000 (2018), pp. 256–264.
- [73] B. D. Plouffe, S. K. Murthy, and L. H. Lewis. “Fundamentals and application of magnetic particles in cell isolation and enrichment: a review”. In: *Reports on Progress in Physics* 78.1 (2014), p. 016601.
- [74] M. Munz, P. A. Baeuerle, and O. Gires. “The emerging role of EpCAM in cancer and stem cell signaling”. In: *Cancer research* 69.14 (2009), pp. 5627–5629.
- [75] J. Chan, C. Ng, and P. Hui. “A simple guide to the terminology and application of leucocyte monoclonal antibodies”. In: *Histopathology* 12.5 (1988), pp. 461–480.
- [76] D Howard et al. “A sample preparation and analysis system for identification of circulating tumor cells”. In: *Journal of Clinical Ligand Assay* 25 (2002), pp. 104–10.
- [77] T Fehm et al. “Methods for isolating circulating epithelial cells and criteria for their classification as carcinoma cells”. In: *Cytotherapy* 7.2 (2005), pp. 171–185.
- [78] J.-C. Goeminne, T Guillaume, and M. Symann. “Pitfalls in the detection of disseminated non-hematological tumor cells”. In: *Annals of oncology* 11.7 (2000), pp. 785–792.
- [79] K.-A. Hyun et al. “Epithelial-to-mesenchymal transition leads to loss of EpCAM and different physical properties in circulating tumor cells from metastatic breast cancer”. In: *Oncotarget* 7.17 (2016), p. 24677.
- [80] K. Ward et al. “Epithelial cell adhesion molecule is expressed in a subset of sarcomas and correlates to the degree of cytological atypia in leiomyosarcomas”. In: *Molecular and clinical oncology* 3.1 (2015), pp. 31–36.
- [81] D. Di Carlo. “Inertial microfluidics”. In: *Lab on a Chip* 9.21 (2009), pp. 3038–3046.
- [82] J. Takagi et al. “Continuous particle separation in a microchannel having asymmetrically arranged multiple branches”. In: *Lab on a Chip* 5.7 (2005), pp. 778–784.

Bibliography

- [83] Z. Wu et al. “Soft inertial microfluidics for high throughput separation of bacteria from human blood cells”. In: *Lab on a Chip* 9.9 (2009), pp. 1193–1199.
- [84] T. Salafi, Y. Zhang, and Y. Zhang. “A review on deterministic lateral displacement for particle separation and detection”. In: *Nano-Micro Letters* 11.1 (2019), pp. 1–33.
- [85] L. R. Huang et al. “Continuous particle separation through deterministic lateral displacement”. In: *Science* 304.5673 (2004), pp. 987–990.
- [86] C.-H. Lee et al. “Examining the lateral displacement of HL60 cells rolling on asymmetric P-selectin patterns”. In: *Langmuir* 27.1 (2011), pp. 240–249.
- [87] S. Bose et al. “Affinity flow fractionation of cells via transient interactions with asymmetric molecular patterns”. In: *Scientific reports* 3.1 (2013), pp. 1–8.
- [88] T. Y. Lee et al. “An integrated microfluidic chip for one-step isolation of circulating tumor cells”. In: *Sensors and Actuators B: Chemical* 238 (2017), pp. 1144–1150.
- [89] A. Singh et al. “Adhesion strength-based, label-free isolation of human pluripotent stem cells”. In: *Nature methods* 10.5 (2013), pp. 438–444.
- [90] G. De Rubis, S. R. Krishnan, and M. Bebawy. “Liquid biopsies in cancer diagnosis, monitoring, and prognosis”. In: *Trends in pharmacological sciences* 40.3 (2019), pp. 172–186.
- [91] S. Gkoutela et al. “Circulating tumor cell clustering shapes DNA methylation to enable metastasis seeding”. In: *Cell* 176.1-2 (2019), pp. 98–112.
- [92] W. Liang et al. “Microfluidic-based cancer cell separation using active and passive mechanisms”. In: *Microfluidics and Nanofluidics* 24.4 (2020), pp. 1–19.
- [93] A. A. S. Bhagat et al. “Microfluidics for cell separation”. In: *Medical & biological engineering & computing* 48.10 (2010), pp. 999–1014.
- [94] C. W. Shields IV, C. D. Reyes, and G. P. López. “Microfluidic cell sorting: a review of the advances in the separation of cells from debulking to rare cell isolation”. In: *Lab on a Chip* 15.5 (2015), pp. 1230–1249.
- [95] M. Toner and D. Irimia. “Blood-on-a-chip”. In: *Annu. Rev. Biomed. Eng.* 7 (2005), pp. 77–103.
- [96] H. W. Hou et al. “Microfluidic devices for blood fractionation”. In: *Micromachines* 2.3 (2011), pp. 319–343.
- [97] D. Robert et al. “Cell sorting by endocytotic capacity in a microfluidic magnetophoresis device”. In: *Lab on a chip* 11.11 (2011), pp. 1902–1910.
- [98] T. Zhu et al. “Continuous-flow ferrohydrodynamic sorting of particles and cells in microfluidic devices”. In: *Microfluidics and nanofluidics* 13.4 (2012), pp. 645–654.
- [99] E. B. Cummings and A. K. Singh. “Dielectrophoresis in microchips containing arrays of insulating posts: theoretical and experimental results”. In: *Analytical chemistry* 75.18 (2003), pp. 4724–4731.

- [100] L. M. Barrett et al. “Dielectrophoretic manipulation of particles and cells using insulating ridges in faceted prism microchannels”. In: *Analytical chemistry* 77.21 (2005), pp. 6798–6804.
- [101] S.-K. Hoi et al. “Microfluidic sorting system based on optical force switching”. In: *Applied Physics B* 97.4 (2009), pp. 859–865.
- [102] A. Y. Lau, L. P. Lee, and J. W. Chan. “An integrated optofluidic platform for Raman-activated cell sorting”. In: *Lab on a Chip* 8.7 (2008), pp. 1116–1120.
- [103] A. Lamprecht et al. “Rotational speed measurements of small spherical particles driven by acoustic viscous torques utilizing an optical trap”. In: *Journal of Micromechanics and Microengineering* 31.3 (2021), p. 034004.
- [104] C. Goering and J. Dual. “Dynamic measurement of the acoustic streaming time constant utilizing an optical tweezer”. In: *Physical Review E* 104.2 (2021), p. 025104.
- [105] C. Goering and J. Dual. “Measuring the effects of a pulsed excitation on the buildup of acoustic streaming and the acoustic radiation force utilizing an optical tweezer”. In: *Physical Review E* 105.5 (2022), p. 055103.
- [106] J. Hultström et al. “Proliferation and viability of adherent cells manipulated by standing-wave ultrasound in a microfluidic chip”. In: *Ultrasound in medicine & biology* 33.1 (2007), pp. 145–151.
- [107] J. Rufo et al. “Acoustofluidics for biomedical applications”. In: *Nature Reviews Methods Primers* 2.30 (2022), pp. 2662–8449.
- [108] Y. Q. Fu et al. “Advances in piezoelectric thin films for acoustic biosensors, acoustofluidics and lab-on-chip applications”. In: *Progress in Materials Science* 89 (2017), pp. 31–91.
- [109] G. Destgeer and H. J. Sung. “Recent advances in microfluidic actuation and micro-object manipulation via surface acoustic waves”. In: *Lab on a Chip* 15.13 (2015), pp. 2722–2738.
- [110] Y. Xie, H. Bachman, and T. J. Huang. “Acoustofluidic methods in cell analysis”. In: *TrAC Trends in Analytical Chemistry* 117 (2019), pp. 280–290.
- [111] C. Eckart. “Vortices and streams caused by sound waves”. In: *Physical review* 73.1 (1948), p. 68.
- [112] A. Pavlic et al. “Sharp-edge-based acoustofluidic chip capable of programmable pumping, mixing, cell focusing, and trapping”. In: *Physics of Fluids* 35.2 (2023), p. 022006.
- [113] A. Pavlic et al. “Efficient modeling of sharp-edge acoustofluidics”. In: *Frontiers in Physics* 11 (), p. 305.
- [114] J. Dual and D. Möller. “Acoustofluidics 4: Piezoelectricity and application in the excitation of acoustic fields for ultrasonic particle manipulation”. In: *Lab on a Chip* 12.3 (2012), pp. 506–514.
- [115] M. S. Gerlt et al. “Focusing of Micrometer-Sized Metal Particles Enabled by Reduced Acoustic Streaming via Acoustic Forces in a Round Glass Capillary”. In: *Phys. Rev. Applied* 17 (1 2022), p. 014043.

Bibliography

- [116] K. Olofsson et al. “Ultrasound-based scaffold-free core-shell multicellular tumor spheroid formation”. In: *Micromachines* 12.3 (2021), p. 329.
- [117] M. Gerlt et al. “Acoustofluidic medium exchange for preparation of electrocompetent bacteria using channel wall trapping”. In: *Lab on a Chip* 21.22 (2021), pp. 4487–4497.
- [118] D. V. Deshmukh et al. “Continuous Production of Acoustically Patterned Cells Within Hydrogel Fibers for Musculoskeletal Tissue Engineering”. In: *Advanced Functional Materials* (2022), p. 2113038.
- [119] J. P. Armstrong et al. “Engineering anisotropic muscle tissue using acoustic cell patterning”. In: *Advanced Materials* 30.43 (2018), p. 1802649.
- [120] S. Peterson, G. Perkins, and C. Baker. “Development of an ultrasonic blood cell separator”. In: *Proceedings of the 8th Annual International Conference of the IEEE Engineering in Medicine and Biology Society*. 1986, pp. 154–156.
- [121] N. Harris et al. “A silicon microfluidic ultrasonic separator”. In: *Sensors and Actuators B: Chemical* 95.1-3 (2003), pp. 425–434.
- [122] J. J. Hawkes and W. T. Coakley. “Force field particle filter, combining ultrasound standing waves and laminar flow”. In: *Sensors and Actuators B: Chemical* 75.3 (2001), pp. 213–222.
- [123] M. Evander et al. “Noninvasive acoustic cell trapping in a microfluidic perfusion system for online bioassays”. In: *Analytical chemistry* 79.7 (2007), pp. 2984–2991.
- [124] F. Petersson et al. “Separation of lipids from blood utilizing ultrasonic standing waves in microfluidic channels”. In: *Analyst* 129.10 (2004), pp. 938–943.
- [125] F. Petersson et al. “Free flow acoustophoresis: microfluidic-based mode of particle and cell separation”. In: *Analytical chemistry* 79.14 (2007), pp. 5117–5123.
- [126] R. Jiang et al. “Rapid isolation of circulating cancer associated fibroblasts by acoustic microstreaming for assessing metastatic propensity of breast cancer patients”. In: *Lab on a Chip* 21.5 (2021), pp. 875–887.
- [127] M. Antfolk et al. “Acoustofluidic, label-free separation and simultaneous concentration of rare tumor cells from white blood cells”. In: *Analytical chemistry* 87.18 (2015), pp. 9322–9328.
- [128] M. Antfolk et al. “A single inlet two-stage acoustophoresis chip enabling tumor cell enrichment from white blood cells”. In: *Lab on a chip* 15.9 (2015), pp. 2102–2109.
- [129] C. Magnusson et al. “Clinical-scale cell-surface-marker independent acoustic microfluidic enrichment of tumor cells from blood”. In: *Analytical chemistry* 89.22 (2017), pp. 11954–11961.
- [130] K. Olofsson, B. Hammarström, and M. Wiklund. “Acoustic separation of living and dead cells using high density medium”. In: *Lab on a chip* 20.11 (2020), pp. 1981–1990.
- [131] E. Undvall Anand et al. “Two-Step Acoustophoresis Separation of Live Tumor Cells from Whole Blood”. In: *Analytical chemistry* 93.51 (2021), pp. 17076–17085.

- [132] P. Augustsson et al. “Microfluidic, label-free enrichment of prostate cancer cells in blood based on acoustophoresis”. In: *Analytical chemistry* 84.18 (2012), pp. 7954–7962.
- [133] F. Olm et al. “Label-free neuroblastoma cell separation from hematopoietic progenitor cell products using acoustophoresis-towards cell processing of complex biological samples”. In: *Scientific reports* 9.1 (2019), pp. 1–11.
- [134] M. Antfolk et al. “Label-free single-cell separation and imaging of cancer cells using an integrated microfluidic system”. In: *Scientific reports* 7.1 (2017), pp. 1–12.
- [135] P. Bröker et al. “A nanostructured SAW chip-based biosensor detecting cancer cells”. In: *Sensors and Actuators B: Chemical* 165.1 (2012), pp. 1–6.
- [136] K. Wang et al. “Sorting of tumour cells in a microfluidic device by multi-stage surface acoustic waves”. In: *Sensors and Actuators B: Chemical* 258 (2018), pp. 1174–1183.
- [137] X. Ding et al. “Cell separation using tilted-angle standing surface acoustic waves”. In: *Proceedings of the National Academy of Sciences* 111.36 (2014), pp. 12992–12997.
- [138] A. A. Nawaz et al. “Intelligent image-based deformation-assisted cell sorting with molecular specificity”. In: *Nature Methods* 17.6 (2020), pp. 595–599.
- [139] P. Augustsson et al. “Automated and temperature-controlled micro-PIV measurements enabling long-term-stable microchannel acoustophoresis characterization”. In: *Lab on a Chip* 11.24 (2011), pp. 4152–4164.
- [140] M. S. Gerlt et al. “Reduced Etch Lag and High Aspect Ratios by Deep Reactive Ion Etching (DRIE)”. In: *Micromachines* 12.5 (May 2021), p. 542.
- [141] A. G. Steckel et al. “Fabrication, Characterization, and Simulation of Glass Devices with Al N Thin-Film Transducers for Excitation of Ultrasound Resonances”. In: *Physical Review Applied* 16.1 (2021), p. 014014.
- [142] P. Reichert et al. “Thin film piezoelectrics for bulk acoustic wave (BAW) acoustophoresis”. In: *Lab on a Chip* 18.23 (2018), pp. 3655–3667.
- [143] D. Carugo et al. “A thin-reflector microfluidic resonator for continuous-flow concentration of microorganisms: a new approach to water quality analysis using acoustofluidics”. In: *Lab on a Chip* 14.19 (2014), pp. 3830–3842.
- [144] M. S. Gerlt et al. “Acoustofluidic medium exchange for preparation of electro-competent bacteria using channel wall trapping”. In: *Lab Chip* 21 (22 2021), pp. 4487–4497. doi: 10.1039/D1LC00406A.
- [145] G. Goddard et al. “Ultrasonic particle-concentration for sheathless focusing of particles for analysis in a flow cytometer”. In: *Cytometry Part A: The Journal of the International Society for Analytical Cytology* 69.2 (2006), pp. 66–74.
- [146] P. P. A. Suthanthiraraj et al. “One-dimensional acoustic standing waves in rectangular channels for flow cytometry”. In: *Methods* 57.3 (2012), pp. 259–271.

Bibliography

- [147] D. M. Kalb et al. “Resonance control of acoustic focusing systems through an environmental reference table and impedance spectroscopy”. In: *Plos one* 13.11 (2018), e0207532.
- [148] V. Farmehini et al. “Real-Time Detection and Control of Microchannel Resonance Frequency in Acoustic Trapping Systems by Monitoring Amplifier Supply Currents”. In: *ACS sensors* 6.10 (2021), pp. 3765–3772.
- [149] J. Dual et al. “Acoustofluidics 6: Experimental characterization of ultrasonic particle manipulation devices”. In: *Lab on a Chip* 12.5 (2012), pp. 852–862.
- [150] V. Vitali et al. “Differential impedance spectra analysis reveals optimal actuation frequency in bulk mode acoustophoresis”. In: *Scientific reports* 9.1 (2019), pp. 1–10.
- [151] M. T. M. Takeuchi, H. A. H. Abe, and K. Y. K. Yamanouchi. “Ultrasonic micromanipulator using visual feedback”. In: *Japanese journal of applied physics* 35.5S (1996), p. 3244.
- [152] F. J. Alenghat et al. “Analysis of cell mechanics in single vinculin-deficient cells using a magnetic tweezer”. In: *Biochemical and biophysical research communications* 277.1 (2000), pp. 93–99.
- [153] C. N. Holenstein et al. “The relationship between metastatic potential and in vitro mechanical properties of osteosarcoma cells”. In: *Molecular biology of the cell* 30.7 (2019), pp. 887–898.
- [154] R. M. Hochmuth. “Micropipette aspiration of living cells”. In: *Journal of biomechanics* 33.1 (2000), pp. 15–22.
- [155] O. Otto et al. “Real-time deformability cytometry: on-the-fly cell mechanical phenotyping”. In: *Nature methods* 12.3 (2015), pp. 199–202.
- [156] S. Heyden and M. Ortiz. “Oncotripsy: Targeting cancer cells selectively via resonant harmonic excitation”. In: *Journal of the Mechanics and Physics of Solids* 92 (2016), pp. 164–175.
- [157] E. Schibber et al. “A dynamical model of oncotripsy by mechanical cell fatigue: selective cancer cell ablation by low-intensity pulsed ultrasound”. In: *Proceedings of the Royal Society A* 476.2236 (2020), p. 20190692.
- [158] C. Rabut et al. “Ultrasound technologies for imaging and modulating neural activity”. In: *Neuron* 108.1 (2020), pp. 93–110.
- [159] Y. Tufail et al. “Transcranial pulsed ultrasound stimulates intact brain circuits”. In: *Neuron* 66.5 (2010), pp. 681–694.
- [160] S. Ibsen et al. “Sonogenetics is a non-invasive approach to activating neurons in *Caenorhabditis elegans*”. In: *Nature communications* 6.1 (2015), pp. 1–12.
- [161] D. Saslow et al. “Clinical breast examination: practical recommendations for optimizing performance and reporting”. In: *CA: a cancer journal for clinicians* 54.6 (2004), pp. 327–344.
- [162] S. McDonald, D. Saslow, and M. H. Alciati. “Performance and reporting of clinical breast examination: a review of the literature”. In: *CA: a cancer journal for clinicians* 54.6 (2004), pp. 345–361.

- [163] K. Hoyt et al. “Tissue elasticity properties as biomarkers for prostate cancer”. In: *Cancer Biomarkers* 4.4-5 (2008), pp. 213–225.
- [164] A. Sarvazyan et al. “Biophysical bases of elasticity imaging”. In: *Acoustical imaging* (1995), pp. 223–240.
- [165] C. Sumi, K. Nakayama, and M. Kubota. “An effective ultrasonic strain measurement-based shear modulus reconstruction technique for superficial tissues-demonstration on in vitro pork ribs and in vivo human breast tissues”. In: *Physics in Medicine & Biology* 45.6 (2000), p. 1511.
- [166] R. Masuzaki et al. “Assessing liver tumor stiffness by transient elastography”. In: *Hepatology international* 1 (2007), pp. 394–397.
- [167] L. Mahoney and A. Csima. “Efficiency of palpation in clinical detection of breast cancer.” In: *Canadian Medical Association Journal* 127.8 (1982), p. 729.
- [168] M. J. Paszek et al. “Tensional homeostasis and the malignant phenotype”. In: *Cancer cell* 8.3 (2005), pp. 241–254.
- [169] D. A. Müller and U. Silvan. “On the biomechanical properties of osteosarcoma cells and their environment”. In: *The International journal of developmental biology* 63.1-2 (2019), pp. 1–8.
- [170] M. A. Steffey et al. “Mechanical properties of canine osteosarcoma-affected antebrachia”. In: *Veterinary Surgery* 46.4 (2017), pp. 539–548.
- [171] J. Fogh and G. Trempe. “New human tumor cell lines”. In: *Human tumor cells in vitro*. Springer, 1975, pp. 115–159.
- [172] V. Swaminathan et al. “Mechanical Stiffness Grades Metastatic Potential in Patient Tumor Cells and in Cancer Cell Lines Mechanical Stiffness of Cells Dictates Cancer Cell Invasion”. In: *Cancer research* 71.15 (2011), pp. 5075–5080.
- [173] S. E. Cross et al. “Nanomechanical analysis of cells from cancer patients”. In: *Nano-Enabled Medical Applications*. Jenny Stanford Publishing, 2020, pp. 547–566.
- [174] M. Kalli and T. Stylianopoulos. “Defining the role of solid stress and matrix stiffness in cancer cell proliferation and metastasis”. In: *Frontiers in oncology* 8 (2018), p. 55.
- [175] D. M. Gilkes and D. Wirtz. “Tumour mechanopathology: cutting the stress out”. In: *Nature Biomedical Engineering* 1.1 (2017), pp. 1–2.
- [176] H. Mohammadi and E. Sahai. “Mechanisms and impact of altered tumour mechanics”. In: *Nature cell biology* 20.7 (2018), pp. 766–774.
- [177] D. Hartono et al. “On-chip measurements of cell compressibility via acoustic radiation”. In: *Lab on a Chip* 11.23 (2011), pp. 4072–4080.
- [178] K. W. Cushing et al. “Ultrasound characterization of microbead and cell suspensions by speed of sound measurements of neutrally buoyant samples”. In: *Analytical chemistry* 89.17 (2017), pp. 8917–8923.
- [179] P. Augustsson et al. “Measuring the acoustophoretic contrast factor of living cells in microchannels”. In: *Proc. 14th MicroTAS, 3–7 October 2010, Groningen, The Netherlands, CBMS* (2010).

Bibliography

- [180] H. Wang et al. “Single-cell compressibility quantification for assessing metastatic potential of cancer cells through multi-frequency acoustophoresis”. In: *Microfluidics and Nanofluidics* 22.6 (2018), pp. 1–7.
- [181] K. Loskutova et al. “Measuring the Compressibility of Cellulose Nanofiber-Stabilized Microdroplets Using Acoustophoresis”. In: *Micromachines* 12.12 (2021), p. 1465.
- [182] Q. Zhou et al. “Piezoelectric single crystal ultrasonic transducers for biomedical applications”. In: *Progress in materials science* 66 (2014), p. 87111.
- [183] K. Komiyama. *Module for quartz watch*. Google Patents. US Patent 5,062,090. 1991.
- [184] C Brown et al. “Piezoelectric materials, a review of progress”. In: *IRE Transactions on component parts* 9.4 (1962), pp. 193–211.
- [185] A. N. S. Institute. *IEEE Standard on Piezoelectricity, ANSI/IEEE Std 176-1987*. IEEE, Institute of Electrical and Electronics Engineers, 1988.
- [186] N. Pérez et al. “Numerical characterization of piezoceramics using resonance curves”. In: *Materials* 9.2 (2016), p. 71.
- [187] A. Niedermayer et al. “Methods for the robust measurement of the resonant frequency and quality factor of significantly damped resonating devices”. In: *Measurement Science and Technology* 23.8 (2012), p. 085107.
- [188] H. Bruus. “Acoustofluidics 2: Perturbation theory and ultrasound resonance modes”. In: *Lab on a Chip* 12.1 (2012), pp. 20–28.
- [189] V. T. Rathod. “A review of acoustic impedance matching techniques for piezoelectric sensors and transducers”. In: *Sensors* 20.14 (2020), p. 4051.
- [190] A. Lenshof et al. “Acoustofluidics 5: Building microfluidic acoustic resonators”. In: *Lab on a Chip* 12.4 (2012), pp. 684–695.
- [191] H. Bruus. “Acoustofluidics 2: Perturbation theory and ultrasound resonance modes”. In: *Lab on a Chip* 12.1 (2012), pp. 20–28.
- [192] L. P. Gor’kov. “On the forces acting on a small particle in an acoustical field in an ideal fluid”. In: *Sov. Phys. Dokl.* Vol. 6. 1962, pp. 773–775.
- [193] J. Fankhauser, C. Goering, and J. Dual. “OSAFT Library: An open-source Python library for acoustofluidics”. In: *Frontiers in Physics* (2022), p. 445.
- [194] K. Yosioka and Y. Kawasima. “Acoustic radiation pressure on a compressible sphere”. In: *Acta Acustica united with Acustica* 5.3 (1955), pp. 167–173.
- [195] W. L. M. Nyborg. “Acoustic streaming”. In: *Physical acoustics*. Vol. 2. Elsevier, 1965, pp. 265–331.
- [196] J. Lighthill. “Acoustic streaming”. In: *Journal of sound and vibration* 61.3 (1978), pp. 391–418.
- [197] H. Bruus. “Acoustofluidics 7: The acoustic radiation force on small particles”. In: *Lab on a Chip* 12.6 (2012), pp. 1014–1021.
- [198] A. A. Doinikov. “Acoustic radiation pressure on a compressible sphere in a viscous fluid”. In: *Journal of Fluid Mechanics* 267 (1994), pp. 1–22.

- [199] A. Doinikov. “Acoustic radiation pressure on a rigid sphere in a viscous fluid”. In: *Proceedings of the Royal Society of London. Series A: Mathematical and Physical Sciences* 447.1931 (1994), pp. 447–466.
- [200] A. A. Doinikov. “Acoustic radiation force on a spherical particle in a viscous heat-conducting fluid. I. General formula”. In: *The Journal of the Acoustical Society of America* 101.2 (1997), pp. 713–721.
- [201] A. A. Doinikov. “Acoustic radiation force on a spherical particle in a viscous heat-conducting fluid. II. Force on a rigid sphere”. In: *The Journal of the Acoustical Society of America* 101.2 (1997), pp. 722–730.
- [202] A. A. Doinikov. “Acoustic radiation force on a spherical particle in a viscous heat-conducting fluid. III. Force on a liquid drop”. In: *The Journal of the Acoustical Society of America* 101.2 (1997), pp. 731–740.
- [203] A. A. Doinikov, J. Fankhauser, and J. Dual. “Nonlinear dynamics of a solid particle in an acoustically excited viscoelastic fluid. I. Acoustic streaming”. In: *Physical Review E* 104.6 (2021), p. 065107.
- [204] A. A. Doinikov, J. Fankhauser, and J. Dual. “Nonlinear dynamics of a solid particle in an acoustically excited viscoelastic fluid. II. Acoustic radiation force”. In: *Physical Review E* 104.6 (2021), p. 065108.
- [205] A. Pavlic et al. “Influence of particle shape and material on the acoustic radiation force and microstreaming in a standing wave”. In: *Physical Review E* 106.1 (2022), p. 015105.
- [206] A. Pavlic, L. Ermanni, and J. Dual. “Interparticle attraction along the direction of the pressure gradient in an acoustic standing wave”. In: *Physical Review E* 105.5 (2022), p. L053101.
- [207] C. L. Harshbarger et al. “Optical feedback control loop for the precise and robust acoustic focusing of cells, micro-and nanoparticles”. In: *Lab on a Chip* 22.15 (2022), pp. 2810–2819.
- [208] A. Kundt. “Ueber eine neue Art akustischer Staubfiguren und über die Anwendung derselben zur Bestimmung der Schallgeschwindigkeit in festen Körpern und Gasen”. In: *Annalen der Physik* 203.4 (1866), pp. 497–523.
- [209] T. Laurell and A. Lenshof, eds. *Microscale Acoustofluidics*. The Royal Society of Chemistry, 2015, P001–574. ISBN: 978-1-84973-671-8.
- [210] C. H. W. St. *Sonic flocculator and method of flocculating smoke or the like*. US Patent 2,215,484. 1940.
- [211] A. Marzo et al. “Holographic acoustic elements for manipulation of levitated objects”. In: *Nature Communications* 6.8661 (Oct. 2015), p. 8661.
- [212] K. Melde et al. “Holograms for acoustics”. In: *Nature* 537.7621 (Sept. 2016), pp. 518–522.
- [213] A. Ozcelik et al. “Acoustic tweezers for the life sciences”. In: *Nature methods* 15.12 (2018), pp. 1021–1028.

Bibliography

- [214] N. F. Läubli et al. “3D mechanical characterization of single cells and small organisms using acoustic manipulation and force microscopy”. In: *Nature communications* 12.1 (2021), pp. 1–11.
- [215] W. Connacher et al. “Micro/nano acoustofluidics: materials, phenomena, design, devices, and applications”. In: *Lab on a Chip* 18.14 (2018), pp. 1952–1996.
- [216] F. Lickert et al. “Acoustophoresis in polymer-based microfluidic devices: Modeling and experimental validation”. In: *The Journal of the Acoustical Society of America* 149.6 (2021), pp. 4281–4291.
- [217] A. G. Steckel and H. Bruus. “Numerical study of bulk acoustofluidic devices driven by thin-film transducers and whole-system resonance modes”. In: *The Journal of the Acoustical Society of America* 150.1 (2021), pp. 634–645.
- [218] Y. Zhou. “Comparison of numerical models for bulk and surface acoustic wave-induced acoustophoresis in a microchannel”. In: *The European Physical Journal Plus* 135.9 (2020), pp. 1–12.
- [219] N. Nama et al. “Numerical study of acoustophoretic motion of particles in a PDMS microchannel driven by surface acoustic waves”. In: *Lab on a Chip* 15.12 (2015), pp. 2700–2709.
- [220] S. J. Raymond et al. “A deep learning approach for designed diffraction-based acoustic patterning in microchannels”. In: *Scientific reports* 10.1 (2020), pp. 1–12.
- [221] P. Augustsson et al. “Iso-acoustic focusing of cells for size-insensitive acoustomechanical phenotyping”. In: *Nature communications* 7.1 (2016), pp. 1–9.
- [222] M. E. Piyasena et al. “Multinode acoustic focusing for parallel flow cytometry”. In: *Analytical chemistry* 84.4 (2012), pp. 1831–1839.
- [223] A. Fornell et al. “Acoustic focusing of beads and cells in hydrogel droplets”. In: *Scientific Reports* 11.1 (2021), pp. 1–9.
- [224] G. P. Gautam et al. “Simple and inexpensive micromachined aluminum microfluidic devices for acoustic focusing of particles and cells”. In: *Analytical and bioanalytical chemistry* 410.14 (2018), pp. 3385–3394.
- [225] J. Shi et al. “Focusing microparticles in a microfluidic channel with standing surface acoustic waves (SSAW)”. In: *Lab on a Chip* 8.2 (2008), pp. 221–223.
- [226] R. J. Olson et al. “Imaging FlowCytobot modified for high throughput by in-line acoustic focusing of sample particles”. In: *Limnology and Oceanography: Methods* 15.10 (2017), pp. 867–874.
- [227] I. Iranmanesh et al. “On-chip ultrasonic sample preparation for cell based assays”. In: *RSC advances* 5.91 (2015), pp. 74304–74311.
- [228] P. Sehgal and B. J. Kirby. “Separation of 300 and 100 nm Particles in Fabry–Perot Acoustofluidic Resonators”. In: *Analytical Chemistry* 89.22 (Oct. 2017), pp. 12192–12200.
- [229] Z. Mao et al. “Enriching Nanoparticles via Acoustofluidics”. In: *ACS Nano* 11.1 (Jan. 2017), pp. 603–612. DOI: 10.1021/acsnano.6b06784. URL: <https://doi.org/10.1021/acsnano.6b06784>.

- [230] S. Battat, D. A. Weitz, and G. M. Whitesides. “An outlook on microfluidics: the promise and the challenge”. In: *Lab on a Chip* 22.3 (2022), pp. 530–536.
- [231] P. B. Muller et al. “A numerical study of microparticle acoustophoresis driven by acoustic radiation forces and streaming-induced drag forces”. In: *Lab on a Chip* 12.22 (2012), pp. 4617–4627.
- [232] W. Qiu, H. Bruus, and P. Augustsson. “Particle-size-dependent acoustophoretic motion and depletion of micro-and nano-particles at long timescales”. In: *Physical Review E* 102.1 (2020), p. 013108.
- [233] E. Undvall et al. “Inertia-Induced Breakdown of Acoustic Sorting Efficiency at High Flow Rates”. In: *Physical Review Applied* 17.3 (2022), p. 034014.
- [234] B. Hammarström, T. Laurell, and J. Nilsson. “Seed particle-enabled acoustic trapping of bacteria and nanoparticles in continuous flow systems”. In: *Lab on a Chip* 12.21 (2012), pp. 4296–4304.
- [235] M. Wu et al. “Acoustic separation of nanoparticles in continuous flow”. In: *Advanced functional materials* 27.14 (2017), p. 1606039.
- [236] C. Harshbarger et al. “High sensitivity measurements of the Acoustic Contrast Factor of stiffness altered biological cells”. In: *Acoustofluidic 2022*. 2022.
- [237] *Alchemical studies*. eng. [Reprinted]. The collected works of C. G. Jung vol. 13. London: Routledge & Kegan, 1973. ISBN: 0710061897.
- [238] G. P. Gupta and J. Massagué. “Cancer metastasis: building a framework”. In: *Cell* 127.4 (2006), pp. 679–695.
- [239] M. Wiklund. “Acoustofluidics 12: Biocompatibility and cell viability in microfluidic acoustic resonators”. In: *Lab on a Chip* 12.11 (2012), pp. 2018–2028.
- [240] A. Pillarisetti et al. “Mechanical phenotyping of mouse embryonic stem cells: increase in stiffness with differentiation”. In: *Cellular Reprogramming (Formerly Cloning and Stem Cells)* 13.4 (2011), pp. 371–380.
- [241] R. Thavarajah et al. “Chemical and physical basics of routine formaldehyde fixation”. In: *Journal of oral and maxillofacial pathology: JOMFP* 16.3 (2012), p. 400.
- [242] T. Wakatsuki et al. “Effects of cytochalasin D and latrunculin B on mechanical properties of cells”. In: *Journal of cell science* 114.5 (2001), pp. 1025–1036.
- [243] M. Schliwa. “Action of cytochalasin D on cytoskeletal networks.” In: *The Journal of cell biology* 92.1 (1982), pp. 79–91.
- [244] P. H. Guttman and S. Halpern. “Nuclear-nucleolar volume ratio in cancer”. In: *The American Journal of Cancer* 25.4 (1935), pp. 802–806.
- [245] K. Kim and J. Guck. “The relative densities of cytoplasm and nuclear compartments are robust against strong perturbation”. In: *Biophysical Journal* 119.10 (2020), pp. 1946–1957.
- [246] L. R. Taggart et al. “Ultrasonic characterization of whole cells and isolated nuclei”. In: *Ultrasound in medicine & biology* 33.3 (2007), pp. 389–401.

Bibliography

- [247] J. T. Karlsen and H. Bruus. “Forces acting on a small particle in an acoustical field in a thermoviscous fluid”. In: *Physical Review E* 92.4 (2015), p. 043010.
- [248] N. Nijenhuis et al. “Combining AFM and acoustic probes to reveal changes in the elastic stiffness tensor of living cells”. In: *Biophysical journal* 107.7 (2014), pp. 1502–1512.
- [249] D. T. Blackstock. *Fundamentals of physical acoustics*. 2001.
- [250] S.-F. Jia, L. L. Worth, and E. S. Kleinerman. “A nude mouse model of human osteosarcoma lung metastases for evaluating new therapeutic strategies”. In: *Clinical & experimental metastasis* 17.6 (1999), pp. 501–506.
- [251] J. Schindelin et al. “Fiji: an open-source platform for biological-image analysis”. In: *Nature methods* 9.7 (2012), pp. 676–682.
- [252] S. Berg et al. “ilastik: interactive machine learning for (bio)image analysis”. In: *Nature Methods* (Sept. 2019). ISSN: 1548-7105.
- [253] COMSOL AB, Stockholm, Sweden. *COMSOL Multiphysics® v. 5.6*. Version 5.6. 2021. URL: www.comsol.com.
- [254] T. Baasch, A. Pavlic, and J. Dual. “Acoustic radiation force acting on a heavy particle in a standing wave can be dominated by the acoustic microstreaming”. In: *Physical Review E* 100.6 (2019), p. 061102.
- [255] D. Andrews and M. McIntyre. “An exact theory of nonlinear waves on a Lagrangian-mean flow”. In: *Journal of fluid Mechanics* 89.4 (1978), pp. 609–646.
- [256] O. Bühler. *Waves and mean flows*. Cambridge University Press, 2014.
- [257] A. Urbansky et al. “Label-free separation of leukocyte subpopulations using high throughput multiplex acoustophoresis”. In: *Lab on a Chip* 19.8 (2019), pp. 1406–1416.
- [258] W. Connacher et al. “Portable acoustofluidic nebulizer”. In: *The Journal of the Acoustical Society of America* 146.4 (2019), pp. 2816–2816.
- [259] S. Marqus et al. “High frequency acoustic nebulization for pulmonary delivery of antibiotic alternatives against *Staphylococcus aureus*”. In: *European Journal of Pharmaceutics and Biopharmaceutics* 151 (2020), pp. 181–188.
- [260] A. Huang et al. “Practical microcircuits for handheld acoustofluidics”. In: *Lab on a Chip* 21.7 (2021), pp. 1352–1363.
- [261] J. T. Karlsen et al. “Acoustic streaming and its suppression in inhomogeneous fluids”. In: *Physical review letters* 120.5 (2018), p. 054501.
- [262] J. S. Bach and H. Bruus. “Suppression of acoustic streaming in shape-optimized channels”. In: *Physical Review Letters* 124.21 (2020), p. 214501.
- [263] T. Baasch, I. Leibacher, and J. Dual. “Multibody dynamics in acoustophoresis”. In: *The Journal of the Acoustical Society of America* 141.3 (2017), pp. 1664–1674.
- [264] M. Kalinich and D. A. Haber. “Cancer detection: Seeking signals in blood”. In: *Science* 359.6378 (2018), pp. 866–867.

- [265] P. S. Mitchell et al. “Circulating microRNAs as stable blood-based markers for cancer detection”. In: *Proceedings of the National Academy of Sciences* 105.30 (2008), pp. 10513–10518.
- [266] P.-H. Wu et al. “A comparison of methods to assess cell mechanical properties”. In: *Nature methods* 15.7 (2018), pp. 491–498.
- [267] T. Baasch et al. “Acoustic compressibility of *Caenorhabditis elegans*”. In: *Biophysical journal* 115.9 (2018), pp. 1817–1825.
- [268] N. Aceto et al. “Circulating tumor cell clusters are oligoclonal precursors of breast cancer metastasis”. In: *Cell* 158.5 (2014), pp. 1110–1122.
- [269] S. S. Shapiro and M. B. Wilk. “An analysis of variance test for normality (complete samples)”. In: *Biometrika* 52.3/4 (1965), pp. 591–611.
- [270] D. C. Bernardoni. “Acoustofluidics for Biomedical Applications”. MA thesis. ETH Zurich, 2022.

Research output

This chapter lists the research output during the duration of this thesis (2019 - 2023) at the Institute for Mechanical Systems (IMES) and at the Institute for Biomechanics (IfB), ETH Zurich.

Publications in peer-reviewed scientific journals

1. Harshbarger, C., Gerlt, M., Ghadamian, J., Bernardoni, D., Snedeker, J., & Dual, J. "Optical feedback control loop for the precise and robust acoustic focusing of cells, micro-and nanoparticles" In: Lab on a Chip 22.15 (2022), pp. 2810–2819.
2. Pavlic, A., Harshbarger, C. L., Rosenthaler, L., Snedeker, J. G., & Dual, J. "Sharp-edge-based acoustofluidic chip capable of programmable pumping, mixing, cell focusing and trapping." In: Physics of Fluids (2023).
3. Pavlic, A., Roth, L., Harshbarger, C. L., & Dual, J. "Efficient modeling of sharp-edge acoustofluidics" In: Frontiers in Physics (2023).

Conference contributions

1. Harshbarger, C., Pavlic, A., Bernardoni, C., Viol, A., Snedeker, J., & Dual, J. (2022). High sensitivity measurements of the Acoustic Contrast Factor of stiffness altered biological cells". Acoustofluidics 2022. 2022.
2. Pavlic, A., Harshbarger, C. L., Rosenthaler, L., & Dual, J. (2021). Acoustically driven sharp-edge micropump capable of cell focusing and fluid mixing. The 25th International Conference on Miniaturized Systems for Chemistry and Life Sciences, Palm Springs, USA, October 10-14, 2021. Poster presentation.

Submitted but not yet accepted publications

1. Harshbarger, C.,* Pavlic, A.,* Bernardoni, D., Viol, A., Snedeker, J., Dual, J., Silván U. Measuring and simulating the biophysical basis of the acoustic contrast factor of biological cells. * These authors contributed equally to the publication.

Teaching activities

Courses

Biomechanics 1 (Prof. Snedeker)	Head assistant Semester: Spring 2021, 2022 & 2023
Bioengineering (Prof. Snedeker)	Head assistant Semester: Spring 2021 & 2022
Practical course in Med. Tec. (Prof. Snedeker)	Head assistant and Co-creator Semester: Autumn 2021 & Autumn 2022
Technische Mechanik (Prof. Dual)	Co-head assistant with Alen Pavlic Semester: Autumn 2020
Mechanik GZ (Prof. Glocker)	Co-head assistant with Alen Pavlic Semester: Spring 2021 & 2022
Microscale Acoustofluidics (Prof. Dual)	Assistant for practical lab Semester: Autumn 2020, & 2021

Teaching activities

Supervision of students¹

Student Name	Thesis	Date	Title
Kilian Lock	BSc	09/2019	Impact of Cell Membrane Roughness on Deformability Measurements
Jana Petr	Sem.	03/2020	The Effects of Actin Cytoskeleton Changes on Deformability Cytometry
Anna Kollár	Sem.	04/2020	Roughness analysis of Blebbistatin treated cells in suspension
Benedikt von Manitius*	Study	05/2020	A review about particle manipulation at sharp edges and acoustic needles
	BSc	06/2020	Testing and simulating of a novel acoustic device: focusing on the needle-piezoelectric transducer interaction
Pushkin Nagpure*	Study	06/2020	The acoustic radiation force on objects of irregular shape and the related microstreaming
	BSc	06/2020	The Acoustic Radiation Force on objects of irregular shape and the related microstreaming
Lukas Roth*	BSc	06/2020	Nonlinear time-averaged phenomena near the side-channel openings in acoustofluidic devices
Marco Ravasi*	BSc	06/2020	Testing of a novel acoustofluidic device: Acoustic radiation force and acoustic streaming around the tip of the needle and comparison to experimental results
Theo Rodde*	BSc	06/2020	Computational modelling of thin film bulk acoustic wave devices for the use in circulating tumor cell detection
Sara Landolt	BSc	09/2020	Development of a blood handling and spiking protocol for the use in circulating tumor cell detection
Jana Petr	MSc	10/2020	CTC isolation from fluids using acoustofluidic devices
Luca Rosenthaler*	BSc	12/2020	Experimental investigation of nonlinear time-averaged phenomena near the side-channel openings in acoustofluidic devices
Florian Piringer*	BSc	06/2021	Improving an Acoustofluidic Needle
Tobias Heinz	BSc	06/2021	Cell enrichment using BAW acoustofluidic devices
Francesco Gatti	Sem.	06/2021	Development and evaluation of exosome isolation protocols for the use in acoustophoresis
Jan Ghadamian	BSc	06/2021	Feedback control system for BAW devices for optimal piezoelectric transducer excitation frequency
Davide Bernardoni	Sem.	07/2021	Sarcoma cell line manipulation using BAW acoustofluidic devices with the aid of a feedback control system
Amelie Viol	BSc	06/2022	Static and dynamic mechanoprofiling of cells
Davide Bernardoni	MSc	06/2022	Acoustofluidics for Biomedical Applications
Lukas Roth*	MSc	08/2022	Exploiting nonlinear time-averaged phenomena near sharp edges in acoustofluidic devices

¹Students with name* were co-supervised with Alen Pavlic

Curriculum Vitae

Cooper Lars Harshbarger

Born on March 14th, 1993 in Pleasanton, California, USA
Citizen of Switzerland, Sweden and the USA



Education

- | | |
|------------------|--|
| 2019 – 2023 | PhD student in Prof. J. Dual's group, IMES,
and in Prof. J. Snedeker's group, IfB,
Swiss Federal Institute of Technology (ETH) Zurich, Switzerland |
| Jan. – July 2019 | Master thesis student in Prof. E. Kuhl's lab,
Stanford University, CA, USA |
| 2013 – 2018 | Bachelor and Masters degree in mechanical engineering
Swiss Federal Institute of Technology (ETH) Zurich, Switzerland |
| 2011 – 2013 | Kantonale Maturitätsschule für Erwachsene, Zurich |
| 2008 – 2011 | KV Zürich Business School, Zurich |

Professional experience

- | | |
|-------------------|---|
| 2021 – present | Bouldering coach and route setter at ASVZ, Zurich |
| Feb. – July. 2019 | Route Setter and Climbing Instructor Certification,
Stanford University, USA |
| Aug. – Dec. 2018 | Intern, ZuriMED, Zurich |
| 2014 – 2017 | Teaching assistant, ETH, Zurich |
| Jan. – Feb. 2014 | Workshop training, Burckhardt Compression, Zurich |
| 2008 – 2011 | Apprenticeship, Credit Suisse and Clariden Leu, Zurich |